

SEARCH FOR LONG-LIVED RESONANCE  
DECAYING TO A DILEPTON PAIR IN  $pp$   
COLLISIONS AT  $\sqrt{s} = 13$  TEV WITH  
THE ATLAS DETECTOR

DISSERTATION

Presented in Partial Fulfillment of the Requirements for the Degree Doctor of  
Philosophy in the Graduate School of The Ohio State University

By

Siinn Che, B.S., M.S.

Graduate Program in Physics

The Ohio State University

2018

Dissertation Committee:

Professor K.K. Gan, Advisor

Professor Richard Kass

Professor Junko Shigemitsu

Professor Fengyuan Yang

© Copyright by

Siinn Che

2018

# ABSTRACT

A search for a long-lived neutral massive particle decaying to a  $\mu\mu$ ,  $ee$ , or  $e\mu$  pair is presented with  $32.8 \text{ fb}^{-1}$  of  $pp$  collisions at  $\sqrt{s} = 13 \text{ TeV}$  taken by the ATLAS detector at the LHC. Upper limits are presented on the production cross section times branching ratio for resonances decaying to a lepton pair. Also presented is the detection efficiency as a function of  $p_T$  and  $\eta$  for a resonance with mass of  $0.1\text{--}2.0 \text{ TeV}$  and lifetime ( $c\tau$ ) of  $100\text{--}500 \text{ mm}$  to allow for an upper limit on the cross section for any model of interest.

## Dedication

some more text

## ACKNOWLEDGMENTS

I would like to thank my parents for their endless support and love. Also, I would like to thank Prof. K.K. Gan for his guidance and support throughout my graduate career. Add more text.

# Table of Contents

	<b>Page</b>
Abstract . . . . .	ii
Dedication . . . . .	iii
Acknowledgments . . . . .	iv
<b>List of Figures . . . . .</b>	<b>viii</b>
<b>List of Tables . . . . .</b>	<b>xi</b>

## Chapters

<b>1 Introduction and Theory . . . . .</b>	<b>1</b>
1.1 The Standard Model . . . . .	1
1.1.1 Fundamental Particles and Interactions . . . . .	1
1.2 Beyond the Standard Model . . . . .	3
1.2.1 $Z'$ from the extension of the Standard Model . . . . .	3
1.2.2 Long-lived $Z'$ Discovery Mode at the LHC . . . . .	4
<b>2 The ATLAS Experiment at the LHC . . . . .</b>	<b>6</b>
2.1 The Large Hadron Collider . . . . .	6
2.2 The ATLAS detector . . . . .	7
2.2.1 Coordinate System . . . . .	7
2.2.2 The Inner Detector . . . . .	8
2.2.3 The Calorimeters . . . . .	10
2.2.4 The Muon Spectrometer . . . . .	12
2.2.5 The ATLAS Magnet . . . . .	14
2.3 The ATLAS Trigger System . . . . .	15
2.3.1 Level 1 Trigger . . . . .	16
2.3.2 High Level Trigger . . . . .	16
2.3.3 Summary of the ATLAS Detector . . . . .	16
<b>3 <math>Z'</math> Reconstruction . . . . .</b>	<b>18</b>
3.1 Track Reconstruction in the Inner Detector . . . . .	18

3.1.1	Standard Tracking . . . . .	18
3.1.2	Large Radius Tracking . . . . .	20
3.2	Electron Reconstruction . . . . .	21
3.3	Muon Reconstruction . . . . .	21
3.4	Secondary Vertex Reconstruction . . . . .	21
<b>4</b>	<b>Analysis Overview . . . . .</b>	<b>24</b>
<b>5</b>	<b>Data and MC samples . . . . .</b>	<b>25</b>
5.1	Data samples . . . . .	25
5.2	MC samples . . . . .	26
5.2.1	Signal samples . . . . .	26
5.2.2	Background MC samples . . . . .	28
<b>6</b>	<b>Signal Selection . . . . .</b>	<b>31</b>
6.1	Event preselection . . . . .	31
6.1.1	Event selection . . . . .	32
6.1.2	Muon and electron requirements . . . . .	33
6.1.3	Vertex selection . . . . .	33
<b>7</b>	<b>Signal Efficiency . . . . .</b>	<b>36</b>
7.1	Trigger efficiency . . . . .	37
7.1.1	Trigger Scale Factors . . . . .	38
7.1.2	Summary on trigger study . . . . .	43
7.2	Lepton reconstruction efficiency . . . . .	44
7.3	Overall reconstruction efficiency . . . . .	45
7.3.1	Event and vertex cut flow . . . . .	46
7.3.2	Signal efficiency and distribution . . . . .	47
7.3.3	Efficiency map . . . . .	47
<b>8</b>	<b>Background Estimation . . . . .</b>	<b>54</b>
8.1	Cosmic Background . . . . .	54
8.2	Random-Crossing Background . . . . .	55
8.2.1	Track Flipping Method . . . . .	56
8.2.2	Event Mixing Method . . . . .	57
8.2.3	MC Study . . . . .	58
8.2.4	Estimating Random-crossing Background with Data Sample . . . . .	59
<b>9</b>	<b>Systematic Uncertainties . . . . .</b>	<b>63</b>
9.1	Systematic Uncertainty in Track and Vertex Reconstruction . . . . .	63
9.1.1	Systematic uncertainties on background estimations . . . . .	67
<b>10</b>	<b>Interpretation of Results . . . . .</b>	<b>70</b>
10.1	Statistical Procedure . . . . .	70
10.2	Upper limits . . . . .	71
<b>11</b>	<b>Conclusion . . . . .</b>	<b>73</b>

<b>Bibliography</b>	<b>74</b>
<b>Appendices</b>	<b>79</b>
A Trigger efficiency	80
B Efficiency Map of Signal MC Samples	82
C $K_S$ and $Z'$ comparison	88
D Extrapolation in the track flipping method	89
D.1 Definition	89
D.2 Vertex estimation	89
D.3 Counting pairs	90
D.4 Extrapolation of control region into validation and signal regions	90
D.5 Extrapolation of validation region into signal region	91
D.6 Scale factors	92
D.7 Vertex yields in the TF method and data	92

# List of Figures

Figure	Page
2.1 LHC accelerator system and the four main experiments. . . . .	7
2.2 The ATLAS detector showing various sub-detector systems. . . . .	8
2.3 The ATLAS calorimeter system. . . . .	10
2.4 The ATLAS Muon Spectrometer . . . . .	12
2.5 Layout of the ATLAS Trigger and data acquisition system in Run 2. . . . .	15
3.1 Illustration of detector hits and reconstructed tracks in the ID. The bright colors represent the detector hits associated with reconstructed tracks. . . . .	19
3.2 Main vertex topologies in $pp$ collisions: primary, pile-up, and secondary vertices.	22
5.1 Representative plots of generator-level (a) $p_T$ and (b) $\eta$ distributions of $Z'$ , and (c), (d) are the corresponding distributions for the signal muons. The signal MC samples are generated with $m = 500, 1000$ GeV, and $c\tau = 100$ mm.	28
7.1 Trigger efficiency of single muon, single photon, di-photon, and the combined triggers of the signal MC samples of $Z' \rightarrow \mu^+ \mu^-, e^+ e^-$ , and $e^\pm \mu^\mp$ generated with $m = 250$ GeV and $c\tau = 250$ mm. . . . .	37
7.2 The efficiency of the single photon trigger for an electron as a function of (a) $ d_0 $ and (b) $ z_0 $ . The corresponding plots of the single muon trigger are shown in (c) and (d). . . . .	39
7.3 Invariant mass distributions of the tag-and-probe electron pairs used to study the efficiencies of the (a) <code>HLT_g50_loose</code> and (b) <code>HLT_g140_loose</code> trigger in the data and $Z+jets$ MC samples. Only the pairs with a probe electron in the plateau region of Figure 7.4a and 7.4b are used in the tag-and-probe method.	40
7.4 Efficiency of the <code>HLT_g50_loose</code> as a function of the (a) $p_T$ , (c) $\eta$ , and (e) $ z_0 $ of the probe in the data and $Z+jets$ MC samples. The corresponding plots of the <code>HLT_g140_loose</code> trigger are shown in (b), (d), and (f). Only the pairs with a probe electron in the plateau region of (a) and (b) are used in (c) - (f).	42
7.5 Invariant mass distributions of the tag-and-probe muon pairs used to study the efficiencies of the single muon trigger in the data and $Z+jets$ MC samples. Only the pairs with a probe muon in the plateau region of Figure 7.6a are used in the tag-and-probe method. . . . .	43

7.6	Efficiency of the single muon trigger as a function of the (a) $p_T$ and (b) $ z_0 $ of the probe in the data and $Z+jets$ MC samples. Only the muons in the plateau region ( $p_T > 62$ GeV) of (a) are used in (b). . . . .	43
7.7	Efficiency of the single muon trigger as a function the $\eta$ and $\phi$ of the probe in (a) data and (b) $Z+jets$ MC sample. . . . .	44
7.8	Lepton reconstruction efficiency as a function of (a) $d_0$ , (b) $z_0$ , (c) $\eta$ , and (d) $p_T$ of signal leptons for the $Z'$ signal MC sample generated with $m = 250$ GeV and $c\tau = 250$ mm. . . . .	45
7.9	(a) Event cut flow, and (b) vertex cut flow using the signal MC samples of $Z' \rightarrow \mu^+ \mu^-$ generated with $m = 500, 1000$ GeV for $c\tau = 100$ mm. . . . .	46
7.10	Signal efficiency as a function of (a) $r$ , (b) $z$ , (c) $\eta$ , (d) $\phi$ , and (e) pile-up for the signal MC samples of $Z' \rightarrow \mu^+ \mu^-$ with $m = 500, 1000$ GeV for $c\tau = 100$ mm. . . . .	48
7.11	Signal efficiency maps of the signal MC sample of $Z' \rightarrow \mu^+ \mu^-$ with (a) $m = 500$ and (b) $m = 1000$ GeV for $c\tau = 100$ mm. The corresponding efficiency maps for $Z' \rightarrow e^+ e^-, e^\pm \mu^\mp$ is shown in (c)–(f). . . . .	49
8.1	Distribution of pairs of two muons with highest $p_T$ in $ \Delta\phi $ and $\eta_1 + \eta_2$ found in the cosmic control region using the data sample. The sharp peak at $ \Delta\phi  = \pi$ and $\Sigma\eta = 0$ shows that a significant fraction of muon pairs in the region is from cosmic muons. The empty bins are shown with white. . . . .	55
8.2	Comparison of the $R_{CR}$ distribution of $\mu^+ \mu^-$ pairs with (dots) and without (shaded) the vertex requirement. The same distribution is shown in (b) normalized to the number of $\mu^+ \mu^-$ pairs forming a vertex. . . . .	56
8.3	Description of track flipping method in (a) $r - z$ and (b) $x - y$ plane. Given two tracks $A$ and $B$ originating from a common secondary vertex, one random track is flipped with respect to the beam spot and is denoted as $B'$ . The resulting flipped track pair, $AB'$ , cannot form a vertex due to the separation in space. . . . .	57
8.4	Vertex cut flow applied on $x^+ x^-$ vertices from the TF method. . . . .	59
8.5	Comparison of (a) vertex mass, (b) $\chi^2/\text{DOF}$ , (c) transverse, and (d) longitudinal position of $x^+ x^-$ vertices reconstructed in TF and event mixing with those reconstructed in the background MC samples. In (c), the red dashed lines indicate the four Pixel layers. The green dotted lines indicate the Inner Support Tube (45.5 mm) and Pixel Support Tube (229 mm). . . . .	60
8.6	Comparison of (a) vertex mass, (b) $\chi^2/\text{DOF}$ , (c) transverse, and (d) longitudinal position of vertices found in data with vertices formed in track flipping in the control region. In (c), the red dashed lines indicate the four Pixel layers. The green dotted lines indicate the Inner Support Tube (45.5 mm) and Pixel Support Tube (229 mm). . . . .	61

9.1	Comparison of the (a) invariant mass, (b) $p_T$ , (c) $\mu$ , (d) transverse, (e) longitudinal position, and (f) decay length of $K_S$ vertex with two large-radius tracks in the data with the MC samples. Data is normalized to MC. In (d), the red dashed lines indicate the four pixel layers and the first layer of SCT. The green dotted lines indicate the Inner Support Tube (45.5 mm) and Pixel Support Tube (229 mm). MC sample is reweighted to the pile-up distribution in the data. . . . .	66
9.2	Representative distributions of the invariant mass of $K_S$ candidates with two large-radius tracks for (a) $2 < r < 100$ mm, (b) $100 < r < 150$ mm, (c) $150 < r < 200$ mm, (d) $200 < r < 250$ mm, and (e) $250 < r < 300$ mm in the data and the MC samples. Data is normalized to MC samples. . . . .	68
9.3	The radial distribution of $K_S$ yields with two large-radius tracks. Data is normalized to the MC for $K_S$ found with the ST tracking. . . . .	69
10.1	The observed 95% CL upper limits on the $\sigma \times \text{BR}$ for the $Z' \rightarrow$ (a) $\mu^+ \mu^-$ , (b) $e^+ e^-$ , and (c) $e^\pm \mu^\mp$ signal samples with $Z'$ masses of 100 - 1000 GeV as a function of $c\tau$ . The dashed lines are expected limits, and the solid bands represent $1\sigma$ uncertainty on the expected limit. . . . .	72
B.1	Reconstruction efficiency map of $ \eta $ vs. $p_T$ for $Z' \rightarrow \mu^+ \mu^-$ MC sample with $m_{Z'} = 100$ and 250 GeV. . . . .	82
B.2	Reconstruction efficiency map of $ \eta $ vs. $p_T$ for $Z' \rightarrow \mu^+ \mu^-$ MC sample with $m_{Z'} = 500, 750$ and 1000 GeV. . . . .	83
B.3	Reconstruction efficiency map of $ \eta $ vs. $p_T$ for $Z' \rightarrow e^+ e^-$ MC sample with $m_{Z'} = 100, 250$ and 500 GeV. . . . .	84
B.4	Reconstruction efficiency map of $ \eta $ vs. $p_T$ for $Z' \rightarrow e^+ e^-$ MC sample with $m_{Z'} = 750$ and 1000 GeV. . . . .	85
B.5	Reconstruction efficiency map of $ \eta $ vs. $p_T$ for $Z' \rightarrow e^\pm \mu^\mp$ MC sample with $m_{Z'} = 100, 250$ and 500 GeV. . . . .	86
B.6	Reconstruction efficiency map of $ \eta $ vs. $p_T$ for $Z' \rightarrow e^\pm \mu^\mp$ MC sample with $m_{Z'} = 750$ and 1000 GeV. . . . .	87
C.7	Distribution of (a) transverse and (b) longitudinal position, (c) $\eta$ , and (d) $p_T$ of $K_S$ and $Z'$ vertices found in the $Z'$ and genetic MC sample described in Section 5.2.2. $Z'$ distribution is normalized to $K_S$ distribution. Statistical uncertainties are shown. . . . .	88

# List of Tables

<b>Table</b>	<b>Page</b>
1.1 The fundamental fermions and their electric charge $Q$ and masses. . . . .	2
1.2 Gauge bosons and their associated fields and masses. . . . .	3
2.1 The spatial, energy resolution and the particle identification of the Atlas detector. . . . .	17
3.1 Main track selection in the standard and large radius tracking algorithms. . .	19
3.2 Fiducial selections on particles for tracking efficiency measurements. . . .	20
3.3 Track requirements for secondary vertex reconstruction. . . . .	23
5.1 Dataset used in DRAW_RPVLL, DAOD_RPVLL, and DAOD_SUSY15 format. . . .	26
5.2 Datasets used for tag and probe studies. . . . .	26
5.3 Mass, lifetime, and DSID of the signal MC samples. . . . .	27
5.4 Background MC samples used in the study of random-crossing background and in the estimation of tracking and vertexing systematic uncertainty. . . .	29
5.5 Background MC samples without the LRT used for tag and probe studies. .	30
6.1 HLTs used to select events in DRAW_RPVLL filter. The single photon trigger requires one photon with $p_T > 140$ GeV. The di-photon trigger requires two photons with $p_T > 50$ GeV. The single muon trigger requires one muon with $p_T > 60$ within $ \eta  < 1.05$ using MS information only. . . . .	32
6.2 RPVLL filter offline selection on photon and leptons. . . . .	32
6.3 Muon and electron requirements applied at analysis level. . . . .	34
6.4 The control, validation, and signal regions defined by the vertex type. . . .	34
6.5 Event and vertex selections applied to select displaced vertices. . . . .	35
7.1 Selection criteria for tag-and-probe electrons in $Z + \text{jets}$ studies. . . . .	40
7.2 Selection criteria for tag-and-probe muons. . . . .	41
7.3 Total trigger scale factors from the tag-and-probe method. . . . .	44
7.4 Event and vertex cut flow of the signal MC sample of $Z' \rightarrow \mu^+ \mu^-$ . . . .	50
7.5 Event and vertex cut flow of the signal MC sample of $Z' \rightarrow e^+ e^-$ . . . .	51
7.6 Event and vertex cut flow of the signal MC sample of $Z' \rightarrow e^\pm \mu^\mp$ . . . .	52

7.7	Overall signal efficiency of the signal samples. Statistical uncertainties are shown. . . . .	53
8.1	Comparison of the estimated vertex yields from the TF and event mixing with those reconstructed in the background MC samples. . . . .	59
8.2	Number of $x$ , $\mu$ , $e$ tracks and the calculated lepton probability from data. . .	61
8.3	The estimate of random-crossing background in the signal region. Scale factors (Table D.4) are applied to obtain the corrected estimate of the background. .	62
9.1	Comparison of $Z'$ and $K_S$ vertex selections. . . . .	65
A.1	Trigger efficiency of single muon, single photon, di-photon triggers, and the combined trigger efficiency of the signal MC samples of $Z' \rightarrow \mu^+ \mu^-$ . Statistical uncertainty is shown. . . . .	80
A.2	Trigger efficiency of single muon, single photon, di-photon triggers, and the combined trigger efficiency of the signal MC samples of $Z' \rightarrow e^+ e^-$ . Statistical uncertainty is shown. . . . .	81
A.3	Trigger efficiency of single muon, single photon, di-photon triggers, and the combined trigger efficiency of the signal MC samples of $Z' \rightarrow e^\pm \mu^\mp$ . Statistical uncertainty is shown. . . . .	81
D.4	(a) Vertex yields in the TF and data. (b) The scale factors calculated from the vertex yields . . . . .	93

# Chapter 1

## INTRODUCTION AND THEORY

In this chapter, the theoretical background and motivations for the search for new physics with long-lived particles are presented. In Section 1.1, an overview of the Standard Model of particle physics is presented. In Section 1.2 the theories beyond the Standard Model that predict new long-lived gauge bosons and the potential discovery mode of the new particles are discussed.

### 1.1 The Standard Model

The Standard Model (SM) [1] of particle physics has been a very successful theory in modern physics that describes the known fundamental particles and their interactions. The SM is a gauge theory based on  $SU(3)\otimes SU(2)\otimes U(1)$  symmetry group. The symmetry group describes three fundamental interactions, quantum chromodynamics (QCD), quantum electrodynamics (QED), and weak interactions, which arises from the requirement of local gauge invariance. The much weaker force of gravity is not incorporated in the SM. Common particles, e.g. protons and neutrons, are made up of fermions, and the interactions between the fermions are mediated by spin 1 gauge bosons. Fermions acquire mass by interacting with the Higgs field  $H$  via spontaneous symmetry breaking [2].

#### 1.1.1 Fundamental Particles and Interactions

The elementary particles in the SM can be divided into two groups, fermions and bosons, and all elementary particles have associated anti-particles with the same property but with opposite charge.

Fermions are spin  $\frac{1}{2}$  particles that constitute the building blocks of matter, and they can be divided into two groups, leptons and quarks. Leptons, e.g. electrons and muons, are colorless particles that do not interact through the strong force. Quarks, which make up protons and neutrons, are subject to the strong force due to color charges. There are three generations of leptons and quarks in increasing mass, and each generation consists of two leptons (electric charge 1 or 0) and two quarks (electric charge  $\frac{2}{3}$  or  $-\frac{1}{3}$ ). Quarks and charged leptons interact through the electroweak interaction while neutrinos only experience weak interaction. Fermions are described as quantum fields with *left-handed* or *right-handed* chirality, and only *left-handed* fermions and *right-handed* antifermions are subject to the charged-current weak interaction via  $W$  boson. Quarks are not observed as free particles due to *color confinement* [3], but they are only observed in color-neutral bound states, called *hadrons*. There are two types of hadrons: *mesons* and *baryons*. Mesons are composite particles with quark and anti-quark pair, and baryons are composed of three quarks. The elementary fermions are summarized in Table 1.1.

	Generation			Q (e)	Mass (MeV)		
	1 <sup>st</sup>	2 <sup>nd</sup>	3 <sup>rd</sup>				
Leptons	$\nu_e$	$\nu_\mu$	$\nu_\tau$	0	0	0	0
	$e$	$\mu$	$\tau$	-1	0.511	105.7	1777
Quarks	$u$	$c$	$t$	+2/3	2.3	1275	173070
	$d$	$s$	$b$	-1/3	4.8	95	4180

Table 1.1: The fundamental fermions and their electric charge  $Q$  and masses.

The fundamental interactions are described by gauge bosons, spin 1 particles that are generated by the symmetry groups in the SM. Gluon fields,  $g_\mu^a$ , are generated by  $SU(3)$  group where  $a = 1, \dots, 8$  and  $\mu$  is a Lorentz index ( $= 0, 1, 2, 3$ ). The quanta of gluon fields produce massless gluons that mediate strong forces. The group  $SU(2) \otimes U(1)$  generates gauge fields  $W_\mu^a$  ( $a = 1, 2, 3$ ) and  $B_\mu$  which mediate electroweak force. The physical observable gauge bosons  $W^\pm$ ,  $Z$ , and photon are created by the mixing of these gauge fields,

$$\begin{aligned} W_\mu^\pm &= (W_\mu^1 \mp iW_\mu^2)/\sqrt{2} \\ Z_\mu &= \cos\theta_W W_\mu^3 - \sin\theta_W B_\mu \\ A_\mu &= \sin\theta_W W_\mu^3 + \cos\theta_W B_\mu \end{aligned} \tag{1.1}$$

where  $\theta_W$  is the weak mixing angle.

The photon and gluons are massless, and  $W^\pm$  and  $Z$  bosons gain masses through the Higgs mechanism via spontaneous symmetry breaking. In the Higgs mechanism, an additional complex scalar field, called Higgs field, is introduced with  $SU(2)$  symmetry, and because the Higgs potential has non trivial vacuum expectation value, the symmetry of the ground state is spontaneously broken, leading to a massive scalar particle with spin 0, known as Higgs boson. The gauge bosons and their associated fields, and masses are summarized in Table 1.2

Symmetry	Gauge boson	Gauge field	$Q$ (e)	Mass (GeV)
$SU(2) \otimes U(1)$	$\gamma$	$A_\mu$	0	0
	$Z$	$Z_\mu$	0	91.2
	$W^\pm$	$W_\mu^\pm$	$\pm 1$	80.4
$SU(3)$	$g$	$g_\mu^a$	0	0

Table 1.2: Gauge bosons and their associated fields and masses.

## 1.2 Beyond the Standard Model

Although the SM has been a very successful theory at explaining fundamental particles and their interactions, there are several experimental observations and phenomena in nature that are not fully explained by the SM. These phenomena include gravity [4], hierarchy problem [5, 6], dark matter [7–9], neutrino oscillations [10], and matter-antimatter asymmetry [11, 12].

Many Beyond the Standard Model (BSM) theories predict the existence of new particles to explain these unexplained phenomena. In particular, theories such as Hidden Valley [13, 14], R-parity violation [15, 16] including Minimal Supersymmetric SM [17], and  $Z'$  models with neutrinos [18] predict the existence of weakly-coupled, neutral gauge boson at the weak scale. The new gauge boson is called  $Z'$  due to the similarity to the standard  $Z$  boson.

### 1.2.1 $Z'$ from the extension of the Standard Model

The new weakly-coupled gauge boson can be added to the SM by including an additional  $U(1)'$  symmetry to the existing  $SU(3) \otimes SU(2) \otimes U(1)$  symmetry. The spontaneous breaking of the  $U(1)'$  symmetry, similar to the electroweak symmetry breaking, produces the new gauge boson,  $Z'$  [19]. The mechanism through which the new symmetry is added to the SM varies by theories. Nonetheless, the  $Z'$  boson has two sets of parameters defining its property: the couplings to the SM particles and the energy scale at which the  $U(1)'$  symmetry is broken.

The former defines the lifetime,  $c\tau$ , of the particle while the latter defines the mass of the particle.

In one case,  $Z'$  can have the same couplings to fermions as the SM  $Z$  boson, and the particle is called *sequential*  $Z'$  [20]. There have been several searches for the sequential  $Z'$  [21–23], and although the sequential  $Z'$  provides a useful reference for some theories, it will not be considered in this thesis as the main focus of the analysis is the long-lived particles.

In other case, the  $Z'$  can have very small couplings to the SM particles such that the particle have a finite lifetime compatible with the detector volume at the ATLAS experiment. This metastable particle is called the *long-lived*  $Z'$ . Because of its small coupling to the SM, a direct production of the long-lived  $Z'$  is unlikely to be observable at the LHC. Instead, the long-lived  $Z'$  should be produced as a decay product of other particles in order to have enough sensitivity to be observed at the LHC.

In this thesis, this long-lived  $Z'$  will be used as a basis in the search for a long-lived resonance. However,  $Z'$  is only used as a convenient model to produce a generic long-lived particle, and no assumption is made on the particle and its production mechanism from existing theories.

### 1.2.2 Long-lived $Z'$ Discovery Mode at the LHC

The primary discovery mode for the long-lived  $Z'$ , or a similar long-lived particle, is via a dilepton decay channel  $Z' \rightarrow \ell^+ \ell^-$  where  $\ell = e$  or  $\mu$ . The number of dilepton pairs produced,  $N_{\ell^+ \ell^-}$ , in this process for the integrated luminosity,  $\mathcal{L}_{Int.}$ , at the LHC is given by,

$$N_{\ell^+ \ell^-} = \mathcal{L}_{Int.} \times \sigma_{Z'} \times B_{\ell^+ \ell^-}, \quad (1.2)$$

where  $\sigma_{Z'}$  is the production cross section of  $Z'$ , and  $B_{\ell^+ \ell^-} = \Gamma_{\ell^+ \ell^-} / \Gamma_{Z'}$  is the branching ratio of  $Z'$  into  $\ell^+ \ell^-$ . Therefore, if  $Z'$  is light enough to be produced at the LHC, the sensitivity to detect  $Z'$  depends on luminosity, the production cross section, and the branching ratio into a particular channel.

Long-lived particles naturally have small width ( $\tau_0 = \hbar/\Gamma$ ). The detectable mass range and lifetime of  $Z'$  is constrained by the center of mass energy ( $\sqrt{s} = 13$  TeV in Run II) and the detector volume ( $\sim O(1m)$ ). There have been other searches for long-lived dilepton resonance at ATLAS [24] and CMS [25] in Run I, and no excess was observed. In this thesis, the dilepton resonance mass, up to 1 TeV, and the lifetime up to  $c\tau = 1000$  mm are considered at  $\sqrt{s} = 13$  TeV in Run II.

Other potential discovery channels exist in searches for  $Z'$  such as  $Z' \rightarrow \tau^+ \tau^-$  and hadronic decay,  $Z' \rightarrow jj$  where  $j = \text{jet}$  although these decay modes are more experimentally difficult to detect due to the irreducible QCD background [26, 27]. The search for a long-lived  $Z'$  through a dilepton resonance is particularly interesting due to its clean final signature and low backgrounds from the SM.

# Chapter 2

## THE ATLAS EXPERIMENT AT THE LHC

The ATLAS experiment is one of the four major experiments at the LHC at the European Organization for Nuclear Research (CERN). The ATLAS detector is designed as a general-purpose particle physics experiment, together with the CMS experiment. In Section 2.1, a brief description of the LHC is given, and in Section 2.2, the ATLAS detector and its sub-detector systems are described.

### 2.1 The Large Hadron Collider

The LHC is the world’s largest synchrotron accelerator ( $pp$  collider) located at CERN near Geneva, Switzerland. The LHC’s circular beam pipes are 27 km in circumference, and two beams of protons are accelerated in opposite direction producing  $pp$  collisions at  $\sqrt{s} = 13$  TeV in Run II. Separate magnet systems are used to direct proton beams in each direction.

There are 8 interaction regions (IRs) at which two proton beams cross, and protons beams are injected into the LHC from two IRs. Before protons are injected to the LHC, they undergo a multi-stage acceleration by several accelerators [28]: a linear accelerator (LINAC2), the Proton Synchrotron Booster, the Proton Synchrotron (PS), and the Super Proton Synchrotron (SPS). The proton beams are accelerated up to 450 GeV when they are injected to the LHC with a 25 ns bunch spacing in Run II. There are more than  $10^{11}$  protons in each bunch, and the large number of protons in each bunch results in multiple collisions per bunch crossing, knowns as *pile-up*. In 2016, the mean number of interactions per bunch crossing was  $\langle \mu \rangle = 24.9$ .

The four main experiments at CERN are distributed around the LHC at collision points. Two experiments, ATLAS and CMS, are designed as general purpose experiments, and A

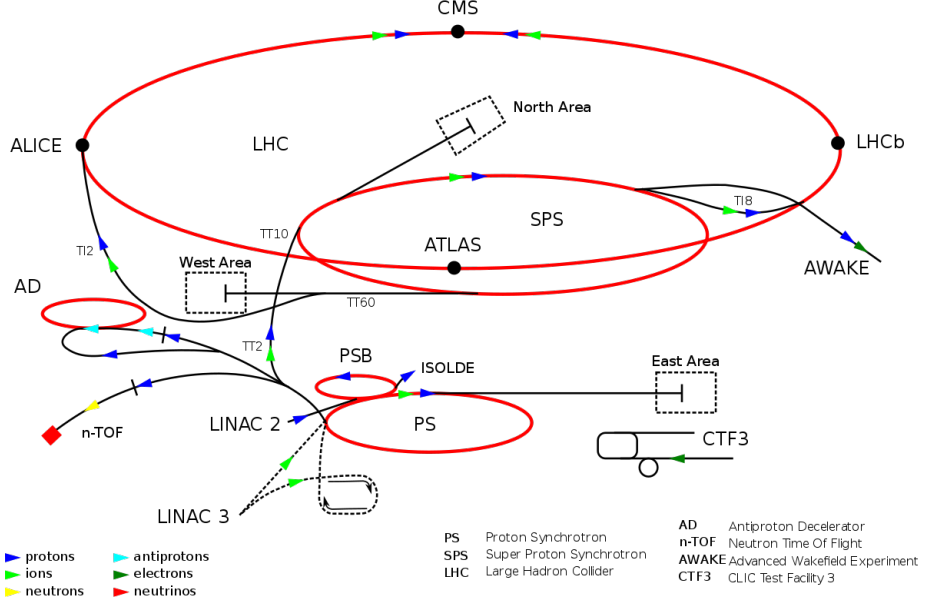


Figure 2.1: LHC accelerator system and the four main experiments.

Large Ion Collider Experiment (ALICE) and the Large Hadron Collider beauty (LHCb) are designed to study strong interaction using heavy ion collisions and the matter-antimatter asymmetry using b quarks, respectively. Figure 2.1 shows the four main experiments and the accelerators at the LHC.

## 2.2 The ATLAS detector

The ATLAS detector is a multi-purpose detector designed to investigate a wide range of physics, including the search for the Higgs boson in Run I and many searches beyond the SM. The detector measures 46 m long, 25 m in diameter, and it has three main layers of sub-detectors to detect particles created from  $pp$  collisions at the Interaction Point (IP). Figure 2.2 shows the ATLAS detector and the sub-detector systems: the Inner detector, the electromagnetic and hadronic calorimeters, and the muon spectrometer. In this section, the coordinate system, the sub-detectors, and the magnet system of the ATLAS detector are described.

### 2.2.1 Coordinate System

In the ATLAS coordinate system, the IP is defined as the origin of the coordinate system. The beam line defines the z-axis, and the x-y plane perpendicular to the beam line is referred

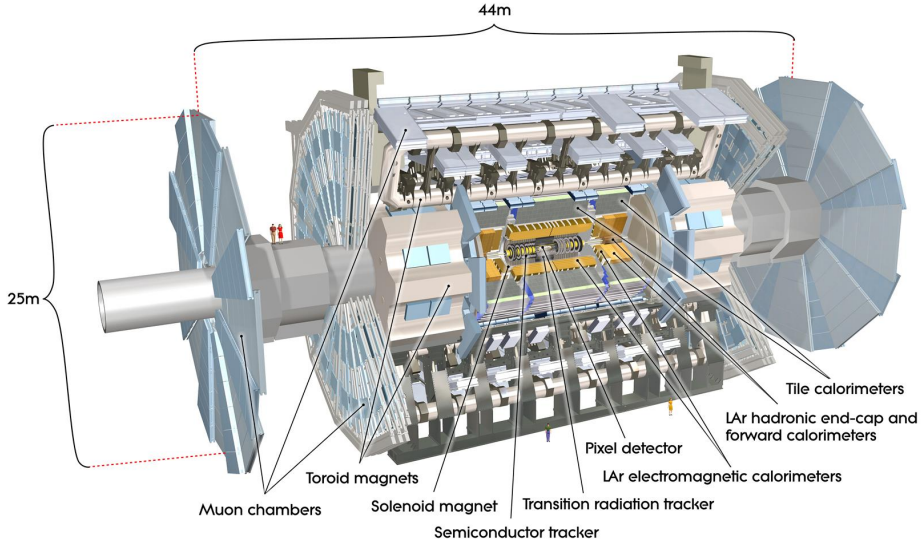


Figure 2.2: The ATLAS detector showing various sub-detector systems.

to as the transverse plane. The positive x-axis points from the IP to the center of the LHC ring, and the positive y-axis is defined as pointing upward. The azimuthal angle  $\phi$  is defined as the angle from the x-axis in the x-y plane. The polar angle  $\theta$  is defined as the angle from the positive z-axis, and it is also expressed as pseudo-rapidity  $\eta$ ,

$$\eta = -\ln(\tan(\frac{\theta}{2})), \quad (2.1)$$

which is a particularly useful quantity because of Lorentz invariance under a boost along the z axis. The distance  $\Delta R$  is defined in  $\eta$ - $\phi$  plane as  $\Delta R = \sqrt{\Delta\eta^2 + \Delta\phi^2}$ .

### 2.2.2 The Inner Detector

The Inner Detector (ID) is a particle tracker designed to measure the charge and momentum of charged particles and to reconstruct the primary and secondary vertices. It consists of cylindrical barrels and two end-cap disks from three sub-detectors centered around the IP. The ID covers the pseudo-rapidity region  $|\eta| < 2.5$ .

The detector is immersed in a 2 T magnetic field generated by a superconducting solenoid magnet, and the magnetic field is used to bend trajectories of charged particles. The transverse momentum and the charge of a particles are then determined from the curvature of the trajectory.

The sub-detectors of the ID, the Pixel tracker, the semiconductor tracker (SCT), and the transition radiation tracker (TRT), are discussed in the following sections.

## Pixel Detector

The Pixel detector is a semiconductor detector in the innermost part of the ATLAS tracking system. The detector consists of 4 concentric layers of barrel detectors and 3 disk detectors at each end-cap region. The barrels and disks are made of a rectangular Pixel modules containing 80.4 millions pixels of the size  $50 \times 400 \mu\text{m}^2$  (6 millions pixels of the size  $50 \times 250 \mu\text{m}^2$  for the IBL) [29]. As a charged particle traverse through pixels, the currents generated by ionizing electrons are measured and registered as hits. The pixels provide spatial information with resolution of  $\sim 8 \mu\text{m}$  in radial direction and  $\sim 75 \mu\text{m}$  in the beam axis, and the information is used for momentum measurements as well as reconstruction of primary and secondary vertices. In Run 2, the Insertable B-Layer (IBL) [30] was installed to maintain and improve the performance of the ATLAS detector under increasing pile-up.

## Semi-conductor Tracker

The SCT is the next tracking system following the Pixel detector. Similar to the Pixel detector, the SCT consists of 4 layers of barrel detectors and 9 disk detectors at each end-cap region [31, 32]. Each barrel/disk is made of SCT modules containing double-sided silicon strips, measuring  $80 \mu\text{m}$  wide and  $12 \text{ cm}$  long<sup>1</sup>. Strips are positioned parallel (perpendicular) to the beam axis in the barrel (end-cap) region. Because a single strip can only provide spatial information in ( $r$ - $\phi$ ) direction in barrel and ( $z$ - $\phi$ ) direction in end-cap region, double-sided strips are displaced by a relative angle of 40 mrad to provide three-dimensional spatial measurements of charged particles. The SCT has a spatial resolution of  $17 \mu\text{m}$  in radial direction and  $580 \mu\text{m}$  in  $z$  direction. The information collected by the SCT is used for charge and transverse momentum measurements and reconstruction of vertices.

## Transition Radiation Tracker

The TRT is the outermost tracking system in the ID, covering the region  $|\eta| < 2.0$ . The barrel region is covered by 52,544 straw tubes aligned parallel to the beam axis. The end-cap region is covered by 122,800 straw tubes aligned in radial direction. Each straw tube is filled with a Xe-based gas mixture, and a wire is placed at the center of the tube, acting as an anode. When a charged particle traverses the detector, it ionizes the gas mixture inside

<sup>1</sup>There are two versions of SCT strips in end-cap modules with lengths of 7 and 12 cm.

straws, producing a cascade of electrons. These electrons from the ionization drift toward the center wire, creating signal for the readout electronics with the intrinsic resolution of a single straw tube of  $\sim 120 \mu\text{m}$  [33].

The TRT also provides important information on particle identification. The spaces between straws are filled with polymer fiber (barrels) and foils (end-caps) for the production of transition radiation. When a highly relativistic charged particle passes through them, photons may be emitted by transition radiation, and these photons can be absorbed by the gas mixture, resulting in higher readout signals than usual, called high-threshold hits. The effect is stronger for electrons due to larger relativistic factor ( $\gamma = E/m$ ) than particles with a lower boost such as hadrons. Therefore, the high-threshold hits in the TRT can be used for electron/pion identification [34].

### 2.2.3 The Calorimeters

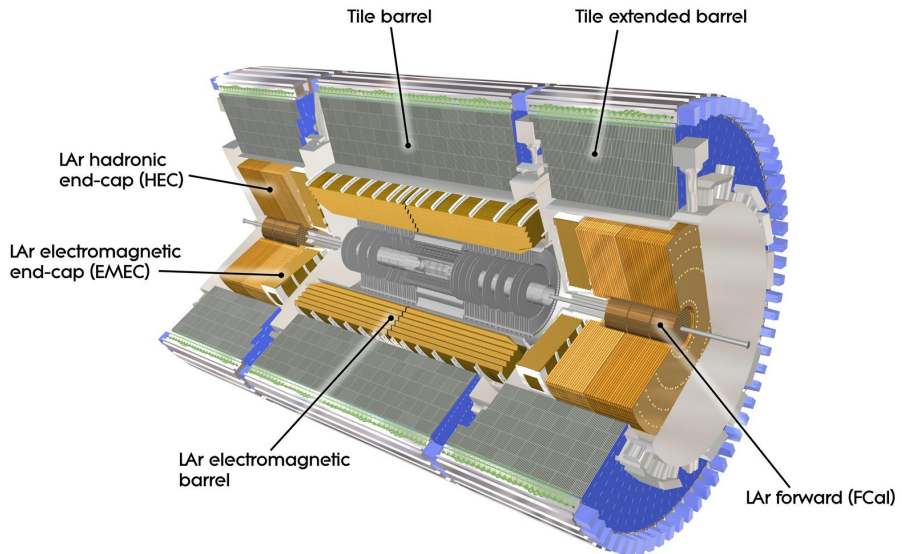


Figure 2.3: The ATLAS calorimeter system.

The ATLAS calorimetry system, shown in Figure 2.3, consists of two sub-systems, the Liquid Argon (LAr) calorimeters [35] and the tile calorimeters (TileCals) [36]. The calorimeters are designed to measure the energy deposited by a particle as it traverses through the detector, and the signals from calorimeters are also used for the trigger system. Based on

its usage, the calorimeters can be grouped into two sets of calorimeters: the electromagnetic (EM) calorimeters and hadronic calorimeters.

### Electromagnetic Calorimeter

The EM calorimeters (EMCs) are located outside the ID and the solenoid magnet, and they are designed to measure the energy deposition from electrons and photons. They are composed of two LAr calorimeters, the EM End-Cap calorimeter (EMEC) covering the region of  $|\eta| < 1.475$  and the EM Barrel (EMB) calorimeter covering the region of  $1.375 < |\eta| < 3.2$ . The LAr calorimeters are composed of layers of high density material (Pb) and LAr sampling layer interspaced for absorption of electron/photons and energy measurement, respectively. The first layer of the LAr calorimeters is called *presampler* which is a thin layer of liquid argon without absorber in front, and it is used to correct for the energy loss before a particle reaches the calorimeter. The LAr calorimeters measure only a small fraction of the deposited energy by a layer, hence called sampling calorimeters.

When an electron or a photon enters the calorimeters, the electron/photon interacts with the absorber layers, creating the initial EM shower via bremsstrahlung and pair-production. The EM shower is amplified and collected by the sampling layers. The EM calorimeters have the minimum number of radiation length of  $24 X_0$  ( $\text{g cm}^{-2}$ ) [37]. The energy resolution of a calorimeter is described as,

$$\frac{\sigma_E}{E} = \frac{a}{\sqrt{E}} \oplus \frac{b}{E} \oplus c, \quad (2.2)$$

where  $a$  is the coefficient of the sampling term, representing the statistical shower development,  $b$  is the noise term, and  $c$  is the constant term [38]. The EMCs in ATLAS have the energy resolution of  $\frac{\sigma_E}{E} \sim \frac{10\%}{\sqrt{E}} \oplus \frac{170 \text{ MeV}}{E} \oplus 0.7\%$  for electrons.

### Hadronic Calorimeter

Hadrons are less likely to produce bremsstrahlung radiation due to heavier mass, and they can traverse through the EMC without losing significant energy. Therefore, the hadronic calorimeters are located outside the EMC to measure the energy of hadrons penetrating the EMC. The hadron calorimeters are composed of both LAr calorimeters and TileCals.

The hadronic LAr calorimeters consists of two parts, the hadronic end-cap calorimeter (HEC) covering the region of  $1.5 < |\eta| < 3.2$  and the forward calorimeter (FCAL) covering the region of  $3.1 < |\eta| < 4.9$ . The principal of hadronic LAr calorimeters is the same as EM

LAr calorimeters. The HEC is divided into four longitudinal layers with copper absorber. The FCAL consists of one EM layer with copper as absorber and two hadronic layers with tungsten as passive material. When a hadron enters the hadronic LAr calorimeters, the particle interacts with nuclei of the absorber material via strong force, creating a hadronic shower. The hadronic shower is sampled by sampling layers.

TileCals are designed to cover the central barrel region ( $|\eta| < 1.0$ ) and the extended barrel region ( $0.8 < |\eta| < 1.7$ ). The TileCals are made of alternating layers of iron and scintillating tiles. Hadrons entering the absorber layers produce hadronic showers, and the secondary particles from the showers interact with the scintillating tiles to produce lights. The photons are delivered to photomultipliers via wave-length shifting fibers and registered as calorimeter cluster hit. The TileCals have the energy resolution of  $\frac{\sigma_E}{E} \sim \frac{50\%}{\sqrt{E}} \oplus 6\%$  for pions.

The TileCals, combined with the hadronic LAr calorimeters, provide measurement of hadrons, jets, taus, and missing transverse energy ( $E_T^{miss}$ ).

#### 2.2.4 The Muon Spectrometer

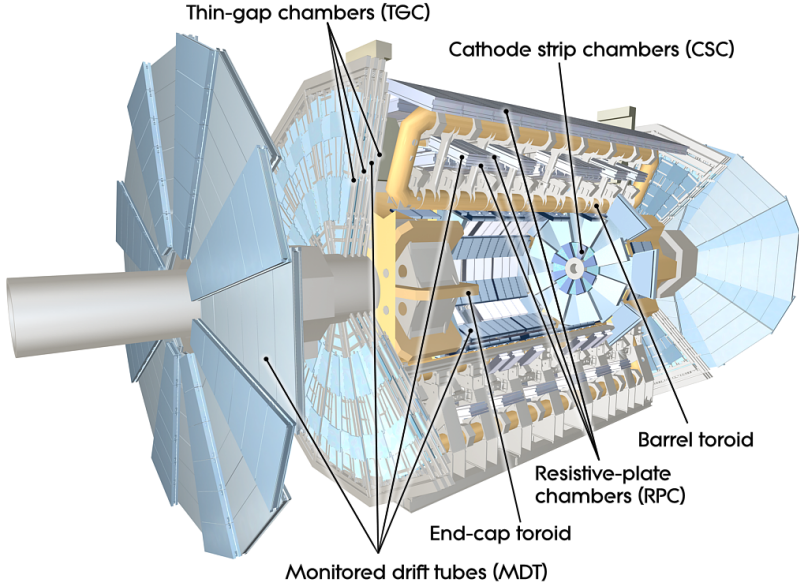


Figure 2.4: The ATLAS Muon Spectrometer

The Muon Spectrometer (MS) is the outermost detector in the ATLAS detector, responsible for muon identification, momentum measurements, and muon trigger information. The

MS is designed to provide high  $p_T$  momentum measurement with resolution of  $\sigma_{p_T}/p_T = 10\%$ , independent from the ID. The MS consists of four sub-detector systems. The Resistive Plate Chambers (RPCs) and the Thin Gap Chambers (TGCs) are used for muon triggering. The Monitored Drift Tubes (MDTs) and the Cathode Strip Chambers (CSCs) allow precise tracking and momentum measurements. The MS barrel region covers the region of  $|\eta| < 1$ , and the coverage is extended to  $|\eta| < 2.7$  in the end-cap. Magnetic field of 0.5 T [39] is provided by a system of a large toroidal magnet (barrel) and two smaller toroidal magnets (end-cap). A layout of the MS is shown in Figure 2.4.

### **Monitored Drift Tube Chambers**

The MDT chambers provide precision momentum measurements using chambers of drift tubes filled with a gas mixture of Ar (97%) and CO<sub>2</sub>(3%). The barrel MDT chambers are arranged in three layers, covering the region of  $|\eta| < 1.1$ . The end-cap MDT chambers are arranged in three wheels, covering the region of  $1.1 < |\eta| < 2.7$ . Each chamber has 6-8 layers of drift tubes of 3 cm in a diameter, and a tungsten-rhenium wire is placed at the center as an anode. The principal of particle detection is similar to the TRT, but the drift tubes are arranged perpendicular to the beam axis in the barrel layers and tangential in the end-cap layers. This configuration allows the MDT to measure the curvature of a muon in  $\eta$ - $z$  plane under the toroidal magnetic field.

### **Cathode Strip Chambers**

The CSCs are located on the innermost wheel of the end-caps, covering the region of  $2.0 < |\eta| < 2.7$ . In this region, the MDTs would not operate properly due to the high rates of muons at this region. Instead, sixteen CSCs on each end-cap provide precise tracking for high density muons with the resolution of 60  $\mu\text{m}$  in  $\eta$ - $z$  plane and 5 mm in the radial direction. The CSCs are multi-wire proportional chambers with segmented cathode strips in alternating alignment. The multi-wires are aligned in the radial direction, and the strips are aligned perpendicular or parallel to the wires to provide 2 dimensional measurements in both  $\eta$  and  $\phi$  directions.

### **Resistive Plate Chambers**

The RPCs provide trigger capability for the muon trigger and measurements in  $\eta$ ,  $\phi$  co-ordinates in the barrel region. There are three RPCs arranged in concentric cylindrical shells around the beam axis. The two inner RPCs are placed at the radii of 5 and 7.5 m to

provide the low- $p_T$  trigger information. The outer RPCs are installed at the radius of 10 m to provide high- $p_T$  trigger information. Each chamber consists of two parallel resistive plates separated by a 2 mm gap filled with a gas mixture based on C<sub>2</sub>H<sub>2</sub>F<sub>4</sub>. A muon track passing through the RPCs ionizes the gas, and the signal is multiplied and read out by each chamber, providing 6 measurements for each track.

### Thin Gap Chambers

The TGCs are designed to provide trigger information and  $\phi$  measurements (non-bending direction) in the end-cap region. Similar to the CSCs, the TGCs are made of multi-wire proportional chambers filled with a gas mixture of 55% CO<sub>2</sub> and 45% C<sub>5</sub>H<sub>12</sub>. The strips are oriented in radial direction, allowing measurements in  $\phi$ . The TCGs consists of 4 layers of chambers on each end-cap, covering the region of  $1 < |\eta| < 2.7$ .

### 2.2.5 The ATLAS Magnet

The ATLAS detector has three major superconducting magnet systems surrounding the ID and the MS: the Central Solenoid magnet and the Barrel/End-cap Toroid magnets.

#### Central Solenoid Magnet

The Central Solenoid magnet surrounds the ID, producing a 2 T magnetic field. The solenoid is designed to bend the trajectory of a charged particle in  $r$ - $\phi$  plane. The curvatures of charged particles are used for the measurements of charge-to-momentum ratio. The solenoid magnet measures 2.4 m in diameter and 5.3 m in length, and 7.73 kA of current is applied to generate the solenoidal magnetic field.

#### Toroid Magnets

In the outer region of the ATLAS detector, two superconducting toroid magnet systems are used to generate a magnetic field within the MS. The barrel toroid are composed of 8 separate coils made of Al/NbTi/Cu conductor with 120 turns. The toroid measures 20.1 m in diameter and 25.3 m in length. The end-cap toroid has 8 coils with 116 turns, and the coils are made of the same material as the barrel toroid. The nominal current of 20.5 kA is applied to generate a magnetic field of 1-2 T with the field integral of 2 to 8 Tm.

## 2.3 The ATLAS Trigger System

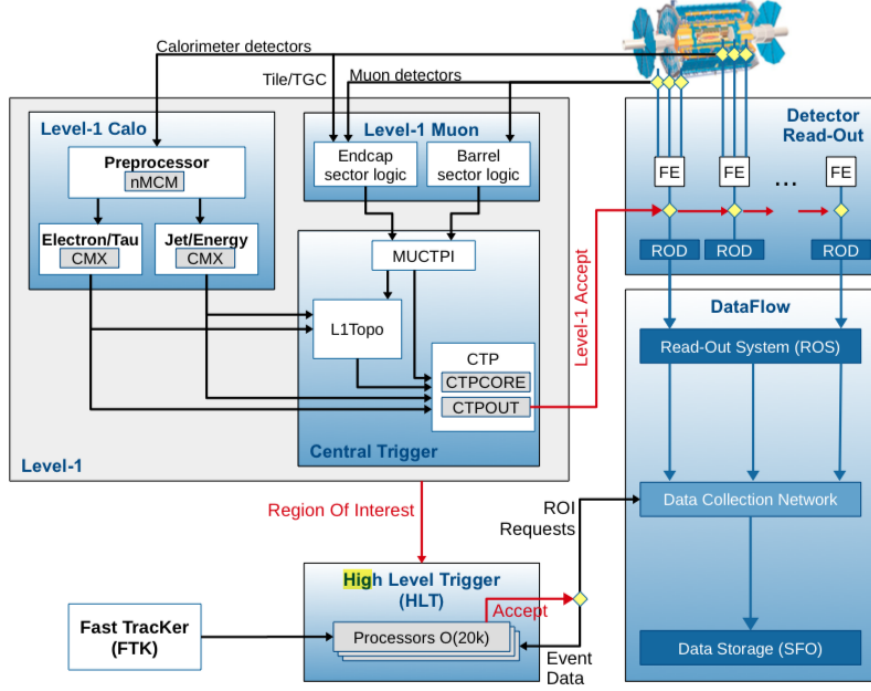


Figure 2.5: Layout of the ATLAS Trigger and data acquisition system in Run 2.

The ATLAS trigger system is designed to select interesting events from raw event data at high rate, generated by  $pp$  collisions. In Run 2, the LHC collide proton bunches every 25 ns, resulting in about a billion  $pp$  collisions per second at  $\langle \mu \rangle = 24.9$  (in 2016). Due to the limited bandwidth and computing resources, it is impossible to record all events from the collisions. Therefore, the ATLAS trigger system is implemented to reduce the data taking rate from 40 MHz to 100 kHz. In Run 2, several upgrades have been performed in both hardware and software to maintain data quality in the environment with increasing pile-up, higher instantaneous luminosity at the center-of-mass energy of  $\sqrt{s} = 13$  TeV.

The trigger system in Run 2 consists of a hardware-based Layer 1 (L1) trigger and a software-based High Level Trigger (HLT). Figure 2.5 shows the ATLAS trigger and data acquisition system in Run 2. The events accepted by the trigger system are further processed by the Data Acquisition (DAQ) system where the information from front-end electronics of each detector component are used to build an individual event. The reconstructed events from DAQ are sent to Data Storage (SFO) for permanent storage.

### 2.3.1 Level 1 Trigger

The L1 trigger is a hardware-based trigger system that operates at the maximum rate of 100 kHz [40]. The main components of the L1 trigger consist of the L1 calorimeter trigger system and the L1 muon trigger system . The L1 trigger uses custom electronics to make fast decisions and find regions of interest (RoI) in the detector where potentially interesting activities are registered in the calorimeters or the MS.

A list of trigger selection is developed based on the physics goal of the collaboration and the needs of individual analyses. The list is called the Trigger Menu [41]. The L1 trigger accepts the events with high  $p_T$  tracks, jets, or large  $E_T^{miss}$  that satisfies one of the trigger menu. The events accepted by the L1 trigger is passed to the software-based trigger system.

### 2.3.2 High Level Trigger

The HLT makes the decision on events based on full information from the detector read-out in the RoI passed by the L1 trigger. This includes a fast reconstruction of the ID tracks. The HLT has the average output rate of 1 kHz [40], constrained by data storage limitation.

### 2.3.3 Summary of the ATLAS Detector

The most relevant part of the ATLAS detector in this search is the ID where a long-lived  $Z'$  decaying to a dilepton pair can be reconstructed as a displaced vertex. The Pixel detector, the innermost detector within which most  $Z$ 's decay, has the spatial resolution of 8 and 75  $\mu\text{m}$  in  $r$  and  $z$  direction, respectively. The TRT detector is used to identify electrons from pions with the spatial resolution of 120  $\mu\text{m}$  in  $\phi$  direction. The EMC is used to identify electrons by combining the energy deposit of an electron with the track reconstructed in the ID, referred as *ID tracks*. The EMC has the energy resolution of  $\frac{\sigma_E}{E} \sim \frac{10\%}{\sqrt{E}} \oplus \frac{170 \text{ MeV}}{E} \oplus 0.7\%$ . The MS is used to reconstruct muons by combining the ID tracks with the tracks reconstructed within the MS. The MS has the spatial resolution of 30  $\mu\text{m}$  from a single drift tube and the energy resolution of  $\sigma_{pT} = 10\%$  at 1 TeV. The specification of these sub-detectors are summarized in Table 2.1.

Sub-detector	Spatial resolution ( $\mu\text{m}$ )	Energy/momentum resolution	Particle identification
Pixel	8 in $r$ , 75 in $z$		
SCT	17 in $r$ , 580 in $z$	$\frac{\sigma_p}{p} = \frac{4.83 \pm 0.16}{10^4 \text{ GeV}} \times p_T$ [42]	
TRT	120 in $\phi$		$e / \pi$
LAr	-	$\frac{\sigma_E}{E} \sim \frac{10\%}{\sqrt{E}} \oplus \frac{170 \text{ MeV}}{E} \oplus 0.7\%$	$e, \gamma$
MS	30 (single tube)	$\sigma_{pT} = 10\%$ at 1 TeV	$\mu$

Table 2.1: The spatial, energy resolution and the particle identification of the Atlas detector.

# Chapter 3

## Z' RECONSTRUCTION

The experimental signature in the search for long-lived  $Z'$  is characterized by a dilepton vertex with high  $p_T$  leptons, displaced ( $> 2$  mm) from the primary vertex in transverse plane, referred a *displaced vertex*. In this chapter, the reconstruction of displaced vertices in the ATLAS ID is described.

### 3.1 Track Reconstruction in the Inner Detector

Track reconstruction in the ATLAS uses pattern recognition algorithms to reconstruct the trajectories of charged particles, referred as a *track*. When a charged particle traverse through the ID, the particle interact with the sub-detectors of the ID (Pixel, SCT, and TRT), leaving raw detector signals. The raw signals are digitized and registered as detector *hits*, and these detector hits are used for track reconstruction.

#### 3.1.1 Standard Tracking

The standard ATLAS track reconstruction is the main track reconstruction algorithm used in the ATLAS experiment. In the first stage of the track reconstruction, detector hits from the Pixel or the SCT detector are used to create *track seeds*, collections of silicon hits used for the initial track finding. If a track seed passes certain quality criteria, including a  $p_T$  and impact parameter selection, the track seed is extended to the outer part of the ID using a window search and pattern recognition algorithms. The extended tracks are evaluated based on  $p_T$ , number of hits, and impact parameters, and only the tracks satisfying the standard track selections are stored in the track collection. Figure 3.1 illustrates detector hits and reconstructed tracks in the ID. The important standard track selections is summarized in

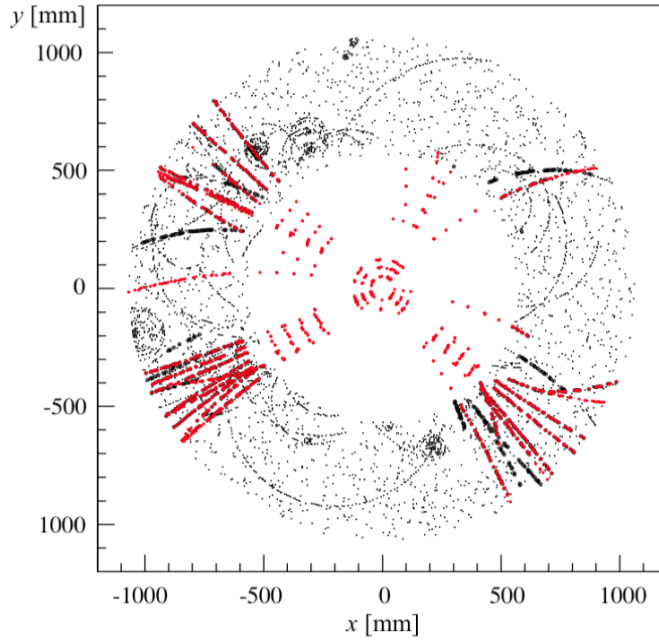


Figure 3.1: Illustration of detector hits and reconstructed tracks in the ID. The bright colors represent the detector hits associated with reconstructed tracks.

Table 3.1 [43].

Tracks are described by five parameters (helix) and a reference point, using a perigee representation [44]. The parameters are the transverse (longitudinal) impact parameter  $d_0$  ( $z_0$ ), the azimuthal angle  $\phi$ , the polar angle  $\theta$ , and the charge-to-momentum ratio,  $q/p$ . The average position of the  $pp$  interaction, referred as beamspot position, is used as the reference point for the track representation [45].

	Standard	Large radius
Maximum $d_0$ (mm)	10	300
Maximum $z_0$ (mm)	250	1500
Maximum $ \eta $	2.7	5
Maximum shared silicon modules	1	2
Minimum unshared silicon hits	6	5
Minimum silicon hits	7	7

Table 3.1: Main track selection in the standard and large radius tracking algorithms.

### 3.1.2 Large Radius Tracking

The standard track reconstruction is proven to be very efficient in Run 2 with the tracking efficiency  $> 90\%$  [46]. However, the tracking algorithm is optimized for charged particles promptly produced from the primary interaction, and the strict requirements on the impact parameters,  $d_0$  and  $z_0$ , limit the tracking efficiency for charged particles with large impact parameters ( $|d_0| > 2$  mm). Therefore, a dedicated track reconstruction algorithm, referred to as the large radius tracking (LRT), is developed to improve the track reconstruction efficiency for the tracks highly displaced from the primary vertex.

The LRT is performed in a sequence, following the standard tracking. It follows the same reconstruction strategy as the standard tracking, but there are a few important differences between the standard tracking and the LRT:

- The pattern recognition algorithms in the LRT only uses *un-used* hits, the silicon hits that have not been used in the standard tracking, in creating and extending track seeds.
- The requirements on tracks such as  $d_0$ ,  $z_0$ , and number of hits are relaxed.

Tracks reconstructed by the LRT using un-used hits are required to pass certain criteria such as minimum  $p_T$  and number of detector hits, and the selected tracks are merged into the standard track collection for the next step of reconstruction. The track selections in the LRT are summarized and compared with the standard track reconstruction in Table 3.1. The combined track collection is used as an input for the lepton reconstruction and identification and secondary vertex reconstruction. More details on the LRT can be found in Ref. [43].

Combined with the standard track reconstruction, the LRT provides overall efficiency of  $> 90\%$  for the particles that satisfy the fiducial selections in Table 3.2 with a displacement in the transverse plane up to 300 mm.

Fiducial Selections		
$r_{\text{prod}}$	<	300 mm
$ \eta $	<	5
$p_T$	>	1 GeV
Number of silicon hits	$\geq$	7

Table 3.2: Fiducial selections on particles for tracking efficiency measurements.

## 3.2 Electron Reconstruction

Electrons are characterized by energy deposits in the EM calorimeter and the associated reconstructed tracks in the ID. The electron reconstruction algorithm uses the energy deposits with total transverse energy  $> 2.5$  GeV in a window of  $0.075 \times 0.125$  in  $(\eta, \phi)$  to reconstruct EM clusters. The EM clusters are associated with tracks within the same RoI,  $|\Delta\eta| < 0.05$  and  $|\Delta\phi| < 0.1$  where the effect of bremsstrahlung is taken into account [47]. In the absence of a matching track, the EM cluster is classified as a photon candidate. The associated pairs of tracks and energy clusters are refitted to improve the energy resolution of the electron candidate. Additional electron requirements, including likelihood-based identification criteria, are imposed on the electron candidates to reduce misidentification.

## 3.3 Muon Reconstruction

Muons deposit very little energy in the calorimeter as they traverse through the detector due to the relatively larger mass, given that the probability of bremsstrahlung is  $\propto 1/m^2$ . However, they leave tracks in both the ID and the MS, referred as inner detector (ID) tracks and muon standalone (MS) tracks. The muon reconstruction algorithm uses MS tracks as seeds, and the MS tracks are extrapolated to the ID for the association with ID tracks. A *combined muon* track is created if a MS track is successfully associated with an ID track after the momentum correction for the energy loss from the interaction with the detector material. There are other types of reconstructed muons such as standalone muons, segment-tagged muons, and calorimeter-tagged muons [48]. However, these types of muons are not considered in this analysis as they do not have associated ID tracks which are required for the reconstruction of displaced vertices.

By default, muons are required to have a minimum number of pixel and SCT hits, as well as small transverse impact parameters. This is not optimal for the searches that aim to detect displaced vertices as the decay products of displaced vertices tend to have large impact parameters ( $d_0, z_0$ ) and missing hits in the inner layers of the detector. Therefore, the requirements on  $d_0$  and pixel hits are removed. Also minimum SCT hits on muon tracks are lowered to 2.

## 3.4 Secondary Vertex Reconstruction

In the LHC, when two proton bunches collide, several different vertex topologies arise. The primary vertex and several pile-up vertices are formed along the beam line, and the vertices

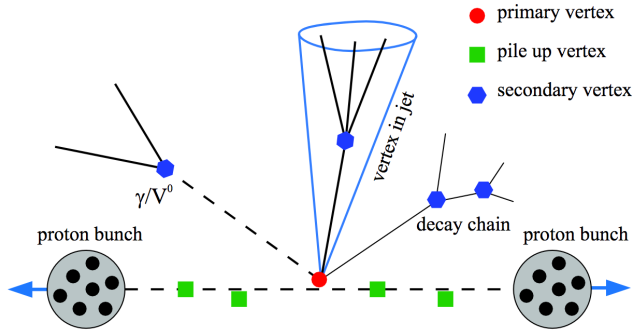


Figure 3.2: Main vertex topologies in  $pp$  collisions: primary, pile-up, and secondary vertices.

from photon conversion or long-lived particles are formed displaced from the primary vertex as shown in Figure 3.2. These displaced vertices are referred as secondary vertices. In the search for long-lived  $Z'$  in the dilepton decay channel, the decay products of long-lived particles can be reconstructed as a secondary vertex.

The secondary vertex reconstruction is based on the primary vertex reconstruction algorithm [49] and was originally developed for the study of material mapping of the ID in Run I. The algorithm was updated for several long-lived particle searches in Run 2.

In the first stage, track are selected using the requirements on track parameters and hit patterns shown in Table 3.3. In addition, tracks are required to have  $p_T > 1$  GeV to reduce low  $p_T$  tracks from a photon conversion, and track quality requirement is relaxed ( $\chi^2/DOF < 50$ ) to improve the efficiency of reconstructing displaced vertices. The tracks reconstructed by both the standard track reconstruction and the LRT are used as input. The tracks passing the track requirements are used to create two-track vertices, based on the closeness of two tracks in space. This process results in a large number of fake vertices. The fake vertices are rejected by considering the location of a vertex and hit patterns of the tracks associated with the vertex. A vertex is rejected if the associated tracks have any hits at a radius smaller than the vertex position. Two-track vertices passing the fake rejection are refitted using a Kalman Filter [50] for precise vertex position measurements, and track parameters are calculated with respect to the secondary vertex.

The two-track vertices reconstructed by the secondary vertex reconstruction serve as the primary analysis object in this thesis.

Variable	Cut
$p_T$ (GeV)	> 1.0
$\chi^2/DOF$	< 50
$d_0$ (mm)	2.0 - 300.0
$z_0$ (mm)	< 1500.0
SCT hits	$\geq 2$
Si shared hits	$\leq 2$
Pixel and TRT hits	TRT hits > 0 or Pixel hits $\geq 2$

Table 3.3: Track requirements for secondary vertex reconstruction.

# Chapter 4

## ANALYSIS OVERVIEW

This thesis presents a search for a heavy long-lived resonance decaying to a dilepton pair,  $\mu^+\mu^-$ ,  $e^+e^-$ , or  $e^\pm\mu^\mp$  within the ATLAS ID. The analysis uses  $32.8 \text{ fb}^{-1}$  of  $pp$  collision data at  $\sqrt{s} = 13 \text{ TeV}$  collected in 2016 with the ATLAS detector. The long-lived particle (LLP) is referred as  $Z'$  but with no assumption on the  $Z'$  production mechanism for a model-independent search.

There have been several searches for the LLPs produced in  $pp$  collisions in Run I at  $\sqrt{s} = 8 \text{ TeV}$ , including the search for displaced hadronic jet [51], displaced heavy flavors [52], or multi-track displaced vertex [53], and no significant excess was observed. The signature considered in this analysis is distinct from the previous searches, and it is one of the first efforts in the ATLAS experiment to search for a generic displaced vertex signature decaying to a dilepton pair. This analysis focuses on interpreting the LLPs decaying to displaced dilepton vertices in the context of model-independent, exotic resonance search.

In this search, a special setup (described in Section 3.1.2) of data reprocessing and reconstruction is used in order to gain sensitivity for the non-conventional signature of LLPs. The special setup allows the reconstruction of tracks with large impact parameters and secondary vertices significantly displaced from primary vertices.

# Chapter 5

## DATA AND MC SAMPLES

### 5.1 Data samples

The analysis uses the 2016  $pp$  collisions data (periods A-L) with the integrated luminosity of  $32.8 \text{ fb}^{-1}$ . In this search, because the standard ATLAS track reconstruction does not provide good sensitivity for long-lived particles, a dedicated data *stream*, `DRAW_RPVLL`, is used to reconstruct events using the non-standard reconstruction as described in Chapter 3. The stream is used in several Exotics and SUSY analyses, searching for long-lived particles.

In this stream, a subset of events from the *main* physics stream [54], a data stream used for common physics analyses in ATLAS, is selected by a set of offline filters, called `RPVLL` filters. The filters select events using the HLT and offline selections configured for each analysis. The triggers and offline selection used in this search is discussed in Chapter 6. The selected events are passed downstream for reconstruction. The data is in `RAW` format so that low-level information such as detector hits can be used for the special reconstruction algorithms to reconstruct displaced tracks and vertices.

The events passing HLTs are processed by a sequence of reconstruction algorithms with varying configurations, and the ATLAS metadata interface (AMI) tags are used to specify the configurations to be used for a data processing chain. In this analysis, the events are centrally processed with AMI tag `r8669` in which the dedicated track reconstruction algorithm, the LRT, and the secondary vertex reconstruction algorithm are enabled to reconstruct tracks and vertices, respectively. The output of `DRAW_RPVLL` stream is in `DAOD_RPVLL` format which is a standard `xAOD` data format with additional displaced tracks and secondary vertices reconstructed.

The `DAOD_RPVLL` is further processed to produce the `DAOD_SUSY15` derivation for data

reduction and software fixes on analysis objects such as energy calibration<sup>2</sup>, as recommended by the Analysis Model Study Group (AMSG) [55]. Table 5.1 summarizes datasets used in this search.

Format	Dataset
DRAW_RPVLL	data16_13TeV.*.physics_Main.merge.DRAW_RPVLL.f*_m*
DAOD_RPVLL	data16_13TeV.*.physics_Main.recon.DAOD_RPVLL.f*_r8669
DAOD_SUSY15	data16_13TeV.*.physics_Main.recon.DAOD_RPVLL.f*_r8669_p3185

Table 5.1: Dataset used in DRAW\_RPVLL, DAOD\_RPVLL, and DAOD\_SUSY15 format.

This search uses a modified version of the standard `GoodRunsList` because a small number of events selected by DRAW\_RPVLL were not reconstructed successfully. The corresponding luminosity blocks were removed from the `GoodRunsList`<sup>3</sup>.

The tag and probe studies of Section 7.1 are performed on the standard xAOD dataset using derivations of the performance groups, given in Table 5.2.

Format	Dataset
DAOD_EGAM1	data16_13TeV.*.physics_Main.PhysCont.DAOD_EGAM1.grp16_v01_p3013
DAOD_MUON1	data16_13TeV.*.physics_Main.PhysCont.DAOD_MUON1.grp16_v01_p3043

Table 5.2: Datasets used for tag and probe studies.

## 5.2 MC samples

### 5.2.1 Signal samples

The long-lived  $Z'$  is generated using PYTHIA 8.1/8.2 [56] with the NNPDF23LO PDF set [57] and the min-bias tune A14. In this signal samples,  $Z'$  is singly produced from  $q\bar{q}$  scattering and decays to a  $\mu\mu$ ,  $ee$ , or  $e\mu$  pair. The proper lifetime,  $c\tau$ , is set to 100, 250, or 500 mm. The mass of  $Z'$  is set between 100 and 1000 GeV. A width based on relativistic Breit-Wigner is assumed for the new resonance. A sample of 20k events are generated for each mass and

<sup>2</sup>Software fixes are released by the ATLAS collaboration in the form of `AODfix`.

<sup>3</sup>data16\_13TeV.periodAllYear\_DetStatus-v83-pro20-15\_DQDefects-00-02-04\_PHYS\_StandardGRL\_All\_Good\25ns\_DAOD\_RPVLL\_r8669.xml

lifetime. Table 5.3 summarizes dataset identifiers (DSID), mass, width, and lifetime of the signal MC samples used in this search.

$m_{Z'}$ (GeV)	$\Gamma$ (GeV)	$c\tau$ (mm)	DSID		
			$\mu\mu$	$ee$	$e\mu$
100	2.8	100	308264	309539	309554
100	2.8	250	308265	309540	309555
100	2.8	500	308266	309541	309556
250	6.9	100	301911	309542	309557
250	6.9	250	301912	309543	309558
250	6.9	500	301913	309544	309559
500	14.7	100	301914	309545	309560
500	14.7	250	301915	309546	309561
500	14.7	500	301916	309547	309562
750	23.0	100	308285	309548	309563
750	23.0	250	308286	309549	309564
750	23.0	500	308287	309550	309565
1000	31.0	100	301917	309551	309566
1000	31.0	250	301918	309552	309567
1000	31.0	500	301919	309553	309568

Table 5.3: Mass, lifetime, and DSID of the signal MC samples.

The signal MC samples generated using PYTHIA are processed to include detector simulation using the AMI tags `s2698` and `s2726`. The samples are overlaid with simulated minimum-bias events to model multiple interactions (pile-up) in data samples. In the signal MC samples, the average pile-up,  $\langle \mu \rangle$ , ranges from 10 to 40 with small number of events having  $\langle \mu \rangle < 10$ . The difference in the  $\langle \mu \rangle$  distributions between MC and data samples are corrected for by pile-up reweighting. The resulting MC samples are reconstructed using AMI tag `r8788`.

In the reconstruction process, the LRT and the secondary vertex reconstruction algorithms are used with the same configuration as data samples to reconstruct displaced tracks and vertices. The reconstructed events are stored in `DAOD_RPVLL`, and the samples are processed to produce the `DAOD_SUSY15` derivation for data reduction and software fixes on analysis objects.

The representative plots of generator-level  $p_T$  and  $\eta$  distributions of  $Z'$  and the muons from the decay of the  $Z'$ , referred as *signal* muons, are shown in Figure 5.1 using the signal MC samples with  $m = 500, 1000$  GeV and  $c\tau = 100$  mm.

The  $\eta$  distribution of signal muons shows that most of the signal muons are produced within the detector acceptance ( $|\eta| < 2.7$ ). The characteristic upper edge in the  $p_T$  spectrum is related to the  $Z'$  mass.

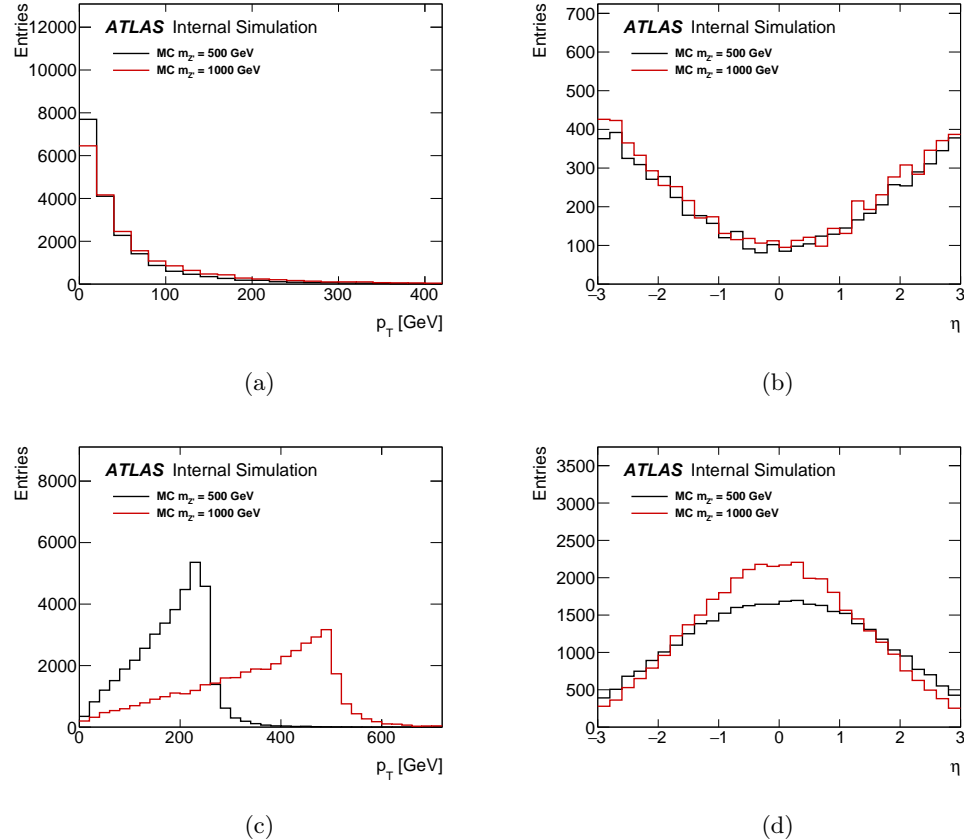


Figure 5.1: Representative plots of generator-level (a)  $p_T$  and (b)  $\eta$  distributions of  $Z'$ , and (c), (d) are the corresponding distributions for the signal muons. The signal MC samples are generated with  $m = 500, 1000$  GeV, and  $c\tau = 100$  mm.

### 5.2.2 Background MC samples

In this analysis, backgrounds are estimated from data because most of the backgrounds are expected to originate from non-collision processes such as cosmic rays or random-crossing of tracks.

However, SM background samples are used to study the performance of random-crossing background estimation (Section 8.2) and to estimate the systematic uncertainties in vertexing

and tracking (Section 9.1). The  $t\bar{t}$  samples are generated for QCD background study using SHERPA 2.2 [58] with the NNPDF30NNLO PDF set. The samples with leptonic decay of di-boson ( $ZZ$ ,  $WW$ ,  $W^\pm Z$ ) are generated using SHERPA 2.1 with the CT10 PDF set. The di-jet samples (JZ3W-JZ6W) are generated in slices of leading jet  $p_T$  (160-400, 400-800, 800-1300, 1300-1800, 1800-2500 GeV) using PYTHIA 8.1 with NNPDF23L0 PDF set. These samples are sufficient for testing purposes, as they contain high- $p_T$  isolated leptons (from  $W$  boson decays) and leptons and displaced tracks in  $b$ -jets, in addition to tracks from pile-up vertices. Details on the PDF sets can be found in Ref. [57].

The SM background samples are reprocessed using the same configuration as the signal MC sample for consistency. The background MC samples used for background and systematic uncertainty estimations are summarized in Table 5.4.

Process	DSID	$\sigma$ (pb)	Events ( $10^6$ )	$\mathcal{L}_{Int}(\text{fb}^{-1})$
$t\bar{t}$	410252	87.8	0.70	7.97
$ZZ \rightarrow \ell\ell\ell\ell$	361063	11.7	0.12	10.3
$W^-Z \rightarrow \ell\ell\ell v$	361064	1.68	0.020	10.2
$W^+Z \rightarrow \ell\ell\ell v$	361066	2.33	0.025	30.0
$WW \rightarrow \ell\ell vv$	361068	12.8	0.13	1.95
JZ3W	361023	$8.45 \cdot 10^3$	0.20	0.0247
JZ4W	361024	135	0.20	1.48
JZ5W	361025	4.20	0.20	47.6
JZ6W	361026	$2.42 \cdot 10^{-2}$	0.20	826

Table 5.4: Background MC samples used in the study of random-crossing background and in the estimation of tracking and vertexing systematic uncertainty.

Additional samples are used without the special reconstruction to study the efficiency of the triggers using tag-and-probe method (Section 7.1). These samples are given in Table 5.5.

Format	Dataset
DAOD_EGAM1	mc15_13TeV.361106.PowhegPythia8EvtGen_AZNLOCTEQ6L1_Zee.merge.DAOD_EGAM1.e3601_s2576_s2132_r7725_r7676_p3012
DAOD_MUON1	mc15_13TeV.361107.PowhegPythia8EvtGen_AZNLOCTEQ6L1_Zmumu.merge.DAOD_MUON1.e3601_s2576_s2132_r7725_r7676_p3045

Table 5.5: Background MC samples without the LRT used for tag and probe studies.

# Chapter 6

## SIGNAL SELECTION

The primary physics objects of this analysis are muons, electrons, and dilepton displaced vertices (DVs). In this section, the signal selection criteria for these physics objects are described.

### 6.1 Event preselection

Events are pre-selected in data processing using a combination of offline triggers and custom filters, called `DRAW_RPVLL`. The selected events from the main physics stream are reprocessed for the special reconstruction. The filters are designed to select events containing displaced vertex candidates while maintaining reasonably low filter rates ( $< 30$  Hz). A single photon ( $\gamma$ ), single electron ( $e$ ), di-photon ( $\gamma\gamma$ ), di-electron ( $e^+e^-$ ), and the combination of photon and electron ( $e\gamma$ ) filters are used to select events with  $e^+e^-$  or  $e^\pm\mu^\mp$  candidates of interest. A single  $\mu$  filter is used to select events with  $\mu^+\mu^-$  or  $e^\pm\mu^\mp$  candidates of interest.

The filters require events to pass one of the HLTs listed in Table 6.1. Most of the HLTs developed in ATLAS are designed for prompt searches, and there are implicit requirements on particles to point back to the IP. Therefore, the triggers with no requirement on ID tracks are used to increase the sensitivity to electrons and muons with large transverse and longitudinal impact parameters,  $d_0$  and  $z_0$ . Consequently, the muon trigger that only uses the muon spectrometer information is used to trigger displaced muons. The photon triggers are used to trigger displaced electrons so that only the calorimeter information is used.

In addition to the HLT requirements, each filter requires offline selections on particles such as  $p_T$ ,  $|\eta|$ , and  $d_0$ . The single photon ( $\gamma$ ) or electron ( $e$ ) filters require a leading photon or electron, respectively, with  $p_T > 150$  GeV,  $|\eta| < 2.5$ , and  $d_0 > 2.0$  mm. These filters also

Description	Trigger
Single photon	HLT_g140_loose
Di-photon	HLT_2g50_loose
Single muon	HLT_mu60_0eta105_msonly

Table 6.1: HLts used to select events in `DRAW_RPVLL` filter. The single photon trigger requires one photon with  $p_T > 140$  GeV. The di-photon trigger requires two photons with  $p_T > 50$  GeV. The single muon trigger requires one muon with  $p_T > 60$  within  $|\eta| < 1.05$  using MS information only.

require a second photon or lepton with  $p_T > 10$  GeV and  $|\eta| < 2.5$  to keep the filter rate reasonably low. The single muon  $\mu$  filter requires a muon with  $p_T > 60$  GeV,  $|\eta| < 2.5$ , and  $d_0 > 1.5$  mm. The di-photon ( $\gamma\gamma$ ), di-electron ( $e^+e^-$ ), and the combination of photon and electron ( $e\gamma$ ) filters require two photons/leptons with  $p_T > 50$  GeV,  $|\eta| < 2.5$ , and  $d_0 > 2.0$  mm. The offline selection is summarized in Table 6.2.

Filter	Leading			Second		
	$p_T$ (GeV)	$ \eta $	$d_0$ (mm)	$p_T$ (GeV)	$ \eta $	$d_0$ (mm)
$\gamma, e$	> 150	< 2.5	> 2.0	> 10	< 2.5	-
$\mu$	> 62	< 2.5	> 1.5	-	-	-
$\gamma\gamma, e^+e^-, e\gamma$	> 55	< 2.5	> 2.0	> 55	< 2.5	> 2.0

Table 6.2: RPVLL filter offline selection on photon and leptons.

The events selected by the RPVLL filters are passed downstream for the special reconstruction process, and the physics objects such as electron, muon, and secondary vertices are reconstructed for analysis.

### 6.1.1 Event selection

At analysis-level, minimum requirements are placed on events based on the quality of events, completeness of the corresponding luminosity blocks, primary vertex, and HLts used in this analysis. In addition, a cosmic veto is applied to reject events with back-to-back muons. The event selection is described below.

- `GoodRunsList` removes events from incomplete luminosity blocks.
- Event cleaning removes corrupted/bad events due to problems in TileCal, LAr calorime-

ter noise bursts, and detector downtimes.

- Events are required to pass one of the HLTs listed in Table 6.1.
- At least one primary vertex is required along the beam line ( $z < 200$  mm).
- Events are rejected if there is a pair of leptons with  $R_{\text{CR}} = \sqrt{(\Delta\phi - \pi)^2 + (\Sigma\eta)^2} < 0.01$ .

### 6.1.2 Muon and electron requirements

The analysis searches for displaced vertices with two leptonic tracks,  $\mu^+\mu^-$ ,  $e^+e^-$ , and  $e^\pm\mu^\mp$ . Prior to applying the vertex level selections, tracks from vertices are required to pass muon or electron selections based on track quality, kinematics, and lepton identification criteria.

Electron requirements are based on the recommendations from the Electron-Gamma (EG) group with an optimization for electrons with large impact parameters. Electrons are rejected if there is a bad cluster associated with an electron. Basic kinematic cuts are applied to electrons,  $|\eta| < 2.47$  and  $p_T > 10$  GeV. The EG group provides several electron identification criteria, called working points, based on a likelihood discriminant to suppress background electrons originating from photon conversions and heavy flavour decays. In this analysis, the electron `LooseLH` working point is used, but the requirements on  $d_0$  and silicon hits are removed to improve electron detection efficiency at large impact parameters.

Muon requirements are based on the recommendations from the Muon Combined Performance group with similar optimizations as electrons. The muon `Loose` working point is used for the identification criteria, and a fiducial cut,  $|\eta| < 2.5$ , and kinematic cut,  $p_T > 10$  GeV, are applied to muons. The requirements on Pixel hits are removed to improve muon detection efficiency at large impact parameter. Muons are required to have an associated ID track for vertex reconstruction. In the case of MC samples, muon momentum resolution and scale corrections are applied to the simulated muons for better agreement between data and simulation [48].

Overlap removal is applied to both muons and electrons to ensure that a ID track is associated with only one muon or electron. The muon and electron requirements are summarized in Table 6.3.

### 6.1.3 Vertex selection

The vertex selection is applied to two-track secondary vertices found in Section 3.4. Secondary vertices with displacement of  $r_{\text{DV}} > 2$  mm from the primary vertex are selected. The selected

<b>Muon</b>	Overlap removal Muon <b>Loose</b> (no requirement on Pixel hits) $ \eta  < 2.5$ $p_T > 10$ GeV Combined Muon
<b>Electron</b>	Overlap removal Bad cluster removal Electron <b>LooseLH</b> (no requirement related to $d_0$ , silicon hits) $ \eta  < 2.47$ $p_T > 10$ GeV

Table 6.3: Muon and electron requirements applied at analysis level.

displaced vertices are made of two tracks which can be any combination of muon, electron, and non-lepton tracks. Therefore, vertices are separated into three vertex types, control, validation, and signal regions.

In the control region, vertices are required to have two non-leptonic tracks ( $x^+x^-$ ). In the validation region, vertices are required to have a muon or an electron and another non-leptonic track ( $\mu^\pm x^\mp, e^\pm x^\mp$ ). In signal region, vertices are required to have a muon pair, an electron pair, or a muon-electron pair ( $\mu^+\mu^-, e^+e^-, e^\pm\mu^\mp$ ). The control region and the validation region are used for background (Chapter 8) and systematic uncertainty (Section 9) estimations. The control, validation, and signal regions are summarized in Table 6.4.

Region	Vertex Type
Control	$x^+x^-$
Validation	$\mu^\pm x^\mp, e^\pm x^\mp$
Signal	$\mu^+\mu^-, e^+e^-, e^\pm\mu^\mp$

Table 6.4: The control, validation, and signal regions defined by the vertex type.

In all regions, vertices are required to pass a common set of vertex selections described as follows. Vertices are required to have  $\chi^2/\text{DOF} < 5$ , which is the default selection used by the Tracking Combined Performance group, to reject poorly reconstructed vertices. A minimum transverse displacement of 2 mm from the primary vertex is required to suppress background from prompt decays. Two tracks from a vertex are required to have opposite electric charges. Vertices within the volume of disabled Pixel module [59] are rejected. Since hadronic interactions of charged particles with detector material produces irreducible backgrounds, the vertices within dense detector material [60] are rejected. The material veto is

not applied to  $\mu^+\mu^-$  vertex due to low probability of muon interaction with detector material. Vertices are also required to be in the detector volume covered by the material mapping ( $r < 300$  mm,  $z < 300$  mm). The invariant mass of the lepton pairs, also referred as vertex mass, is required to have  $m_{\ell\ell} > 10$  GeV to suppress backgrounds from low mass SM particles such as  $J/\Psi$  and  $\Upsilon$ . The vertex mass is calculated by the secondary vertex reconstruction algorithm with the assumption that all tracks are pions. A cosmic veto is applied to vertices by requiring  $R_{\text{CR}} > 0.01$ . The veto is very effective in rejecting cosmic muons reconstructed as back-to-back muon vertices, and the details are discussed in Section 8.1.

In addition to the common vertex selection, at least one electron or muon from the vertex is required to match one of the triggers listed on Table 6.1 and the filters listed on Table 6.2 in the signal region. The vertex selection is summarized in Table 6.5.

<b>Event</b>	GoodRunsList Event cleaning Trigger filter Cosmic veto Primary vertex ( $ z  < 200$ mm)
<b>Vertex</b>	Trigger matching (signal region only) $\chi^2/\text{DOF} < 5$ $r_{\text{DV}} > 2$ mm Opposite charge Disabled module veto Material veto (excluding $\mu^+\mu^-$ ) $m > 10$ GeV $r < 300$ mm, $ z  < 300$ mm Filter matching (signal region only)

Table 6.5: Event and vertex selections applied to select displaced vertices.

# Chapter 7

## SIGNAL EFFICIENCY

A signal efficiency for finding a displaced dilepton vertex is defined by the ratio of the number of events passing the signal selection (Chapter 6) to the total number of events generated. The signal efficiency can be written as,

$$\varepsilon_{\text{overall}} = \varepsilon_{\text{filter}} \cdot \varepsilon_{\text{trigger}} \cdot (\varepsilon_{\text{track}1} \cdot \varepsilon_{\text{lepton}2}) \cdot (\varepsilon_{\text{track}2} \cdot \varepsilon_{\text{lepton}1}) \cdot \varepsilon_{\text{vertex}}. \quad (7.1)$$

$\varepsilon_{\text{filter}}$  and  $\varepsilon_{\text{trigger}}$  together represent the efficiency of RPVLL filter, the ratio of the events passing RPVLL filter to the total events processed. RPVLL filter has the trigger filter as one of its requirements. Because it is desirable to study the trigger efficiency independently from the filter efficiency, RPVLL filter efficiency is factorized into the filter efficiency and the trigger efficiency.  $\varepsilon_{\text{track}}$  represents the efficiency to reconstruct ID tracks from signal particles, and  $\varepsilon_{\text{lepton}}$  represents the efficiency to reconstruct and identify the signal particles as leptons using ID tracks, energy deposite in calorimeters, or MS tracks. Since  $\varepsilon_{\text{track}}$  and  $\varepsilon_{\text{lepton}}$  are different for  $e$  and  $\mu$ , two lepton are specified by the index 1 and 2.  $\varepsilon_{\text{vertex}}$  represents the efficiency to reconstruct a displaced vertex that pass the vertex selection using two signal leptons.

In order to understand the source of signal efficiency loss, the trigger efficiency is studied in Section 7.1, and the tracking and lepton identification efficiencies are studied in Section 7.2. In Section 7.3, the overall reconstruction efficiency, also referred as signal efficiency, of the  $Z'$  signal model after the full analysis selection is presented.

## 7.1 Trigger efficiency

The trigger efficiency is defined as the ratio of the events passing one of the triggers used in this analysis to the total events generated. In this analysis, three triggers listed on Table 6.1 are used to select the events with displaced dilepton vertex candidates. The single muon trigger is sensitive to the events with a  $\mu^+\mu^-$  or  $e^\pm\mu^\mp$  vertex. The di-photon trigger is mainly used to select the events with an  $e^+e^-$  vertex, but a small number of events with an  $e^\pm\mu^\mp$  vertex pass this trigger. The single photon trigger is sensitive to events with  $e^+e^-$  or  $e^\pm\mu^\mp$  vertex, but its efficiency is relatively low in comparison with the other two triggers.

To illustrate the impact of the trigger efficiencies on the signal samples, the efficiency of each trigger and the combined trigger efficiency is shown in Figure 7.1 using the signal MC samples of  $Z'$  decaying to all three channels at  $m = 250$  GeV and  $c\tau = 250$  mm. The sample with  $e^+e^-$  channel shows the highest combined trigger efficiency due to the high efficiency in di-photon trigger, and the sample with  $e^\pm\mu^\mp$  channel shows the reduced combined trigger efficiency because  $e^\pm\mu^\mp$  vertices have only one track that can satisfy either the single muon or photon trigger.

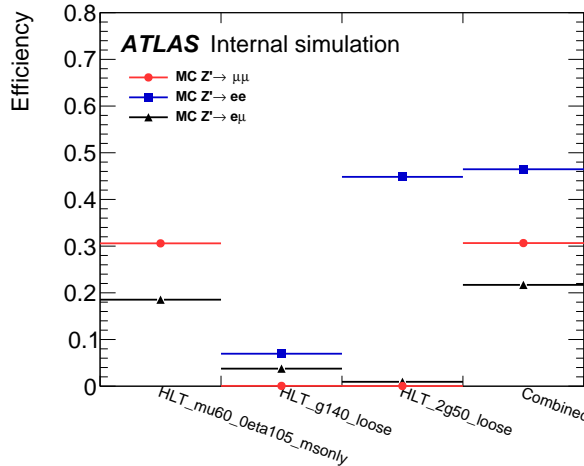


Figure 7.1: Trigger efficiency of single muon, single photon, di-photon, and the combined triggers of the signal MC samples of  $Z' \rightarrow \mu^+\mu^-$ ,  $e^+e^-$ , and  $e^\pm\mu^\mp$  generated with  $m = 250$  GeV and  $c\tau = 250$  mm.

The trigger efficiency of all  $Z'$  signal MC samples is shown in Appendix A. It is evident that at low  $Z'$  mass ( $\sim 100$  GeV), the combined trigger efficiency of the signal MC sample is significantly reduced because typical  $p_T$  of the signal leptons is lower than the  $p_T$  threshold

of the triggers.

The trigger study indicates that there is a substantial loss in the signal efficiency at trigger level before reconstruction, and developing dedicated, more efficient triggers for long-lived particles will provide potential improvement in sensitivity to long-lived particles.

### 7.1.1 Trigger Scale Factors

The performance of triggers may be different in data and MC simulations. Therefore, trigger scale factors are usually measured with tag-and-probe studies on  $Z + \text{jet}$  and applied to efficiency calculation, where most leptons have small impact parameters. However, because the leptons originating from displaced vertices tend to have large impact parameters, the standard scale factors on triggers provided by the performance groups cannot be applied. In the following, the scale factors on the lepton triggers are estimated using tag-and-probe method on the data and  $Z + \text{jets}$  MC samples.

The estimated scale factors are valid only if the trigger efficiencies do not depend on impact parameters or if this dependence is modelled reasonable well in simulations. Therefore, the efficiencies of the single photon and single muon triggers listed on Table 6.1 are estimated using the signal MC samples as a function of impact parameters  $d_0$  and  $z_0$  in Figure 7.2.

The plots show that the photon trigger efficiency is uniform up to  $|d_0| < 200$  mm and  $|d_0| < 300$  mm. The muon trigger efficiency starts to decrease for large impact parameters,  $|d_0| \sim 120$  mm and  $|z_0| \sim 200$  mm. However, the decreasing muon efficiency at very large impact parameters is neglected since the fraction of reconstructed muons with such large impact parameters is less than 10% at the lifetime of  $c\tau = 100$  mm.

### Photon triggers

The scale factors of the single photon and the di-photon triggers are estimated with a standard tag and probe method on  $Z \rightarrow ee$  events both in data and MC samples. The di-photon trigger (`HLT_2g50_loose`) is studied using the single photon trigger (`HLT_g50_loose`) with the same  $p_T$  threshold. The selection criteria of electron tag-and-probe candidates are listed in Table 7.1. In addition, pairs are required to have opposite signs and to satisfy the mass requirement ( $|m_{e^+e^-} - m_Z| < 10$  GeV) and the isolation requirement of  $\Delta R(\text{tag}, \text{probe}) > 0.4$ .

The invariant mass distributions of the tag-and-probe pairs found in the data and the MC samples are shown in Figure 7.3. It is evident that the background is negligible, and the shapes of distributions are in good agreement with data and MC. Therefore, no background

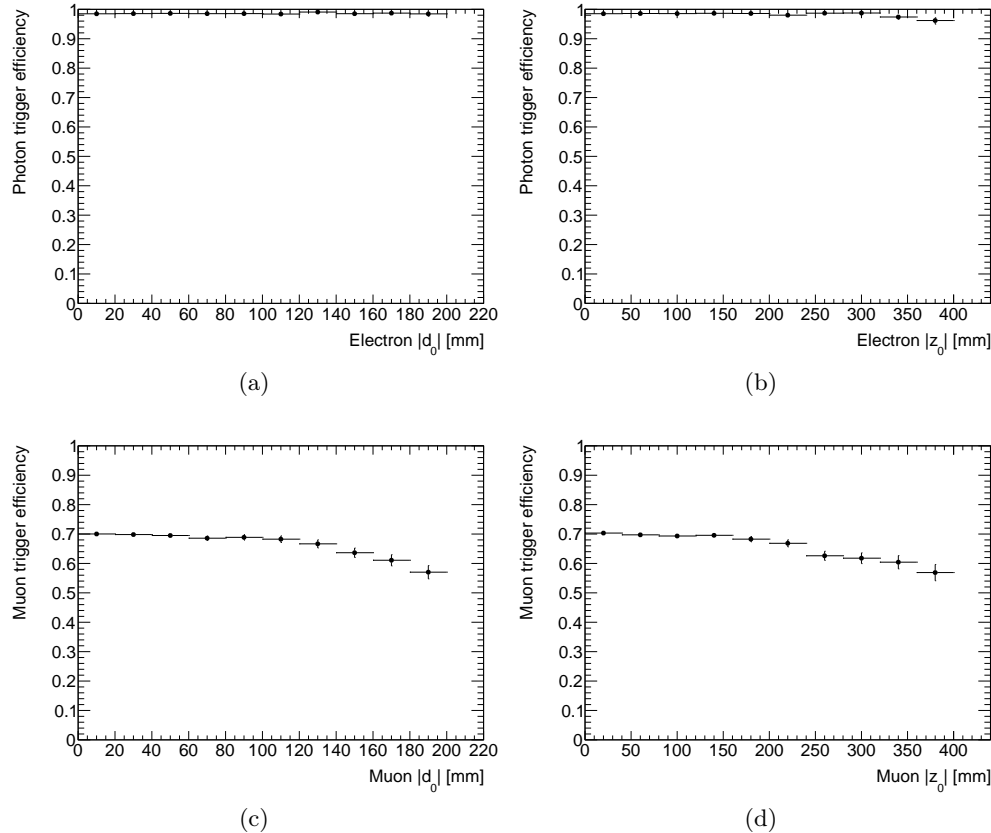


Figure 7.2: The efficiency of the single photon trigger for an electron as a function of (a)  $|d_0|$  and (b)  $|z_0|$ . The corresponding plots of the single muon trigger are shown in (c) and (d).

Selection	Tag	Probe
$p_T$ (GeV)	> 27	> 30
Trigger matched	HLT_e26_lhtight_nod0_ivarloose	-
$ \eta $	< 1.37 or 1.52 - 2.47	< 2.47
Identification	TightLH	LooseLHNoD0
Object quality	yes	yes
Track isolation	yes	-
Jet veto	-	yes

Table 7.1: Selection criteria for tag-and-probe electrons in  $Z+jets$  studies.

subtraction is performed in the calculation of the trigger efficiencies,

$$\epsilon_{\text{trigger}} = \frac{\text{Number of probes matched to trigger}}{\text{Number of probes}}. \quad (7.2)$$

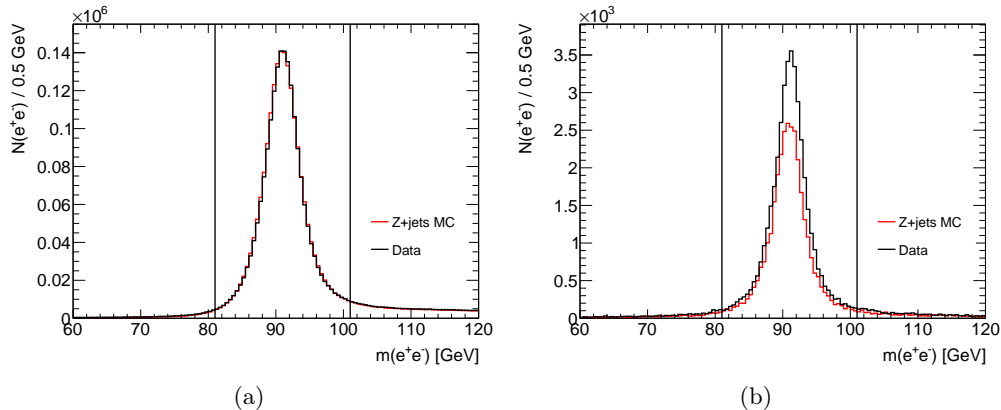


Figure 7.3: Invariant mass distributions of the tag-and-probe electron pairs used to study the efficiencies of the (a) `HLT_g50_loose` and (b) `HLT_g140_loose` trigger in the data and  $Z+jets$  MC samples. Only the pairs with a probe electron in the plateau region of Figure 7.4a and 7.4b are used in the tag-and-probe method.

The selected tag-and-probe electrons are used to estimate the efficiencies of photon triggers, shown as a function of probe  $p_T$ ,  $\eta$ , and  $|z_0|$  in Figure 7.4. The efficiency in  $p_T$  shows that the `HLT_g50_loose` plateau starts at 55 GeV, and `HLT_g140_loose` plateau starts at 148 GeV, and the electrons in this plateau region are used in the rest of Fig. 7.4. The efficiency in  $\eta$  shows good agreement between data and MC for electrons reconstructed inside

the barrel, whereas a small discrepancy in efficiency is shown for electrons at the boundary regions and in the end-cap regions. Also, the efficiency in  $|z_0|$  shows no dependence of the photon trigger efficiencies on  $|z_0|$ .

The ratio of the efficiency from data to MC, binned in  $\eta$ , is taken as a scale factor and applied to the efficiency calculation.

## Muon trigger

The scale factor of the single muon trigger is estimated with a standard tag-and-probe method on  $Z \rightarrow \mu\mu$  events both in data and MC. The selection criteria of muon tag-and-probe candidates are listed in Table 7.2. Similar to the photon triggers, pairs are required to have opposite signs and to satisfy the mass requirement ( $|m_{e^+e^-} - m_Z| < 10$  GeV) and the isolation requirement of  $\Delta R(\text{tag}, \text{probe}) > 0.4$ .

Selection	Tag	Probe
$p_T$ (GeV)	> 28	> 30
Trigger matched	HLT_mu26_ivarmedium	-
$ \eta $	< 2.4	< 1.05
Identification	Medium	Loose and combined
Isolation	Loose	-
$d_0$ significance	< 3	-
$\Delta z_0 \sin \theta$	< 0.5 mm	-

Table 7.2: Selection criteria for tag-and-probe muons.

The invariant mass distributions of the muon tag-and-probe pairs found in the data and the MC samples are shown in Figure 7.5. It is evident that the background is negligible and therefore not corrected for the calculation of the trigger efficiency.

The selected tag-and-probe muons are used to estimate the efficiency of the single muon trigger, shown as a function of probe  $p_T$  and  $|z_0|$  in Figure 7.6. The efficiency in  $p_T$  shows that the efficiency plateau starts at 62 GeV. The efficiency is uniform up to  $|z_0| \sim 150$  mm. In Figure 7.7, the muons in this plateau region ( $p_T > 62$ ) are used to compare the efficiency in data and MC. It is evident that efficiency depends on both  $\phi$  and  $\eta$ .

The ratio of the efficiency from data to MC, binned in  $\phi$  and  $\eta$ , is taken as a scale factor and applied to the efficiency calculation.

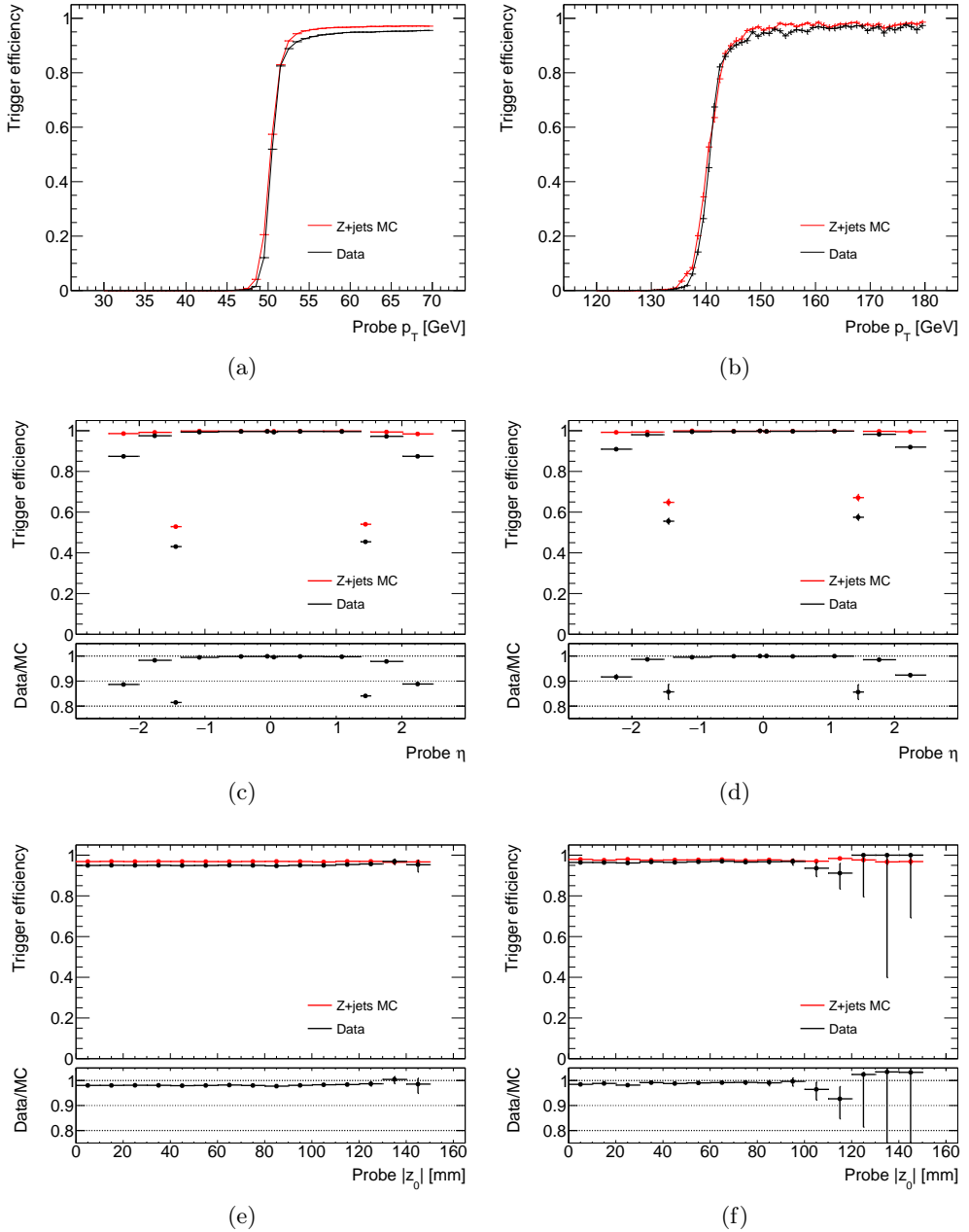


Figure 7.4: Efficiency of the HLT\_g50\_loose as a function of the (a)  $p_T$ , (c)  $\eta$ , and (e)  $|z_0|$  of the probe in the data and  $Z+jets$  MC samples. The corresponding plots of the HLT\_g140\_loose trigger are shown in (b), (d), and (f). Only the pairs with a probe electron in the plateau region of (a) and (b) are used in (c) - (f).

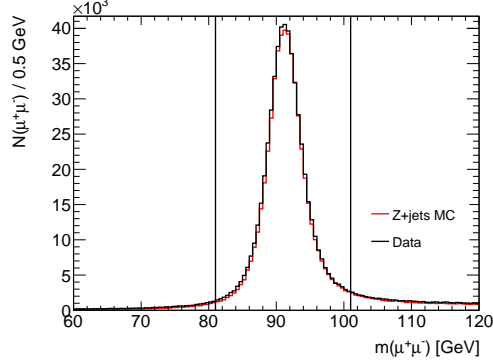


Figure 7.5: Invariant mass distributions of the tag-and-probe muon pairs used to study the efficiencies of the single muon trigger in the data and  $Z$ +jets MC samples. Only the pairs with a probe muon in the plateau region of Figure 7.6a are used in the tag-and-probe method.

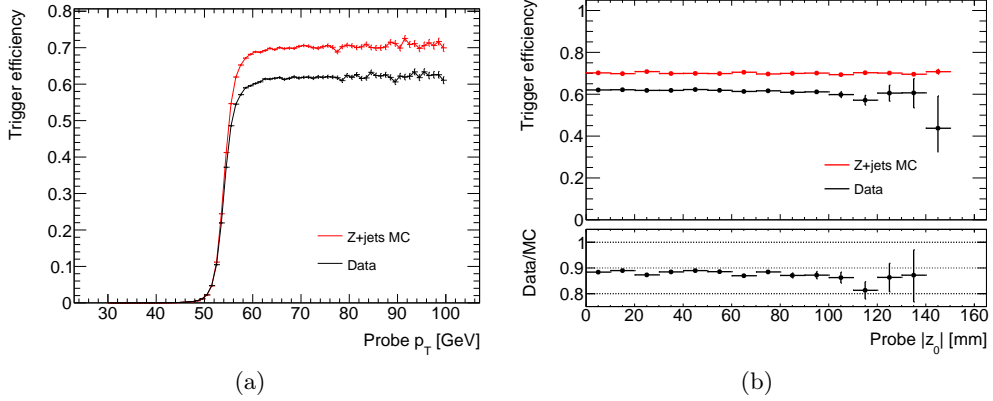


Figure 7.6: Efficiency of the single muon trigger as a function of the (a)  $p_T$  and (b)  $|z_0|$  of the probe in the data and  $Z$ +jets MC samples. Only the muons in the plateau region ( $p_T > 62$  GeV) of (a) are used in (b).

### 7.1.2 Summary on trigger study

The trigger studies show that the triggers have no dependence on the impact parameters up to  $d_0 \sim 120$  and  $z_0 \sim 200$  mm (Fig. 7.2). Using the tag-and-probe method, scale factors are obtained, and the total scale factors are summarized in Table 7.3.

These scale factors are binned in  $\eta$  for the photon triggers and are binned in both  $\eta$  and  $\phi$  for the muon trigger to correct signal efficiency. The overall trigger efficiency depends on the mass of  $Z'$ , 24-58% for  $\mu\mu$ , 38-93% for  $ee$ , and 17-88% for  $e\mu$  at  $m \geq 250$  GeV, and the trigger efficiency is much reduced for lower mass due to the  $p_T$  threshold of the triggers.

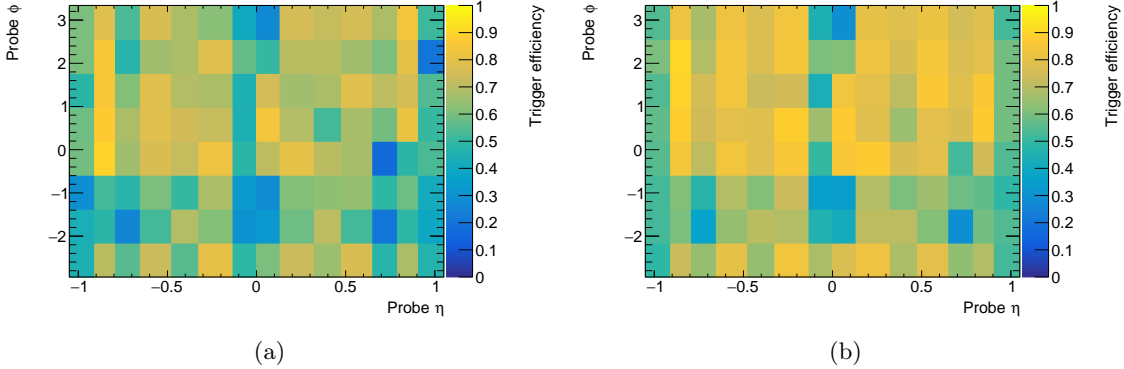


Figure 7.7: Efficiency of the single muon trigger as a function the  $\eta$  and  $\phi$  of the probe in (a) data and (b) Z+jets MC sample.

Trigger	Total scale factor
HLT_g140_loose	0.988
HLT_g50_loose	0.980
HLT_mu60_0eta105_msonly	0.884

Table 7.3: Total trigger scale factors from the tag-and-probe method.

## 7.2 Lepton reconstruction efficiency

The tracking efficiency,  $\varepsilon_{\text{track}}$ , and the lepton identification efficiency,  $\varepsilon_{\text{lepton}}$ , are studied together as a lepton reconstruction efficiency. The lepton reconstruction efficiency is defined and estimated as follows. From a signal MC sample, the leptons decaying from  $Z'$  are collected at generator-level, referred as *truth* signal leptons. For each truth signal lepton, if there is a reconstructed lepton with its ID track matched to the ID track of the truth signal lepton by a hit-based truth matching scheme, it is marked as reconstructed. The ratio of reconstructed signal leptons to the total number of signal leptons produced in the sample is taken as the lepton reconstruction efficiency. No RPVLL or trigger filter is applied in estimating the lepton reconstruction efficiency.

Figure 7.8 shows a representative plot of the lepton reconstruction efficiency as a function of track parameters using the combined signal MC samples of a  $Z'$  decaying to all three channels, generated with  $m = 250$  GeV and  $c\tau = 250$  mm.

It is evident that the efficiency decreases drastically at  $|\eta| > 2.0$  where the Pixel barrel region ends due to the minimum silicon hits requirement on tracks as shown in Table 3.1.

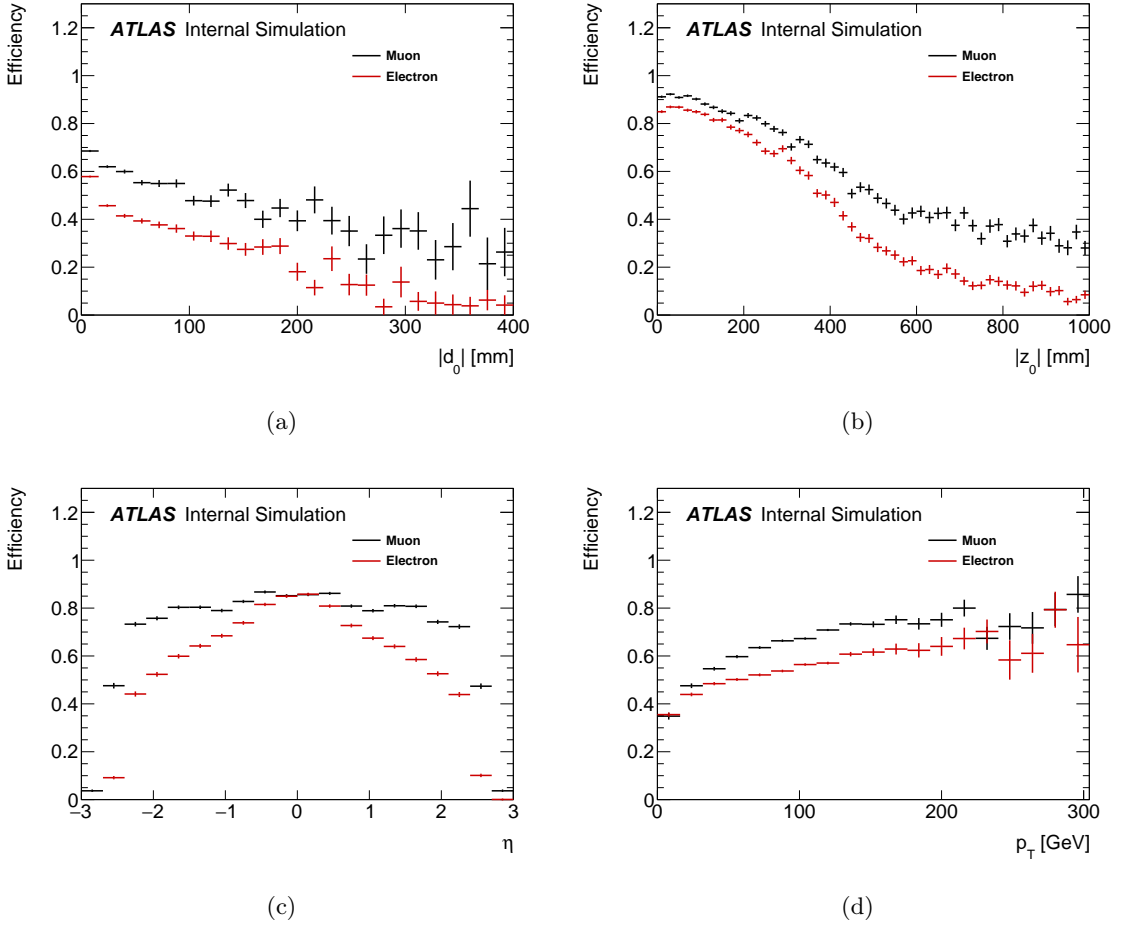


Figure 7.8: Lepton reconstruction efficiency as a function of (a)  $d_0$ , (b)  $z_0$ , (c)  $\eta$ , and (d)  $p_T$  of signal leptons for the  $Z'$  signal MC sample generated with  $m = 250$  GeV and  $c\tau = 250$  mm.

The efficiency is not very sensitive to  $p_T$  except in the low  $p_T$  region ( $p_T < 20$  GeV).

The lepton reconstruction efficiency decreases for large  $d_0$  and  $z_0$ . In the signal MC samples, most of the  $Z'$  decay within the Pixel barrel region,  $r < 122.5$  mm and  $|z| < 400.5$  mm, where the lepton reconstruction efficiency is high.

### 7.3 Overall reconstruction efficiency

The overall reconstruction efficiency represents the signal efficiency defined in Eq. 7.1, i.e. the ratio of  $Z'$ 's reconstructed as displaced vertices in the signal region to the total  $Z'$  produced in the sample. In this section, the signal selection cut flows (Section 7.3.1), the signal efficiency,

and the efficiency distributions (Section 7.3.2) are presented. In Section 7.3.3, efficiency maps of the signal samples are presented as a function of  $p_T$  and  $|\eta|$  of  $Z'$ .

### 7.3.1 Event and vertex cut flow

The signal MC samples are processed as described in Section 6.1, in which long-lived  $Z'$ 's are reconstructed as secondary vertices. The event and the vertex selections (Table 6.5) are applied to the processed samples, and representative plots of the event vertex cut flow are shown in Figure 7.9 using the signal MC samples of  $Z'$  decaying to  $\mu^+\mu^-$  generated with  $m = 250, 1000 for  $c\tau = 100.$$

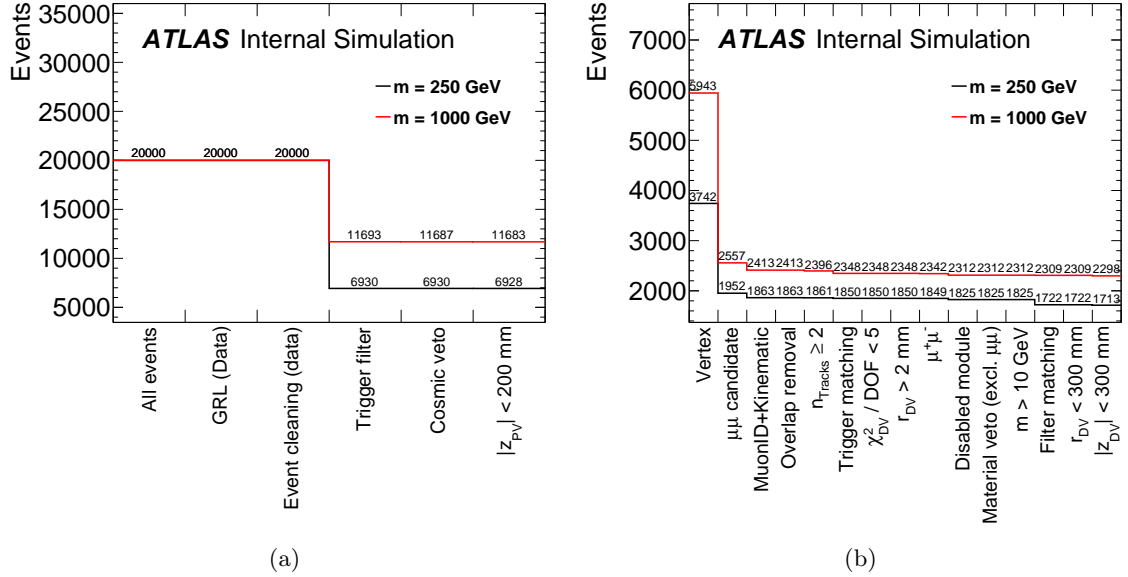


Figure 7.9: (a) Event cut flow, and (b) vertex cut flow using the signal MC samples of  $Z' \rightarrow \mu^+\mu^-$  generated with  $m = 500, 1000 for  $c\tau = 100.$$

In the event cut flow, `GoodRunsList` filter and Event cleaning are shown as place holders as they are only applied to data sample. About 34-60% of the signal events passed the event cut flow, but the vertex cut flow shows that only about 18-25% of the signal events have a displaced vertex candidate, indicating that there is a significant loss of signal efficiency in the vertex reconstruction process. The following selection criteria,  $\chi^2 / \text{DOF} < 5$  and the displacement cut ( $r_{\text{DV}} > 2$  mm), are applied, but the effect is very small as expected because the same requirements are applied in the secondary vertex reconstruction algorithm.

A material veto is applied to all vertex types except  $\mu^+\mu^-$  vertex. The minimum dilepton mass requirement has minimum impact on the signal efficiency.

Events and vertex cut flow of other signal samples are shown in Tables 7.4–7.6.

### 7.3.2 Signal efficiency and distribution

The signal efficiency is studied by examining the efficiency distributions in the transverse ( $r$ ), longitudinal ( $z$ ) vertex position, and the  $\eta$  and  $\phi$  distributions of the signal vertices. The representative efficiency distributions are shown in Figure 7.10 using the signal MC samples generated with  $m = 500, 1000$  GeV for  $c\tau = 100$  mm.

The signal efficiency shows a dependence on vertex position which decreases at large  $r$  and  $z$  due to the minimum silicon hits requirement on tracks. The first (central) bins in  $r$  ( $z$ ) distributions have lower efficiency due to the minimum displacement requirement ( $r_{DV} > 2$  mm) on secondary vertices. The  $\eta$  distribution has an uniform efficiency of  $\sim 25\%$  for  $|\eta| < 2.5$ . The  $\phi$  distribution is uniform as expected. The pile-up distribution of the signal efficiency shows that the efficiency is reduced for high pile-up as expected.

The overall signal efficiency for the signal samples are shown in Table 7.7. The signal efficiency is 14.9-33.3% for mass above 500 GeV, but the efficiency is reduced for lower  $Z'$  mass due to minimum  $p_T$  thresholds on the leptons, especially for the samples with  $m_{Z'} = 100$  GeV. The samples with shorter lifetime tend to have higher signal efficiency as expected.

### 7.3.3 Efficiency map

Signal efficiency for each mass and lifetime of long-lived  $Z'$  sample is presented as a function of  $p_T$  and  $|\eta|$  of  $Z'$ . Because any neutral, LLP decaying to a dilepton pair can be described by mass, lifetime,  $p_T$ , and  $\eta$  of the LLP, these efficiency maps can be used for other BSM searches such as searching for long-lived neutralino in the context of SUSY R-parity violating theory.

Representative efficiency maps are shown in Figure 7.11 using the signal MC samples of  $Z' \rightarrow \mu\mu, ee, e\mu$  with  $m = 500, 1000$  GeV and  $c\tau = 100$  mm. The overall signal efficiency is  $\sim 10\%$ , but the efficiencies in the central region ( $|\eta| < 2.5$ ) are much higher. Efficiency maps of other signal samples are available in Appendix B.

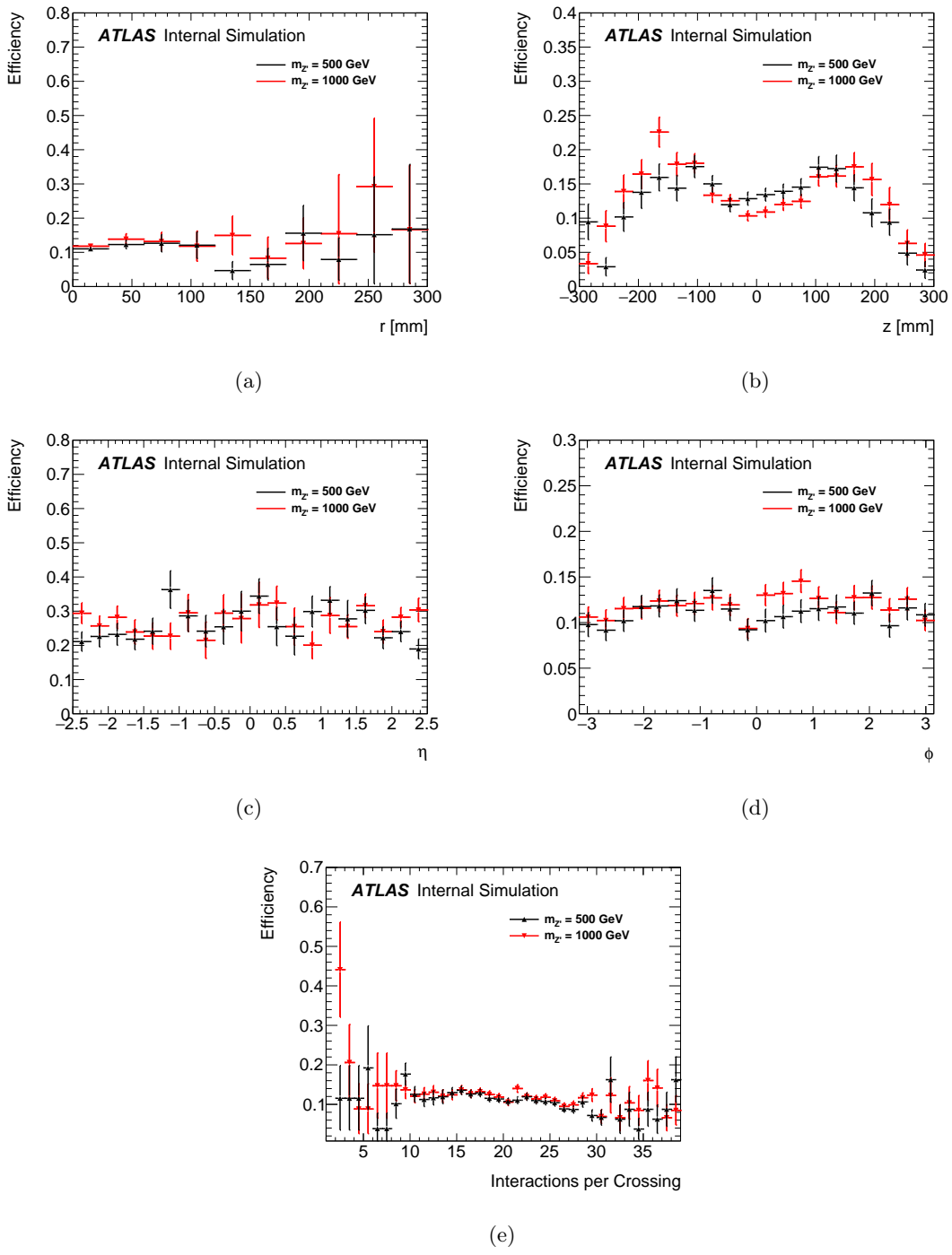


Figure 7.10: Signal efficiency as a function of (a)  $r$ , (b)  $z$ , (c)  $\eta$ , (d)  $\phi$ , and (e) pile-up for the signal MC samples of  $Z' \rightarrow \mu^+ \mu^-$  with  $m = 500, 1000 \text{ GeV}$  for  $c\tau = 100 \text{ mm}$ .

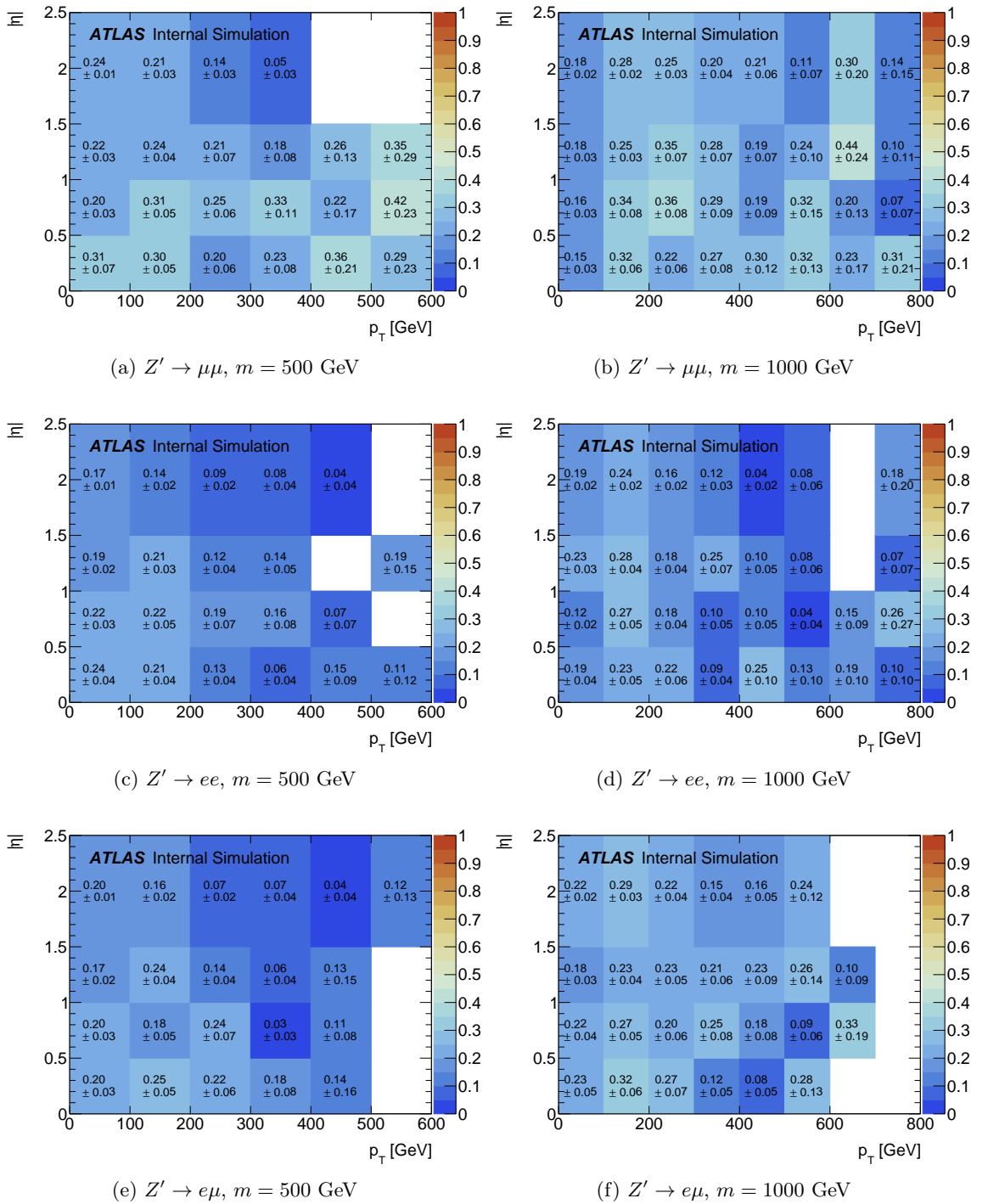


Figure 7.11: Signal efficiency maps of the signal MC sample of  $Z' \rightarrow \mu^+\mu^-$  with (a)  $m = 500$  and (b)  $m = 1000$  GeV for  $c\tau = 100$  mm. The corresponding efficiency maps for  $Z' \rightarrow e^+e^-$ ,  $e^\pm\mu^\mp$  is shown in (c)–(f).

$m_{Z'}$ (GeV)	$c\tau$ (mm)	All Events	Higgs pair	Cosmic veto	Vertex	Photon selection	Overlap removal	Trigger matching	Discriminating	Disabled module	Filter matching	300 mm	2DV/ $\sqrt{s}$						
100	100	20000	940	940	644	366	342	342	339	339	330	108	106	108	82	82	81	49	
100	250	20000	818	818	533	269	260	260	259	259	252	82	82	82	50	50	50	49	
100	500	20000	761	761	416	165	154	154	154	154	148	148	148	148	148	148	148	148	
250	100	20000	6930	6930	3742	1952	1863	1863	1861	1861	1850	1849	1825	1825	1825	1825	1825	1825	1713
250	250	20000	6180	6179	3467	1809	1708	1708	1703	1703	1700	1700	1699	1699	1699	1699	1699	1699	1722
250	500	20000	4922	4921	2680	1354	1284	1284	1278	1278	1276	1276	1276	1276	1276	1276	1276	1276	1582
500	100	19000	9146	9145	9144	4680	2205	2091	2091	2085	2068	2068	2068	2068	2068	2068	2068	2068	1176
500	250	20000	8273	8272	8269	4481	2191	2080	2080	2068	2056	2056	2056	2056	2056	2056	2056	2056	2056
500	500	20000	6724	6720	6717	3605	1777	1666	1666	1658	1646	1646	1646	1646	1646	1646	1646	1646	1572
750	100	20000	11032	11028	11027	5605	2473	2330	2330	2313	2282	2282	2282	2282	2282	2282	2282	2282	2254
750	250	20000	9622	9613	5301	2626	2457	2457	2441	2441	2421	2421	2421	2421	2421	2421	2421	2421	2250
750	500	20000	8059	8055	8054	4262	2017	1878	1878	1868	1851	1851	1851	1851	1851	1851	1851	1851	2364
1000	100	20000	11633	11683	11683	5943	2557	2413	2413	2396	2348	2348	2348	2348	2348	2348	2348	2348	1784
1000	250	20000	10517	10515	10514	5804	2725	2578	2578	2564	2518	2518	2518	2518	2518	2518	2518	2518	2457
1000	500	20000	8905	8902	8901	4878	2295	2170	2170	2155	2129	2129	2129	2129	2129	2129	2129	2129	2058

Table 7.4: Event and vertex cut flow of the signal MC sample of  $Z' \rightarrow \mu^+ \mu^-$ .

$m_Z$ (GeV)	$\sigma$ (mm)	All Events	Thinner Filter	Cosmic Veto	Electron Selection	Bad Cluster	Overlap Removal	Thinner matching	$\chi^2/\text{Dof}$	Detailed module	Filter matching	$m < 10$ GeV	$\tau_{\text{DV}} < 300$ mm	$\tau_{\text{DV}} > 300$ mm	$\tau_{\text{DV}} < 300$ mm	$\tau_{\text{DV}} > 300$ mm	$\tau_{\text{DV}} < 300$ mm	$\tau_{\text{DV}} > 300$ mm
100	100	20000	315	315	69	69	66	66	65	52	16	15	15	15	15	15	15	15
100	250	20000	323	323	145	59	58	56	56	36	15	15	15	15	15	15	15	15
100	500	20000	241	241	111	31	30	29	29	27	26	19	19	10	10	10	10	9
250	100	20000	10144	4472	1696	1658	1639	1618	1601	1585	1577	1563	1378	1345	1339	1339	1339	1339
250	250	20000	9276	9274	9272	1519	1501	1477	1458	1453	1453	1448	1206	1174	1174	1174	1174	1163
250	500	20000	7750	7749	3203	1105	1063	1038	1011	1011	1007	803	769	769	769	769	769	758
500	100	20000	16008	16006	6621	1917	1940	1925	1900	1878	1877	1843	1668	1656	1656	1656	1656	1652
500	250	20000	14853	14849	6245	1986	1907	1892	1880	1858	1858	1858	1580	1569	1569	1569	1569	1559
500	500	19000	12279	12278	5029	1566	1505	1502	1493	1471	1466	1455	1322	1194	1194	1194	1194	1162
750	100	20000	18014	18011	18006	2266	2196	2173	2138	2138	2138	2138	2092	2085	2085	2085	2085	1913
750	250	20000	16912	16914	16912	2260	2186	2177	2168	2129	2129	2129	2099	2081	2081	2081	2081	1808
750	500	20000	15290	15286	6206	1853	1791	1778	1731	1731	1731	1731	1423	1423	1423	1423	1423	1399
1000	100	20000	18723	18719	18714	2347	2271	2247	2195	2195	2195	2195	2151	2004	2004	2004	2004	1992
1000	250	20000	17890	17883	17877	2487	2412	2395	2349	2349	2349	2349	2298	2070	2070	2070	2070	2050
1000	500	19000	15666	15660	15658	1956	1881	1870	1866	1842	1842	1842	1812	1562	1562	1562	1562	1559

Table 7.5: Event and vertex cut flow of the signal MC sample of  $Z' \rightarrow e^+e^-$ .

$m_{Z'}$ (GeV)	$c\tau$ (mm)	All events	Trigger filter	Cosine Veto	Electron Selection	Bad Chamber	Overlap Removal	Trigger matching	Disabled module	Filter matching	$\Delta DV/\Delta 300 \text{ mm}$
100	100	19000	484	484	295	150	145	137	134	134	88
100	250	20000	483	483	255	94	91	89	88	61	21
100	500	19000	379	379	178	56	53	53	53	34	15
100	100	20000	4771	4769	2326	960	938	899	891	868	851
250	250	20000	4273	4272	2251	921	901	899	874	848	844
250	500	20000	3486	3484	1667	709	695	693	678	663	663
500	100	19000	13351	13346	6049	2168	2135	2131	2040	2005	2005
500	250	20000	12680	12680	12679	5736	2199	2169	2059	2037	2020
500	500	20000	10885	10883	10883	1697	1697	1689	1604	1595	1594
750	100	19000	16046	16036	16032	7041	2624	2582	2480	2437	2437
750	250	20000	15546	15545	15541	7171	2706	2659	2533	2494	2493
750	500	20000	13598	13590	13585	6033	2170	2132	2025	2003	1995
1000	100	18000	15970	15963	15959	7189	2581	2535	2415	2385	2371
1000	250	20000	16751	16743	16739	7855	3088	3036	3028	2899	2854
1000	500	19000	14165	14154	6366	2345	2290	2284	2198	2162	2153

Table 7.6: Event and vertex cut flow of the signal MC sample of  $Z' \rightarrow e^\pm \mu^\mp$ .

$m_{Z'}$ (GeV)	$c\tau$ (mm)	$\mu\mu$ (%)	$ee$ (%)	$e\mu$ (%)
100	100	$0.46 \pm 0.05$	$0.07 \pm 0.02$	$0.10 \pm 0.02$
100	250	$0.35 \pm 0.04$	$0.07 \pm 0.02$	$0.08 \pm 0.02$
100	500	$0.20 \pm 0.03$	$0.05 \pm 0.02$	$0.07 \pm 0.02$
250	100	$7.70 \pm 0.19$	$6.44 \pm 0.17$	$3.10 \pm 0.12$
250	250	$7.12 \pm 0.18$	$5.59 \pm 0.16$	$2.81 \pm 0.12$
250	500	$5.25 \pm 0.16$	$3.59 \pm 0.13$	$2.19 \pm 0.10$
500	100	$9.67 \pm 0.21$	$8.16 \pm 0.19$	$8.97 \pm 0.21$
500	250	$9.02 \pm 0.20$	$7.62 \pm 0.19$	$8.25 \pm 0.19$
500	500	$7.00 \pm 0.18$	$5.96 \pm 0.17$	$6.01 \pm 0.17$
750	100	$10.23 \pm 0.21$	$9.48 \pm 0.21$	$11.45 \pm 0.23$
750	250	$10.65 \pm 0.22$	$8.94 \pm 0.20$	$10.47 \pm 0.22$
750	500	$7.91 \pm 0.19$	$6.84 \pm 0.18$	$7.89 \pm 0.19$
1000	100	$10.43 \pm 0.22$	$9.89 \pm 0.21$	$11.86 \pm 0.24$
1000	250	$11.11 \pm 0.22$	$10.15 \pm 0.21$	$12.21 \pm 0.23$
1000	500	$9.26 \pm 0.20$	$7.97 \pm 0.20$	$9.17 \pm 0.21$

Table 7.7: Overall signal efficiency of the signal samples. Statistical uncertainties are shown.

# Chapter 8

## BACKGROUND ESTIMATION

Due to the lifetime ( $c\tau > 2$  mm) and mass ( $m > 10$  GeV) requirements applied at vertex selection, no SM background is expected in the signal region in the search for a displaced dilepton resonance. Therefore, two non-collision backgrounds are considered in this search: cosmic background and *random-crossing* background. The cosmic background is the dominant background in this analysis and is estimated in Section 8.1. In Section 8.2, the background from the random-crossing of two uncorrelated tracks is estimated.

### 8.1 Cosmic Background

A cosmic muon passing through the ID during a collision event can be reconstructed as a back-to-back muon pair with opposite electric charges, forming a displaced  $\mu^+\mu^-$  vertex.

This cosmic background is suppressed by implementing the cosmic veto,  $R_{\text{CR}} < 0.01$  (Section 6.1.1). The event cut flow in Figure 7.9a shows that the cosmic veto is very effective with negligible signal loss. To illustrate the effectiveness of the veto, a cosmic control region is defined as follows:

- Events are required to fail the cosmic veto.
- Events are required to have at least two muons satisfying vertex track selection (Table 3.3).
- All other event selections are kept the same as the signal region.

In this control region, pairs of two muons with highest  $p_T$  are studied using the data sample. Figure 8.1 shows the distribution of the pairs in  $|\Delta\phi|$  and  $\eta_1 + \eta_2$ . The distribution

shows that a significant fraction of muons pairs is from cosmic rays and is constrained to the small  $R_{\text{CR}}$  region.

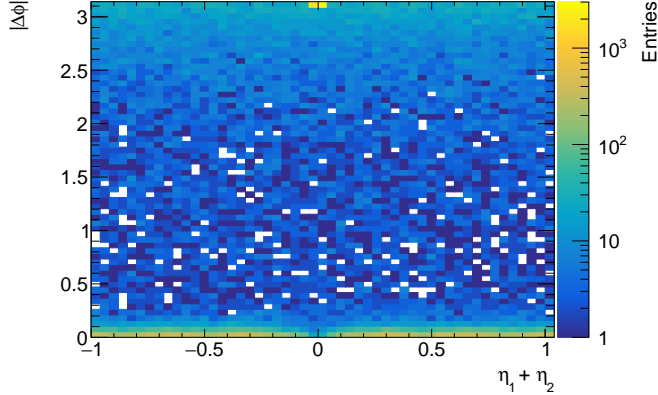


Figure 8.1: Distribution of pairs of two muons with highest  $p_T$  in  $|\Delta\phi|$  and  $\eta_1 + \eta_2$  found in the cosmic control region using the data sample. The sharp peak at  $|\Delta\phi| = \pi$  and  $\Sigma\eta = 0$  shows that a significant fraction of muon pairs in the region is from cosmic muons. The empty bins are shown with white.

To estimate the cosmic background in the signal region, the  $R_{\text{CR}}$  distribution of  $\mu^+\mu^-$  pairs is compared to those forming a vertex in Figure 8.2b. There are 246  $\mu^+\mu^-$  vertices found in the data sample that pass all of the signal selection except the cosmic veto, and there is no event with  $R_{\text{CR}} > 0.004$ , indicating that the cosmic background is effectively suppressed by the cosmic veto of  $R_{\text{CR}} = 0.01$ .

The  $R_{\text{CR}}$  distribution, normalized to  $\mu^+\mu^-$  pairs forming a vertex, yields a cosmic background of  $0.27 \pm 0.14$  (stat.). This background is about two orders of magnitude larger than the random-crossing background to be discussed. Therefore, the cosmic muon background is the dominant source of background in the signal region.

## 8.2 Random-Crossing Background

The random-crossing of two uncorrelated tracks can be a major source of the background in the search for displaced dilepton vertices. This background is expected to increase with more pile up in Run 2.

This random-crossing background is estimated by a data-driven method called the *track*

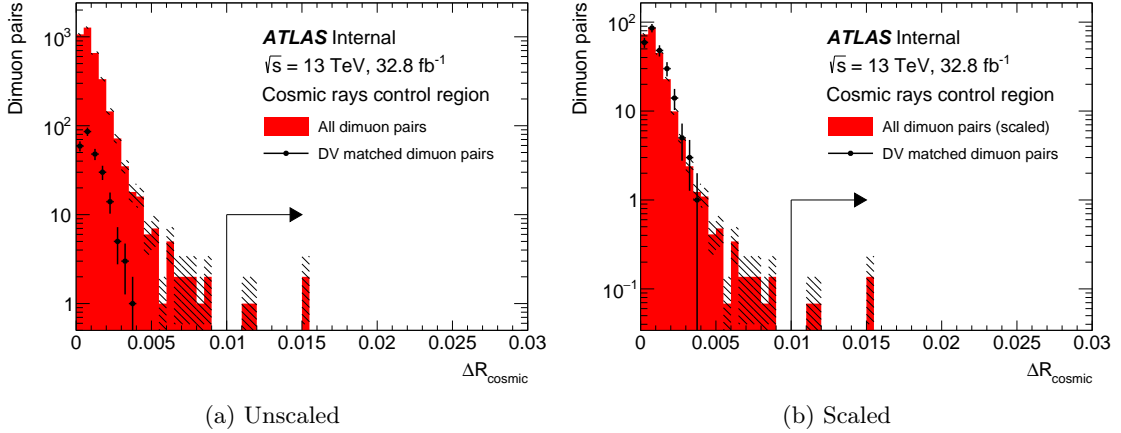


Figure 8.2: Comparison of the  $R_{\text{CR}}$  distribution of  $\mu^+\mu^-$  pairs with (dots) and without (shaded) the vertex requirement. The same distribution is shown in (b) normalized to the number of  $\mu^+\mu^-$  pairs forming a vertex.

*flipping* (TF). In this method, secondary vertex reconstruction is performed on each pair of tracks from all possible combinations of tracks after one random track from each pair is flipped with respect to the beam spot. Because one track is flipped in each pair of tracks, the resulting vertices provide a good estimate for random-crossing background. In addition, another random-crossing background method, called *event mixing*, is used to estimate systematic uncertainty in the background estimate.

The TF and event mixing methods are described in Section 8.2.1 and 8.2.2, respectively. In Section 8.2.3, the TF method is tested on the background MC samples, and the result is compared with the corresponding result from the event mixing. In Section 8.2.4, the random-crossing background in data is estimated by the TF method.

### 8.2.1 Track Flipping Method

In the TF method, events are selected by the same requirement described in Section 6.1. From the selected events, ID tracks associated with a muon, electron, or neither, referred as muon, electron, or non-leptonic track, respectively, are selected with the track criteria (Table 3.3) used for the secondary vertexing algorithm. Lepton tracks are required to pass the same selection criteria described in Table 6.3. Non-leptonic tracks are required to pass the same kinematic selection ( $p_T > 10$  GeV,  $|\eta| < 2.5$ ) as leptons.

From the selected tracks, track pairs are created from all possible combinations of muon, electron, or non-leptonic tracks, i.e.  $\mu^+\mu^-$ ,  $e^+e^-$ ,  $e^\pm\mu^\mp$ ,  $e^\pm x^\mp$ ,  $\mu^\pm x^\mp$ , or  $x^+x^-$ , where  $x$

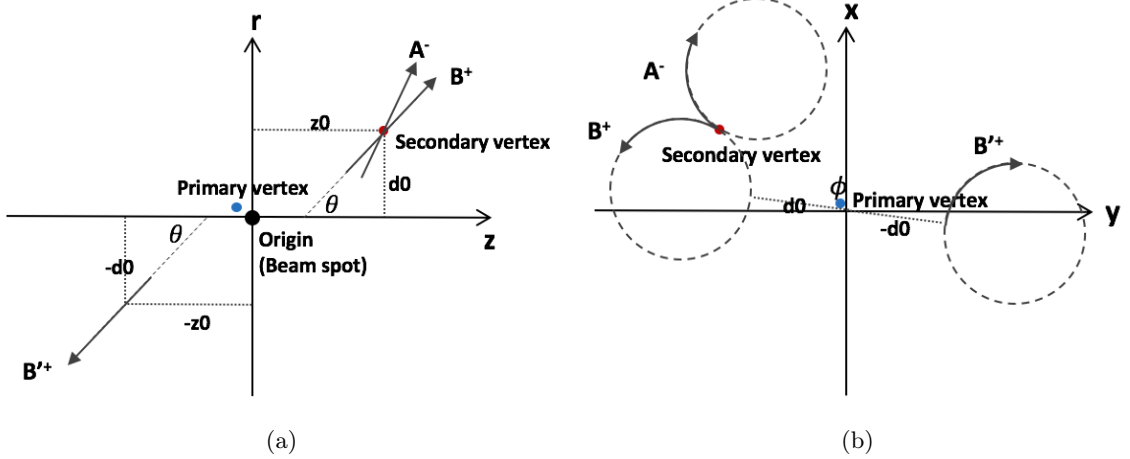


Figure 8.3: Description of track flipping method in (a)  $r - z$  and (b)  $x - y$  plane. Given two tracks  $A$  and  $B$  originating from a common secondary vertex, one random track is flipped with respect to the beam spot and is denoted as  $B'$ . The resulting flipped track pair,  $AB'$ , cannot form a vertex due to the separation in space.

represents a non-leptonic track. For each pair of tracks, one random track is flipped with respect to the beam spot ( $d_0 \rightarrow -d_0, z_0 \rightarrow -z_0, \phi \rightarrow \phi + \pi, \theta \rightarrow \pi - \theta$ ), creating a *flipped track pair*. The secondary vertex algorithm used in the reconstruction of data or MC sample is used to reconstruct displaced vertices using these flipped track pairs. Vertex selection cuts similar to the cuts listed in Table 3.3 are applied to the vertices found from flipped track pairs, except that the trigger matching and filter matching are only required for  $\mu\mu$ ,  $ee$ , and  $e\mu$ .

Track-flipped vertices are formed purely from random-crossing of tracks as depicted in Figure 8.3. Therefore, track-flipped vertex yields provide a good estimate for the random-crossing background. Also, because trigger and filter matchings are not imposed in the control and validation region, the TF method provides a conservative background estimation.

### 8.2.2 Event Mixing Method

The event mixing method is similar to the TF, but instead of flipping a track from a pair of tracks, it combines tracks from different events to create uncorrelated track pairs, i.e. two tracks do not originate from a real vertex.

The event mixing method proceed as follows. First, muon, electron, and non-leptonic tracks that satisfy the track criteria (Table 3.3) are collected from all events, resulting in a

collection of all potential seed objects in the sample. Lepton tracks are required to pass the same selection criteria<sup>4</sup> described in Table 6.3. Non-leptonic tracks are required to pass the minimal kinematic selection ( $p_T > 10$  GeV,  $|\eta| < 2.5$  to match with the kinematic selection for leptons.

Pairs of tracks are randomly sampled from the collection. For each track pair, a primary vertex is randomly chosen from all events with a lepton candidate. Primary vertices are needed in order to evaluate the displacement cut and quality requirements of the vertexing algorithm. The secondary vertex reconstruction is performed on each track pair.

The ratio of event-mixing vertex yields to the number of track pairs sampled represents the probability,  $p_{\text{xing}}$ , of two tracks randomly forming a displaced vertex. Using  $p_{\text{xing}}$  and the total number of track pairs of each type ( $\mu^+\mu^-$ ,  $e^+e^-$ ,  $e^\pm\mu^\mp$ ,  $\mu^\pm x^\mp$ ,  $e^\pm x^\mp$ ,  $x^+x^-$ ) in data, the random-crossing background is estimated for each type by, e.g.,

$$N_{\mu^+\mu^-}^v = N_{\mu^+\mu^-} \times p_{\text{xing}}, \quad (8.1)$$

where  $N_{\mu^+\mu^-}^v$  represent the estimated random-crossing background of  $\mu^+\mu^-$  type, and  $N_{\mu^+\mu^-}$  represents the total number of  $\mu^+\mu^-$  pairs present in data. The random-crossing probability,  $p_{\text{xing}}$ , is estimated individually for each type of vertices. The details on this method can be found in Ref. [61].

### 8.2.3 MC Study

The track-flipping and event mixing methods are compared using the background MC samples (Table 5.4). Similar event, track, and vertex selections are applied as the signal selection, but the track  $p_T$  requirement is lowered to  $p_T > 5$  GeV and opposite charge requirement is removed for more statistics. A representative plot of vertex cut flows in the TF method is shown in Figure 8.4 using track-flipped  $x^+x^-$  vertices from the background MC samples.

The vertex yields from the TF and event mixing method, which represent the estimation for random-crossing background, are compared with the vertex yields from reconstruction in Table 8.1. No random-crossing background of  $\mu^+\mu^-$ ,  $e^+e^-$ , or  $e^\pm\mu^\mp$  type is expected from the MC samples using both methods.

The vertex yields from the TF and the event mixing methods agree within the statistical uncertainty. The kinematic distributions of  $xx$  vertices in TF and event mixing are compared with those of the background MC samples in Figure 8.5. Both samples reproduce the vertex

<sup>4</sup>Only lepton pairs with an invariant mass greater than 6 GeV are used in the normalization procedure to remove any contamination from low mass processes.

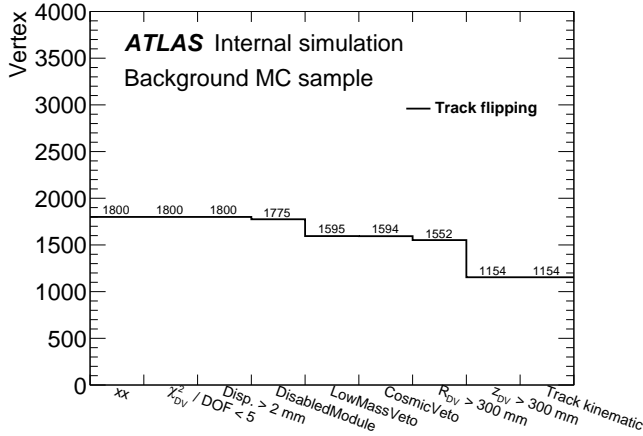


Figure 8.4: Vertex cut flow applied on  $x^+x^-$  vertices from the TF method.

Vertex Type	Track flipping	Event Mixing	MC
$\mu x$	3	4	5
$e x$	5	2	4
$xx$	1154	1125	989

Table 8.1: Comparison of the estimated vertex yields from the TF and event mixing with those reconstructed in the background MC samples.

distribution in the background MC samples.

#### 8.2.4 Estimating Random-crossing Background with Data Sample

The random-crossing background is estimated by performing the TF method on the data sample. Following the procedure described in Section 8.2.1, track-flipped vertices are created, and the vertex yields in the control and validation regions can be used to estimate the random-crossing background in the signal region.

In the control region, the  $xx$  vertices found from the track flipping method are compared to the vertices reconstructed in the data sample in Figure 8.6. The distributions shows that the TF method reproduces the data reasonably well including some of the structures of the ID, suggesting that the TF method provides a reasonable estimation of the random-crossing background.

Because of the limited number of lepton pairs in the data sample, it is not practical to

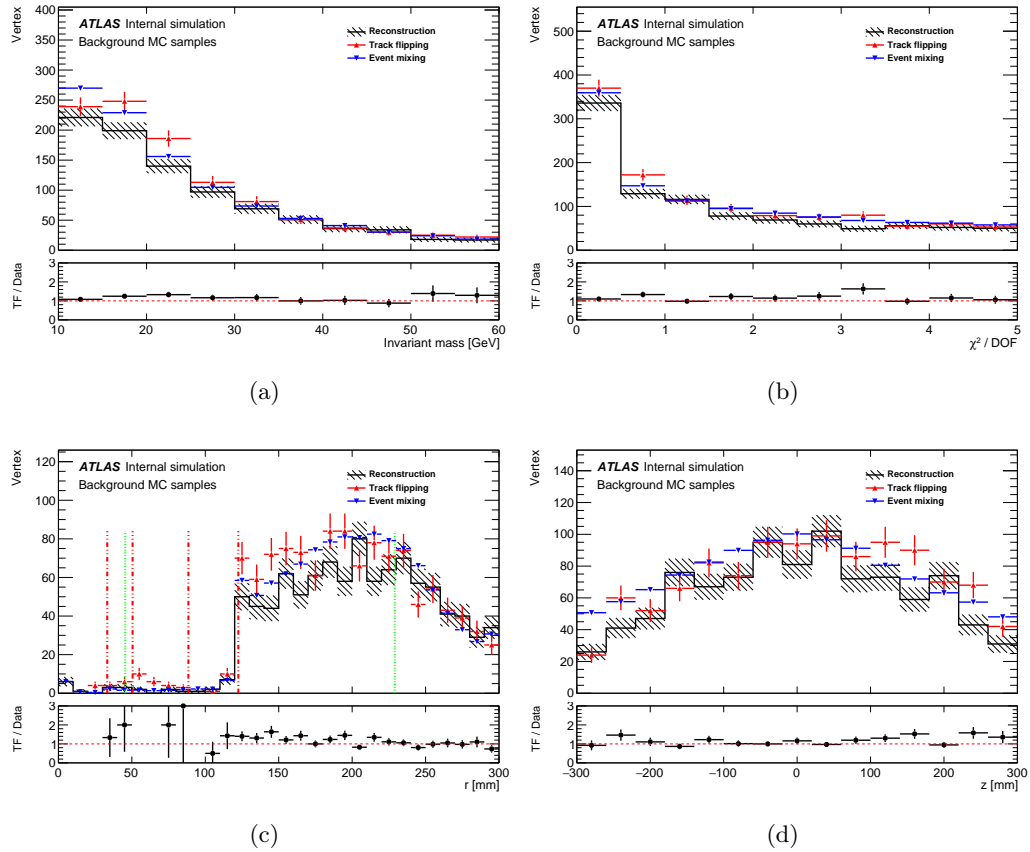


Figure 8.5: Comparison of (a) vertex mass, (b)  $\chi^2/\text{DOF}$ , (c) transverse, and (d) longitudinal position of  $x^+x^-$  vertices reconstructed in TF and event mixing with those reconstructed in the background MC samples. In (c), the red dashed lines indicate the four Pixel layers. The green dotted lines indicate the Inner Support Tube (45.5 mm) and Pixel Support Tube (229 mm).

use the TF method to estimate the random-crossing background. Instead, the track-flipped vertex yields in the control region and validation region (region with zero or one lepton) are used to estimate random-crossing background in the signal region using the lepton probability, defined as follows:

- $P(e)$  is defined as the ratio of number of electrons to number of inner detector tracks in the entire sample,
- $P(\mu)$  is defined as the ratio of number muons to number of inner detector tracks in the entire sample,

where track requirements described in Table 3.3 are imposed on both leptons and inner

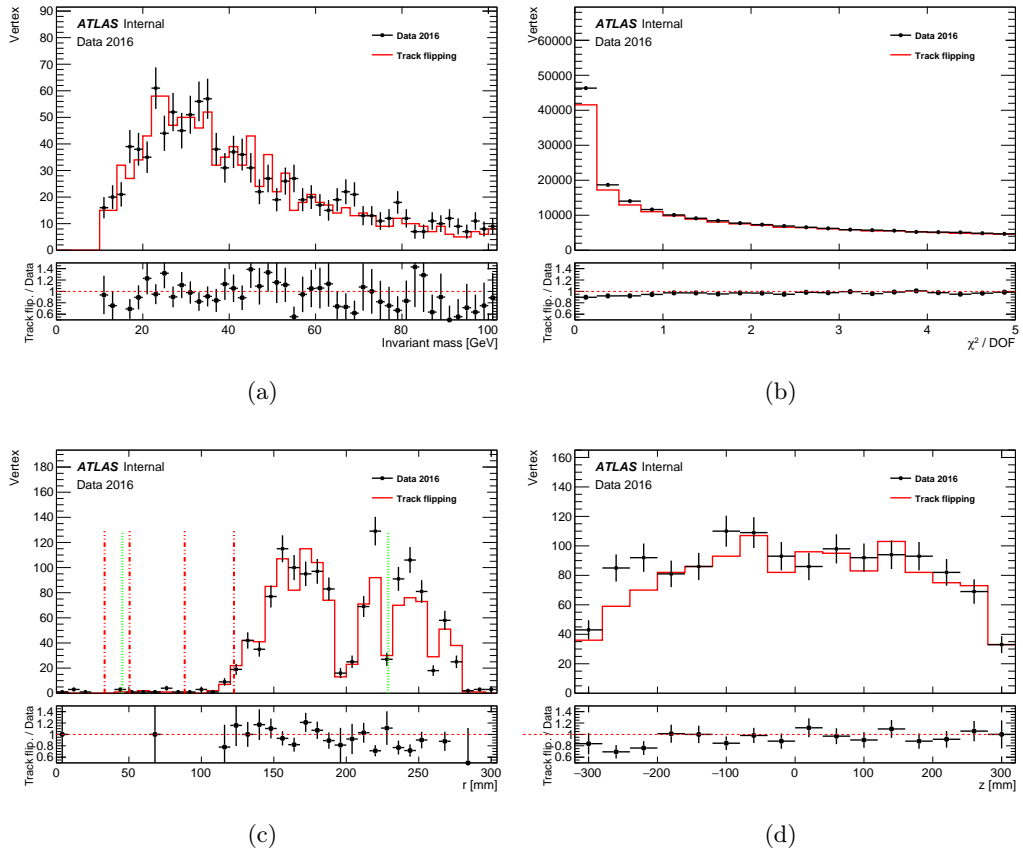


Figure 8.6: Comparison of (a) vertex mass, (b)  $\chi^2/\text{DOF}$ , (c) transverse, and (d) longitudinal position of vertices found in data with vertices formed in track flipping in the control region. In (c), the red dashed lines indicate the four Pixel layers. The green dotted lines indicate the Inner Support Tube (45.5 mm) and Pixel Support Tube (229 mm).

detector tracks. The lepton probability estimated from data is shown in Table 8.2.

	Tracks	$P(\ell)$
x	$2.47 \times 10^7$	-
$\mu$	$5.23 \times 10^4$	$2.10 \times 10^{-3}$
e	$3.63 \times 10^4$	$1.46 \times 10^{-3}$
Inclusive	$2.48 \times 10^7$	-

Table 8.2: Number of  $x$ ,  $\mu$ ,  $e$  tracks and the calculated lepton probability from data.

Using the lepton probabilities, the track-flipping vertex yield in the control region (xx) is

extrapolated into the validation region using Eq. D.9, and the extrapolated  $\mu x$  and  $ex$  vertex yields are compared with the observed track-flipping vertex yield to determine scale factors as defined in Eq D.10.

The track-flipping vertex yields in the control and validation regions are then extrapolated into the signal region using Eqs. D.7–D.9 to the estimate random-crossing background, and the scale factors (Eq. D.11) are applied to these extrapolation for a more precise estimate of the background.

The raw vertex yields in the TF method and data, and the scale factors calculated from the vertex yields are presented in Appendix D.7. The final estimate of random-crossing background from the TF method are shown in Table 8.3. The estimate of the background after applying the scale factors in the signal region is  $3.95 \times 10^{-3}$ , which is compatible with the corresponding result of  $2.40 \times 10^{-3}$  from the event mixing method [61].

	Raw estimate from xx	Raw estimate from $\mu x, ex$	Corrected estimate
$N_{\mu\mu}$	$2.69 \times 10^{-3}$	$2.19 \times 10^{-3}$	$1.79 \times 10^{-3}$
$N_{ee}$	$5.56 \times 10^{-3}$	$1.05 \times 10^{-3}$	$1.99 \times 10^{-4}$
$N_{e\mu}$	$7.73 \times 10^{-3}$	$3.89 \times 10^{-3}$	$1.96 \times 10^{-3}$
Sum of signal regions	$1.60 \times 10^{-2}$	$7.13 \times 10^{-3}$	$3.95 \times 10^{-3}$

Table 8.3: The estimate of random-crossing background in the signal region. Scale factors (Table D.4) are applied to obtain the corrected estimate of the background.

# Chapter 9

## SYSTEMATIC UNCERTAINTIES

The systematic uncertainties in the signal efficiency is computed by estimating the contribution of each efficiency factor in Eq. 7.1.

The systematic uncertainty in track and vertex reconstruction is studied using  $K_S$  in Section 9.1. The systematic uncertainty in trigger is studied in Section 7.1.1 using tag-and-probe method with  $Z \rightarrow e^+e^-,\mu^+\mu^-$  events.

### 9.1 Systematic Uncertainty in Track and Vertex Reconstruction

In a typical analysis, the systematic uncertainty in track and vertex reconstruction is estimated by the Inner Tracking Combined Performance group using the standard tracking setup. This result cannot be directly used for this analysis due to the special reconstruction setup described in Chapter 3. Instead, the systematic uncertainty in track and vertex reconstruction is estimated by comparing vertex yields between the data and the MC samples using the process,  $K_S \rightarrow \pi^+\pi^-$ . This process allows the comparison of the efficiencies between data and MC samples to the long lifetime ( $c\tau \sim 26.8$  mm). However, there are intrinsic differences between  $K_S$  and signal long-lived particles such as mass and  $p_T$ . In order to understand the validity and the limitation of this method, the kinematic distributions of  $K_S$  and  $Z'$  candidates are compared in Appendix C.

Tracks originating from a  $K_S$  decay can be reconstructed by either the standard tracking (ST) or the LRT algorithm, resulting in three categories of  $K_S$  vertices: vertices with two *standard tracks*, one standard track and one *large-radius track*, and two large-radius tracks.  $K_S$  vertex yields in each category can be expressed by total  $K_S$  produced in a sample and

tracking and vertexing efficiency,

$$\begin{aligned} N_{\text{ST}} &= K_S \text{ produced} \times (\epsilon_{\text{ST Track}})^2 \cdot \epsilon_{\text{ST Vertex}}, \\ N_{\text{ST+LRT}} &= K_S \text{ produced} \times (\epsilon_{\text{ST Track}} \cdot \epsilon_{\text{LRT Track}}) \cdot \epsilon_{\text{ST+LRT Vertex}}, \\ N_{\text{LRT}} &= K_S \text{ produced} \times (\epsilon_{\text{LRT Track}})^2 \cdot \epsilon_{\text{LRT Vertex}}, \end{aligned} \quad (9.1)$$

where  $N$  represents vertex yields in each category.  $\epsilon_{\text{ST Track}}$  and  $\epsilon_{\text{LRT Track}}$  represent track reconstruction efficiency in the ST and the LRT, respectively.  $\epsilon_{\text{ST Vertex}}$ ,  $\epsilon_{\text{ST+LRT Vertex}}$ , and  $\epsilon_{\text{LRT Vertex}}$  represent two-track vertex reconstruction efficiency on two standard, two large-radius, or one standard and one large-radius tracks.

In order to compare the efficiency between data and MC samples, the  $K_S$  yields of LRT type in data is normalized to the MC for  $K_S$  found with the ST,

$$\text{Normalized data to MC} = \frac{N_{\text{LRT}} \cdot \left( N_{\text{ST}}^{\text{MC}} / N_{\text{ST}} \right)}{N_{\text{LRT}}^{\text{MC}}}, \quad (9.2)$$

where quantities estimated using MC samples are denoted by MC, and quantities estimated using data are denoted otherwise. Using Eqs. 9.1– 9.2, the systematic uncertainty in track and vertex reconstruction is expressed as,

$$\frac{N_{\text{LRT}} / N_{\text{ST}}}{N_{\text{LRT}}^{\text{MC}} / N_{\text{ST}}^{\text{MC}}} = \frac{\frac{(\epsilon_{\text{LRT Track}})^2 \cdot \epsilon_{\text{LRT Vertex}}}{(\epsilon_{\text{ST Track}})^2 \cdot \epsilon_{\text{ST Vertex}}}}{\frac{(\epsilon_{\text{LRT Track}}^{\text{MC}})^2 \cdot \epsilon_{\text{LRT Vertex}}^{\text{MC}}}{(\epsilon_{\text{ST Track}}^{\text{MC}})^2 \cdot \epsilon_{\text{ST Vertex}}^{\text{MC}}}}} \quad (9.3)$$

$$\left( \frac{\epsilon_{\text{LRT Track}}}{\epsilon_{\text{LRT Track}}^{\text{MC}}} \right)^2 \cdot \left( \frac{\epsilon_{\text{LRT Vertex}}}{\epsilon_{\text{LRT Vertex}}^{\text{MC}}} \right) = \left( \frac{N_{\text{LRT}} \cdot N_{\text{ST}}^{\text{MC}}}{N_{\text{LRT}}^{\text{MC}} \cdot N_{\text{ST}}^{\text{MC}}} \right) \cdot \left( \frac{\epsilon_{\text{ST Track}}}{\epsilon_{\text{ST Track}}^{\text{MC}}} \right)^2 \cdot \left( \frac{\epsilon_{\text{ST Vertex}}}{\epsilon_{\text{ST Vertex}}^{\text{MC}}} \right). \quad (9.4)$$

Events are selected using the same event selection described in Section 6.1 except trigger filters as the high- $p_T$  photon or muon triggers are not suitable for  $K_S$  study. From the selected events,  $K_S$  candidates, referred as  $K_S$  vertices, are selected by applying  $K_S$  vertex selection to secondary vertices in the events. The  $K_S$  vertex selection is similar to the  $Z'$  signal vertex selection, but for background reduction, additional vertex cuts motivated by Ref. [62] are applied. The mass window of 0.35 to 0.65 GeV is used in the  $K_S$  vertex selection. The difference between  $K_S$  and  $Z'$  vertex selections are summarized in Table 9.1.

After applying the event and  $K_S$  vertex selection, the  $K_S$  vertex distributions in the

	$Z'$	$K_S$
Trigger	Photon or muon trigger (Table 6.1)	-
Vertex type	$\mu^+\mu^-$ , $e^\pm\mu^\mp$ , $e^+e^-$	$x^+x^-$
Mass (GeV)	$> 10.0$	[0.35, 0.65]
Additional cut	-	$ \Delta z_0  < 2 \text{ mm}$ Decay length $> 15 \text{ mm}$

Table 9.1: Comparison of  $Z'$  and  $K_S$  vertex selections.

data and MC samples are compared in Figure 9.1. The data sample is normalized to the MC samples which have limited statistics. Only  $K_S$  vertices with two large-radius tracks are shown. The distributions show good agreement in the invariant mass,  $p_T$ , transverse and longitudinal position, and decay length of the vertices, except the pile-up distribution as expected.

$K_S$  vertices found in the data and the MC samples are binned in decay radius,  $r$ , and the  $K_S$  yields in each bin are estimated after subtracting the background contributions using side-bands (350 - 450, 550 - 650 GeV) in the invariant mass distribution. Figure 9.2 shows the mass distribution of  $K_S$  vertex with two large-radius tracks from the data and the MC samples. The figure shows that backgrounds are small and uniform in the mass window, and the mass distributions are in good agreement between the data and the MC samples.

The  $K_S$  yields with two large-radius tracks are compared between data and MC samples in Figure 9.3, where the data is normalized by a factor of  $N_{\text{ST}}/N_{\text{ST}}^{\text{MC}}$ , integrated over  $r$ . The ratio between two, representing the double ratio (Eq. 9.2), is shown in the lower pane.

In estimating the systematic uncertainty, largest discrepancy (4%), shown in the fourth bin, is taken as a conservative estimate of  $(N_{\text{LRT}} \cdot N_{\text{ST}}^{\text{MC}})/(N_{\text{LRT}}^{\text{MC}} \cdot N_{\text{ST}})$ . The results from previous studies show that the systematic uncertainty in the standard tracking is 2% [63], and the systematic uncertainty in secondary vertex reconstruction using standard tracks is 1% [60]. The study on secondary vertex reconstruction is performed using min-bias data, but the relatively uniform distribution of efficiency as a function of pile-up (Figure 7.10e) suggests that this result is still applicable for data with  $\langle \mu \rangle \approx 24$ . Using Eq. 9.4 together with these results, the systematic uncertainty in track and vertex reconstruction in the LRT is estimated to be 10%<sup>5</sup>.

<sup>5</sup>10% is a rounded estimate of the calculation,  $1.04 \cdot 1.02^2 \cdot 1.01 \approx 1.093$

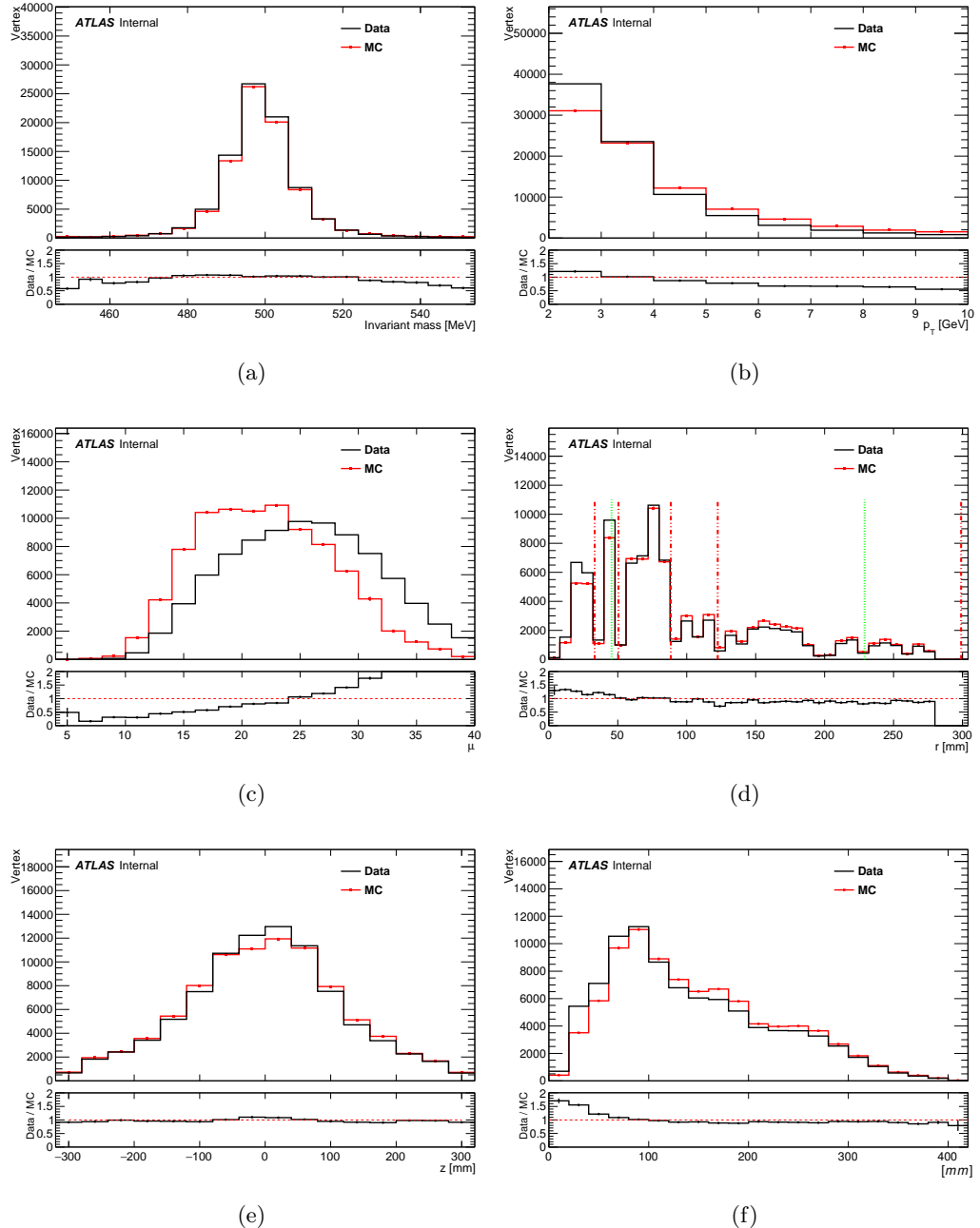


Figure 9.1: Comparison of the (a) invariant mass, (b)  $p_T$ , (c)  $\mu$ , (d) transverse, (e) longitudinal position, and (f) decay length of  $K_S$  vertex with two large-radius tracks in the data with the MC samples. Data is normalized to MC. In (d), the red dashed lines indicate the four pixel layers and the first layer of SCT. The green dotted lines indicate the Inner Support Tube (45.5 mm) and Pixel Support Tube (229 mm). MC sample is reweighted to the pile-up distribution in the data.

### 9.1.1 Systematic uncertainties on background estimations

There are two main sources of background in this analysis; cosmic muon background and random crossing background. The cosmic muon background estimation was outlined in Section 8.1. From this technique, the estimate is  $0.27 \pm 0.14$  (stat.) events. This  $\pm 0.14$  is taken to be the total uncertainty on this background. In the case of the random crossing, the estimate from the TF method is used as the central value,  $3.95 \times 10^{-3}$ , and the difference between the TF and event mixing method,  $1.5 \times 10^{-3}$ , is used as the uncertainty on the random-crossing background.

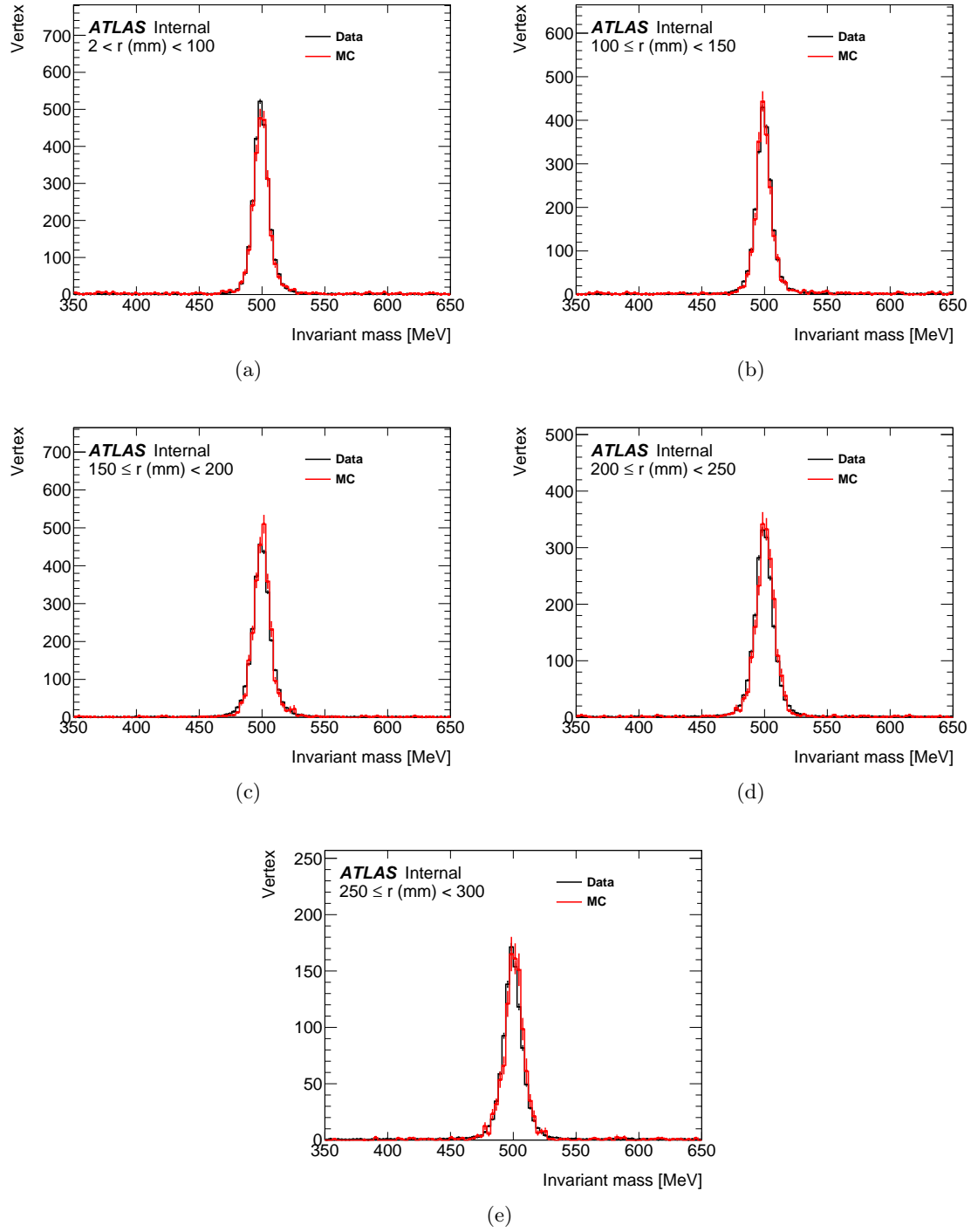


Figure 9.2: Representative distributions of the invariant mass of  $K_S$  candidates with two large-radius tracks for (a)  $2 < r < 100$  mm, (b)  $100 < r < 150$  mm, (c)  $150 < r < 200$  mm, (d)  $200 < r < 250$  mm, and (e)  $250 < r < 300$  mm in the data and the MC samples. Data is normalized to MC samples.

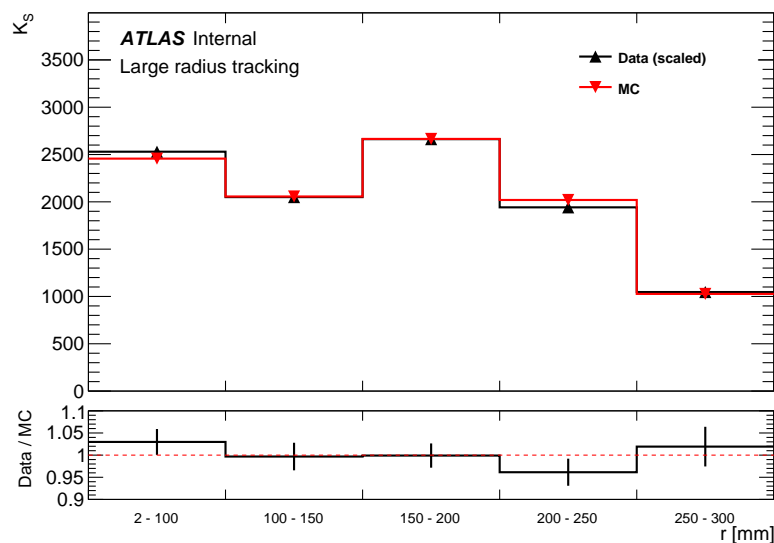


Figure 9.3: The radial distribution of  $K_S$  yields with two large-radius tracks. Data is normalized to the MC for  $K_S$  found with the ST tracking.

# Chapter 10

## INTERPRETATION OF RESULTS

No events were observed in data that satisfies the signal selection, and the result is consistent with the SM expectations. Therefore, upper limits (ULs) are set on the cross section times branching ratio ( $\sigma \times \text{BR}$ ) for resonances decaying to a dilepton.

### 10.1 Statistical Procedure

The limits are calculated using *HistFitter v0.61.0* [64], a statistical tool used for limit settings in ATLAS. The limit setting procedure is based on the modified Frequentist method,  $\text{CL}_s$  [65, 66]. In this framework, a number of events,  $n$ , is modeled as a Poisson distribution with the mean  $\lambda = \mu_{\text{sig}} \cdot s + b$  where  $\mu_{\text{sig}}$  is the signal strength parameter. The systematic uncertainty estimated in Chapter 9 is introduced as the nuisance parameter  $\theta$  to  $s$  and  $b$ , i.e.  $s$  and  $b$  become a function of  $\theta$ . The method uses the LHC default one-sided profile likelihood ratio  $q_{\mu_{\text{sig}}}$  as a test statistic,

$$q_{\mu_{\text{sig}}} = -2 \log \left( \frac{L(n_{\text{obs}} | \mu_{n_{\text{sig}}}, \hat{\theta})}{L(n_{\text{obs}} | \hat{\mu}_{\text{sig}}, \hat{\theta})} \right) \quad (10.1)$$

where  $L$  is the likelihood function,  $\hat{\mu}_{\text{sig}}$ ,  $\hat{\theta}$  are the values that globally maximize the likelihood,  $\hat{\theta}$  is the value that maximizes the likelihood for the specific value of  $\mu_{\text{sig}}$ , and  $n_{\text{obs}}$  is the observed number of events in data or in pseudo experiments.

The distributions of the test statistic  $q_{\mu_{\text{sig}}}$  for the signal + background and background hypothesis ( $\mu_{\text{sig}} = 1$  or  $\mu_{\text{sig}} = 0$ ) are obtained from multiple pseudo experiments, and the Frequentist probability (or  $p$ -value) is calculated from the distributions as,

$$\begin{aligned} \text{CL}_{s+b} &= P(q_{\mu_{\text{sig}}} > q_{\mu_{\text{sig}}}^{\text{obs}} \mid \mu_{\text{sig}} = 1), \\ \text{CL}_b &= P(q_{\mu_{\text{sig}}} > q_{\mu_{\text{sig}}}^{\text{obs}} \mid \mu_{\text{sig}} = 0), \end{aligned} \quad (10.2)$$

where  $\text{CL}_{s+b}$  is the probability to obtain a test statistic value more extreme than the observed test statistic,  $q_{\mu_{\text{sig}}}^{\text{obs}}$ , assuming signal + background hypothesis ( $\mu_{\text{sig}} = 1$ ), and  $\text{CL}_b$  is the corresponding probability for background hypothesis. Using these confidence levels, the signal confidence level,  $\text{CL}_s$ , is defined as

$$\text{CL}_s = \frac{\text{CL}_{s+b}}{\text{CL}_b}. \quad (10.3)$$

The UL at the 95% confidence level are obtained by adjusting  $\mu_{\text{sig}}$  until  $\text{CL}_s$  reaches 0.05, and the limit is translated to the  $\sigma \times \text{BR}$  by the relation,

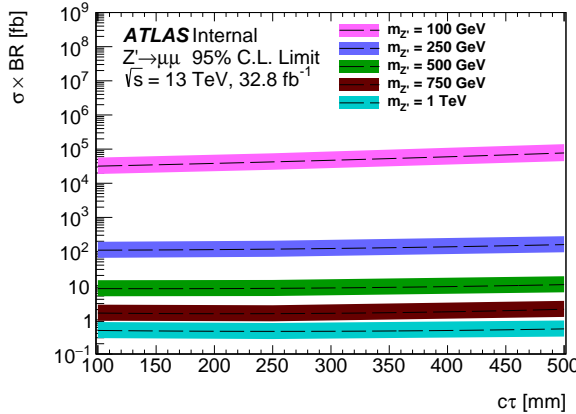
$$\mathcal{L}_{\text{Int.}} \cdot (\sigma \cdot \text{BR}) \cdot \epsilon = \mu_{\text{sig}} \cdot s + b, \quad (10.4)$$

where  $\mathcal{L}_{\text{Int.}}$  is the integrated luminosity and  $\epsilon$  is the signal efficiency.

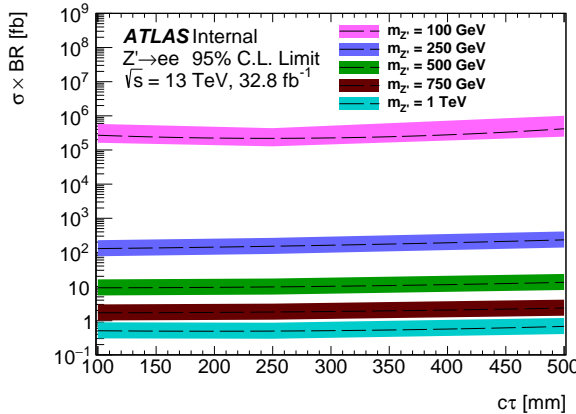
## 10.2 Upper limits

The observed ULs are evaluated by performing pseudo experiments with an expected background of  $0.27 \pm 0.14$  events, the systematic uncertainty of 10%, and the uncertainty of the luminosity measurement of 2.2%.

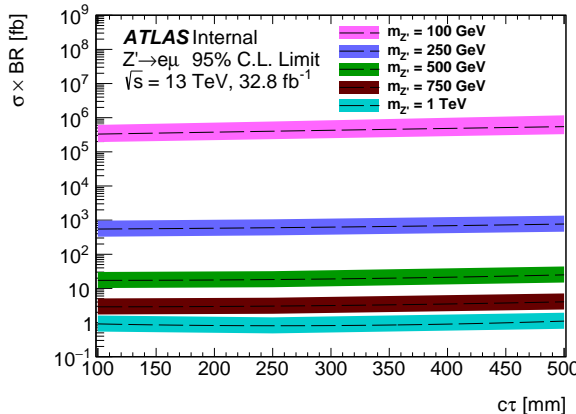
The observed ULs at 95% CL on  $\sigma \times \text{BR}$  for  $Z' \rightarrow \mu^+ \mu^-$ ,  $e^+ e^-$ , and  $e^\pm \mu^\mp$  are shown in Figure 10.1 as a function of  $c\tau$ . The observed limits are relatively uniform in  $c\tau$  for all channels. At  $m_{Z'} = 1$  TeV, the ULs are from 0.5 - 0.9 fb. At  $m_{Z'} = 100$  GeV, the ULs are much larger (50 - 400 pb) than other mass points due to the limited trigger efficiency.



(a)



(b)



(c)

Figure 10.1: The observed 95% CL upper limits on the  $\sigma \times \text{BR}$  for the  $Z' \rightarrow$  (a)  $\mu^+ \mu^-$ , (b)  $e^+ e^-$ , and (c)  $e^\pm \mu^\mp$  signal samples with  $Z'$  masses of 100 - 1000 GeV as a function of  $c\tau$ . The dashed lines are expected limits, and the solid bands represent  $1\sigma$  uncertainty on the expected limit.

# Chapter 11

## CONCLUSION

A search for long-lived  $Z'$  decaying to a  $\mu\mu$ ,  $ee$ , or  $e\mu$  pair is performed using  $32.8 \text{ fb}^{-1}$  of  $pp$  collisions at  $\sqrt{s} = 13 \text{ TeV}$  with the ATLAS detector at the LHC. No events were observed, and the results are consistent with an expected background of  $0.27 \pm 0.14$  events. Upper limits are set on  $\sigma \times \text{BR}$  for resonances decaying to a dilepton, and the resulting upper limits at the 95% CL are 50 - 400 pb at  $m_{Z'} = 100 \text{ GeV}$  and 0.5-0.9 fb at  $m_{Z'} = 1 \text{ TeV}$ . Also presented is the signal efficiency as a function of  $p_T$  and  $\eta$  for resonances decaying to a dilepton with typical values of 10-20% within the tracking coverage.

## BIBLIOGRAPHY

- [1] C. P. Burgess and G. D. Moore, *The standard model: a primer*. Cambridge Univ. Press, Cambridge, 2007. <http://cds.cern.ch/record/1003111>.
- [2] P. W. Higgs, *Broken symmetries and the masses of gauge bosons*, Phys. Rev. **13** (1964) 508, <http://cds.cern.ch/record/429539>.
- [3] H. Hata, *Color confinement as a result of restoration of local gauge symmetry*, Tech. Rep. HE-TH-81-13, KUNS-618, Kyoto Univ., Kyoto, Nov, 1981.  
<http://cds.cern.ch/record/135318>.
- [4] V. A. Kostelecký, *Gravity, Lorentz violation, and the standard model*, Phys. Rev. D **69** (2004), <https://link.aps.org/doi/10.1103/PhysRevD.69.105009>.
- [5] M. Magg, Q. Shafi, and C. Wetterich, *Gauge hierarchy in the presence of discrete symmetry*, Phys. Rev. B **87** (1979) 227, <http://cds.cern.ch/record/875284>.
- [6] M. Magg and C. Wetterich, *Neutrino mass problem and gauge hierarchy*, Phys. Rev. B **94** (1980) 61, <http://cds.cern.ch/record/133759>.
- [7] ATLAS Collaboration, *Searches for dark matter in ATLAS*, Tech. Rep. ATL-PHYS-PROC-2017-112, CERN, Geneva, Aug, 2017.  
<http://cds.cern.ch/record/2281629>.
- [8] G. Bertone, D. Hooper, and J. Silk, *Particle dark matter: evidence, candidates and constraints*, Phys. Rept. **405** (2005) 279.
- [9] D. Clowe, M. Bradač, A. H. Gonzalez, et al., *A direct empirical proof of the existence of dark matter*, The Astrophysical Journal Letters **648** (2006) 109.
- [10] M. Ahn, S. Aoki, H. Bhang, et al., *Indications of neutrino oscillation in a 250 km long-baseline experiment*, Phys. Rev. **90** (2003) 041801.
- [11] D. Toussaint, S. Treiman, F. Wilczek, et al., *Matter-antimatter accounting, thermodynamics, and black-hole radiation*, Phys. Rev. D **19** (1979) 1036.

- [12] M. Dine and A. Kusenko, *Origin of the matter-antimatter asymmetry*, Reviews of Modern Physics **76** (2003) 1.
- [13] M. J. Strassler and K. M. Zurek, *Echoes of a hidden valley at hadron colliders*, Phys. Rev. B **651** (2007) 374.
- [14] S. Cassel, D. Ghilea, and G. Ross, *Electroweak and dark matter constraints on a  $Z'$  in models with a hidden valley*, Nuclear Physics B **827** (2010) 256.
- [15] G. Senjanovic and R. N. Mohapatra, *Exact left-right symmetry and spontaneous violation of parity*, Phys. Rev. D **12** (1975) 1502.
- [16] R. N. Mohapatra and G. Senjanović, *Neutrino masses and mixings in gauge models with spontaneous parity violation*, Phys. Rev. D **23** (1981) 165.
- [17] R. Barbier, C. Berat, M. Besancon, et al., *R-parity violating supersymmetry*, Phys. Rept. **420** (2005) 1, [arXiv:hep-ph/0406039](https://arxiv.org/abs/hep-ph/0406039).
- [18] L. Basso, A. Belyaev, S. Moretti, et al., *Phenomenology of the minimal  $B$ - $L$  extension of the standard model:  $Z'$  and neutrinos*, Phys. Rev. **D80** (2009) 055030, [arXiv:0812.4313 \[hep-ph\]](https://arxiv.org/abs/0812.4313).
- [19] P. Langacker, *The physics of heavy  $Z'$  gauge bosons*, Rev. Mod. Phys. **81** (2009) 1199, [arXiv:0801.1345 \[hep-ph\]](https://arxiv.org/abs/0801.1345).
- [20] V. Barger, W. Keung, and E. Ma, *Sequential  $W$  and  $Z$  bosons*, Phys. Rev. B **94** (1980) 377, <http://www.sciencedirect.com/science/article/pii/0370269380909004>.
- [21] Q.-H. Cao, Z. Li, J.-H. Yu, et al., *Discovery and identification of  $W'$  and  $Z'$  in  $SU(2)_1 \otimes SU(2)_2 \otimes U(1)_X$  models at the LHC*, Phys. Rev. D **86** (2012) 095010, <https://link.aps.org/doi/10.1103/PhysRevD.86.095010>.
- [22] DØ Collaboration, *Search for a heavy neutral gauge boson in the dielectron channel with  $5.4 \text{ fb}^{-1}$  of  $p\bar{p}$  collisions at  $\sqrt{s} = 1.96 \text{ TeV}$* , Phys. Rev. B **695** (2011) 88, <http://www.sciencedirect.com/science/article/pii/S0370269310012700>.
- [23] ATLAS Collaboration, *Search for high-mass dilepton resonances in  $pp$  collisions at  $\sqrt{s} = 8 \text{ TeV}$  with the ATLAS detector*, Phys. Rev. D **90** (2014) 052005, <https://link.aps.org/doi/10.1103/PhysRevD.90.052005>.
- [24] ATLAS Collaboration, *Search for massive, long-lived particles using multitrack displaced vertices or displaced lepton pairs in  $pp$  collisions at  $\sqrt{s} = 8 \text{ TeV}$  with the ATLAS detector*, Phys. Rev. D **92** (2015) 072004, <https://cds.cern.ch/record/2010949>.
- [25] CMS Collaboration, *Search in leptonic channels for heavy resonances decaying to long-lived neutral particles*, JHEP **02** (2012) 085, <https://cds.cern.ch/record/1493239>.
- [26] ATLAS Collaboration, *Search for new phenomena in dijet events using  $37 \text{ fb}^{-1}$  of  $pp$  collision data collected at  $\sqrt{s} = 13 \text{ TeV}$  with the ATLAS detector*, Phys. Rev. D **96** (2017) 052004, [arXiv:1703.09127 \[hep-ex\]](https://arxiv.org/abs/1703.09127).

- [27] CMS Collaboration, *Search for dijet resonances in proton–proton collisions at  $\sqrt{s} = 13$  TeV and constraints on dark matter and other models*, Phys. Rev. **B769** (2017) 520, arXiv:1611.03568 [hep-ex].
- [28] O. S. Brüning, P. Collier, P. Lebrun, et al., *LHC design report*. CERN, Geneva, 2004. <https://cds.cern.ch/record/782076>.
- [29] H. Pernegger, *The Pixel detector of the ATLAS experiment for LHC Run-2*, Journal of Instrumentation **10** (2015) C06012, <http://stacks.iop.org/1748-0221/10/i=06/a=C06012>.
- [30] ATLAS Collaboration, *Production and integration of the ATLAS insertable B-layer*, Tech. Rep. arXiv:1803.00844, Mar, 2018. <http://cds.cern.ch/record/2307576>.
- [31] ATLAS Collaboration, *The barrel modules of the ATLAS semi-conductor tracker*, Tech. Rep. ATL-INDET-PUB-2006-005, ATL-COM-INDET-2006-009, CERN-ATL-COM-INDET-2006-009, CERN, Geneva, Jul, 2006. <https://cds.cern.ch/record/974073>.
- [32] ATLAS Collaboration, *ATLAS SCT endcap module production*, Tech. Rep. ATL-INDET-PUB-2006-007, ATL-COM-INDET-2006-008, CERN, Geneva, Jul, 2006. <https://cds.cern.ch/record/973395>.
- [33] ATLAS Collaboration, *ATLAS transition radiation tracker (TRT): straw tube gaseous detectors at high rates*, Tech. Rep. ATL-INDET-PROC-2013-005, CERN, Geneva, Apr, 2013. <https://cds.cern.ch/record/1537991>.
- [34] ATLAS Collaboration, *Particle identification performance of the ATLAS transition radiation tracker*, Tech. Rep. ATLAS-CONF-2011-128, CERN, Geneva, Sep, 2011. <https://cds.cern.ch/record/1383793>.
- [35] ATLAS Collaboration, *The ATLAS liquid argon calorimeter: overview and performance*, Journal of Physics: Conference Series **293** (2011) 012044, <http://stacks.iop.org/1742-6596/293/i=1/a=012044>.
- [36] ATLAS Collaboration, *The ATLAS tile calorimeter*, Tech. Rep. ATL-TILECAL-PROC-2015-002, CERN, Geneva, Mar, 2015. <https://cds.cern.ch/record/2004868>.
- [37] ATLAS Collaboration, *ATLAS liquid-argon calorimeter: technical design report*. CERN, Geneva, 1996. <https://cds.cern.ch/record/331061>.
- [38] ATLAS Collaboration, *Performance of the ATLAS Liquid Argon Calorimeter after three years of LHC operation and plans for a future upgrade*, Journal of Instrumentation **9** (2014) C09007, <http://stacks.iop.org/1748-0221/9/i=09/a=C09007>.
- [39] ATLAS Collaboration, *Commissioning of the magnetic field in the ATLAS muon spectrometer*, Nuclear Physics B **177-178** (2008) 265, <http://www.sciencedirect.com/science/article/pii/S0920563207009528>.

- [40] ATLAS Collaboration, *The Run 2 ATLAS trigger system*, <http://stacks.iop.org/1742-6596/762/i=1/a=012003>.
- [41] ATLAS Collaboration, *The ATLAS trigger in Run-2: design, menu, and performance*, Tech. Rep. ATL-DAQ-PROC-2017-027, CERN, Geneva, Oct, 2017. <https://cds.cern.ch/record/2287548>.
- [42] ATLAS Collaboration, *The ATLAS Inner Detector commissioning and calibration*, Eur. Phys. J. **C70** (2010) 787–821, [arXiv:1004.5293](https://arxiv.org/abs/1004.5293) [physics.ins-det].
- [43] ATLAS Collaboration, *Performance of the reconstruction of large impact parameter tracks in the ATLAS inner detector*, Tech. Rep. ATL-PHYS-PUB-2017-014, CERN, Geneva, Jul, 2017. <https://cds.cern.ch/record/2275635>.
- [44] ATLAS Collaboration, *ATLAS Tracking Event Data Model*, Tech. Rep. ATL-SOFT-PUB-2006-004. ATL-COM-SOFT-2006-005. CERN-ATL-COM-SOFT-2006-005, CERN, Geneva, Jul, 2006. <https://cds.cern.ch/record/973401>.
- [45] ATLAS Collaboration, *Reconstruction of primary vertices at the ATLAS experiment in Run 1 proton–proton collisions at the LHC*, Eur. Phys. J. **C77** (2017) 332, [arXiv:1611.10235](https://arxiv.org/abs/1611.10235) [physics.ins-det].
- [46] ATLAS Collaboration, *Performance of the ATLAS track reconstruction algorithms in dense environments in LHC Run 2*, Eur. Phys. J. **C77** (2017) 673, [arXiv:1704.07983](https://arxiv.org/abs/1704.07983) [hep-ex].
- [47] ATLAS Collaboration, *Electron reconstruction and identification efficiency measurements with the ATLAS detector using the 2011 LHC proton-proton collision data*, Eur. Phys. J. **C74** (2014) 2941, [arXiv:1404.2240](https://arxiv.org/abs/1404.2240) [hep-ex].
- [48] ATLAS Collaboration, *Muon reconstruction performance of the ATLAS detector in proton–proton collision data at  $\sqrt{s} = 13$  TeV*, Eur. Phys. J. **C76** (2016) 292, [arXiv:1603.05598](https://arxiv.org/abs/1603.05598) [hep-ex].
- [49] ATLAS Collaboration, *Primary vertex reconstruction in the ATLAS experiment at LHC*, Journal of Physics: Conference Series **119** (2008) 032033, <http://stacks.iop.org/1742-6596/119/i=3/a=032033>.
- [50] R. E. Kalman, *A new approach to linear filtering and prediction problems*, Trans. ASME, D **82** (1960) 35, <https://cds.cern.ch/record/434680>.
- [51] ATLAS Collaboration, *Search for long-lived, weakly-interacting particle that decay to displaced hadronic jets in proton-proton collisions at  $\sqrt{s} = 8$  TeV with the ATLAS detector*, Tech. Rep. ATL-COM-PHYS-2013-683, CERN, Geneva, May, 2013. <https://cds.cern.ch/record/1550730>.
- [52] ATLAS Collaboration, *Searches for long-lived neutral particles decaying into heavy flavors in the hadronic calorimeter of ATLAS at  $\sqrt{s} = 8$  TeV*, Tech. Rep. ATL-COM-PHYS-2013-113, CERN, Geneva, Feb, 2013. <https://cds.cern.ch/record/1512932>.

- [53] ATLAS Collaboration, *Search for massive, long-lived particles using multitrack displaced vertices or displaced lepton pairs in pp collisions at  $\sqrt{s} = 8$  TeV with the ATLAS detector*, Phys. Rev. **D92** (2015) 072004, [arXiv:1504.05162 \[hep-ex\]](https://arxiv.org/abs/1504.05162).
- [54] ATLAS Collaboration, *Performance of the ATLAS Trigger System in 2015*, Eur. Phys. J. **C77** (2017) 317, [arXiv:1611.09661 \[hep-ex\]](https://arxiv.org/abs/1611.09661).
- [55] ATLAS Collaboration, *Report of the analysis model study group*, Tech. Rep. ATL-COM-SOFT-2013-005, CERN, Geneva, Apr, 2013.  
<https://cds.cern.ch/record/1543445>.
- [56] T. Sjöstrand, S. Mrenna, and P. Skands, *PYTHIA 6.4 physics and manual*, Journal of High Energy Physics **2006** (2006) 026,  
<http://stacks.iop.org/1126-6708/2006/i=05/a=026>.
- [57] NNPDF Collaboration, R. D. Ball et al., *Parton distributions for the LHC Run II*, JHEP **04** (2015) 040, [arXiv:1410.8849 \[hep-ph\]](https://arxiv.org/abs/1410.8849).
- [58] T. Gleisberg, S. Hoeche, F. Krauss, et al., *Event generation with SHERPA 1.1*, JHEP **02** (2009) 007, [arXiv:0811.4622 \[hep-ph\]](https://arxiv.org/abs/0811.4622).
- [59] ATLAS Collaboration, *The upgraded pixel detector of the ATLAS experiment for Run 2 at the Large Hadron Collider*, Tech. Rep. ATL-INDET-PROC-2015-015, CERN, Geneva, Dec, 2015. <https://cds.cern.ch/record/2110260>.
- [60] ATLAS Collaboration, *A measurement of material in the ATLAS tracker using secondary hadronic interactions in 7 TeV pp collisions*, JINST **11** (2016) 45, <https://cds.cern.ch/record/2215485>.
- [61] ATLAS Collaboration, *Search for long-lived, massive particles decaying into leptons in pp collisions at 13 TeV centre-of-mass energy, with the ATLAS detector at the LHC*, Tech. Rep. ATL-COM-PHYS-2017-1060, CERN, Geneva, Jul, 2017.  
<https://cds.cern.ch/record/2275055>.
- [62] S. H. Oh and C. Wang, *Kshort and lambda production in jets from pp collisions at 7 TeV center-of-mass energy.*, Tech. Rep. ATL-COM-PHYS-2014-1258, CERN, Geneva, Sep, 2014. <https://cds.cern.ch/record/1951024>.
- [63] ATLAS Collaboration, *Early inner detector tracking performance in the 2015 data at  $\sqrt{s} = 13$  TeV*, Tech. Rep. ATL-PHYS-PUB-2015-051, CERN, Geneva, Dec, 2015.  
<https://cds.cern.ch/record/2110140>.
- [64] M. Baak, G. J. Besjes, D. Côte, et al., *HistFitter software framework for statistical data analysis*, Eur. Phys. J. **C75** (2015) 153, [arXiv:1410.1280 \[hep-ex\]](https://arxiv.org/abs/1410.1280).
- [65] V. Obraztsov, *Confidence limits for processes with small statistics in several subchannels and with measurement errors*, Nuclear Instruments and Methods in Physics Research Section A: Accelerators, Spectrometers, Detectors and Associated Equipment **316** (1992) 388,  
<http://www.sciencedirect.com/science/article/pii/016890029290925T>.

- [66] G. J. Feldman and R. D. Cousins, *Unified approach to the classical statistical analysis of small signals*, Phys. Rev. D **57** (1998) 3873,  
<https://link.aps.org/doi/10.1103/PhysRevD.57.3873>.

## Appendix A: Trigger efficiency

The trigger efficiency of all  $Z'$  signal MC samples is shown in Table A.1. It is evident that at low  $Z'$  mass ( $\sim 100$  GeV), the combined trigger efficiency of the signal MC sample is significantly reduced because the typical  $p_T$  of the signal leptons is lower than the  $p_T$  threshold of the trigger.

$m_{Z'}$ (GeV)	$c\tau$ (mm)	Single muon (%)	Single photon (%)	Di-photon (%)	Combined (%)
100	100	$4.70 \pm 0.15$	$0.01 \pm 0.01$	$0.00 \pm 0.00$	$4.70 \pm 0.15$
100	250	$4.09 \pm 0.14$	$0.00 \pm 0.00$	$0.00 \pm 0.00$	$4.09 \pm 0.14$
100	500	$3.81 \pm 0.14$	$0.00 \pm 0.00$	$0.00 \pm 0.00$	$3.81 \pm 0.14$
250	100	$34.57 \pm 0.34$	$0.08 \pm 0.02$	$0.04 \pm 0.01$	$34.65 \pm 0.34$
250	250	$30.84 \pm 0.33$	$0.07 \pm 0.02$	$0.03 \pm 0.01$	$30.90 \pm 0.33$
250	500	$24.41 \pm 0.30$	$0.05 \pm 0.02$	$0.01 \pm 0.01$	$24.45 \pm 0.30$
500	100	$47.60 \pm 0.36$	$1.02 \pm 0.07$	$0.10 \pm 0.02$	$48.14 \pm 0.36$
500	250	$40.82 \pm 0.35$	$1.00 \pm 0.07$	$0.13 \pm 0.03$	$41.36 \pm 0.35$
500	500	$33.15 \pm 0.33$	$0.80 \pm 0.06$	$0.10 \pm 0.02$	$33.62 \pm 0.33$
750	100	$53.99 \pm 0.35$	$2.68 \pm 0.11$	$0.28 \pm 0.04$	$55.16 \pm 0.35$
750	250	$46.99 \pm 0.35$	$2.27 \pm 0.11$	$0.26 \pm 0.04$	$48.11 \pm 0.35$
750	500	$39.18 \pm 0.35$	$2.23 \pm 0.10$	$0.13 \pm 0.03$	$40.30 \pm 0.35$
1000	100	$56.91 \pm 0.35$	$3.96 \pm 0.14$	$0.35 \pm 0.04$	$58.46 \pm 0.35$
1000	250	$51.13 \pm 0.35$	$3.59 \pm 0.13$	$0.33 \pm 0.04$	$52.58 \pm 0.35$
1000	500	$43.14 \pm 0.35$	$3.24 \pm 0.13$	$0.34 \pm 0.04$	$44.52 \pm 0.35$

Table A.1: Trigger efficiency of single muon, single photon, di-photon triggers, and the combined trigger efficiency of the signal MC samples of  $Z' \rightarrow \mu^+ \mu^-$ . Statistical uncertainty is shown.

$m_{Z'}$ (GeV)	$c\tau$ (mm)	Single muon (%)	Single photon (%)	Di-photon (%)	Combined (%)
100	100	0.00±0.00	0.30±0.04	1.36±0.08	1.57±0.09
100	250	0.00±0.00	0.31±0.04	1.37±0.08	1.62±0.09
100	500	0.02±0.01	0.37±0.04	0.97±0.07	1.21±0.08
250	100	0.00±0.00	8.12±0.19	49.26±0.35	50.73±0.35
250	250	0.00±0.00	6.74±0.18	45.00±0.35	46.38±0.35
250	500	0.01±0.01	5.80±0.17	37.21±0.34	38.78±0.34
500	100	0.02±0.01	73.59±0.31	66.73±0.33	80.06±0.28
500	250	0.02±0.01	68.10±0.33	60.90±0.35	74.28±0.31
500	500	0.02±0.01	59.35±0.36	51.22±0.36	64.62±0.35
750	100	0.02±0.01	87.99±0.23	74.83±0.31	90.07±0.21
750	250	0.03±0.01	82.54±0.27	68.60±0.33	84.60±0.26
750	500	0.02±0.01	74.59±0.31	58.39±0.35	76.45±0.30
1000	100	0.03±0.01	92.45±0.19	79.87±0.28	93.61±0.17
1000	250	0.01±0.01	88.44±0.23	73.84±0.31	89.45±0.22
1000	500	0.04±0.01	81.57±0.28	64.60±0.35	82.45±0.28

(a)

Table A.2: Trigger efficiency of single muon, single photon, di-photon triggers, and the combined trigger efficiency of the signal MC samples of  $Z' \rightarrow e^+e^-$ . Statistical uncertainty is shown.

$m_{Z'}$ (GeV)	$c\tau$ (mm)	Single muon (%)	Single photon (%)	Di-photon (%)	Combined (%)
100	100	2.35±0.11	0.16±0.03	0.05±0.02	2.55±0.11
100	250	2.24±0.10	0.15±0.03	0.07±0.02	2.41±0.11
100	500	1.79±0.10	0.17±0.03	0.06±0.02	2.00±0.10
250	100	20.22±0.28	4.09±0.14	1.12±0.07	23.85±0.30
250	250	18.28±0.27	3.58±0.13	0.92±0.07	21.36±0.29
250	500	14.87±0.25	3.02±0.12	0.54±0.05	17.43±0.27
500	100	27.30±0.32	62.39±0.35	3.31±0.13	70.26±0.33
500	250	24.01±0.30	57.40±0.35	2.88±0.12	63.40±0.34
500	500	20.66±0.29	49.46±0.35	2.27±0.11	54.43±0.35
750	100	31.74±0.34	78.47±0.30	4.88±0.16	83.85±0.27
750	250	28.27±0.32	73.66±0.31	4.68±0.15	77.73±0.29
750	500	23.33±0.30	64.74±0.34	3.99±0.14	67.99±0.33
1000	100	34.07±0.35	84.66±0.27	6.35±0.18	88.72±0.24
1000	250	30.27±0.32	79.67±0.28	5.85±0.17	83.16±0.26
1000	500	26.61±0.32	71.87±0.33	5.21±0.16	74.55±0.32

(a)

Table A.3: Trigger efficiency of single muon, single photon, di-photon triggers, and the combined trigger efficiency of the signal MC samples of  $Z' \rightarrow e^\pm\mu^\mp$ . Statistical uncertainty is shown.

## Appendix B: Efficiency Map of Signal MC Samples

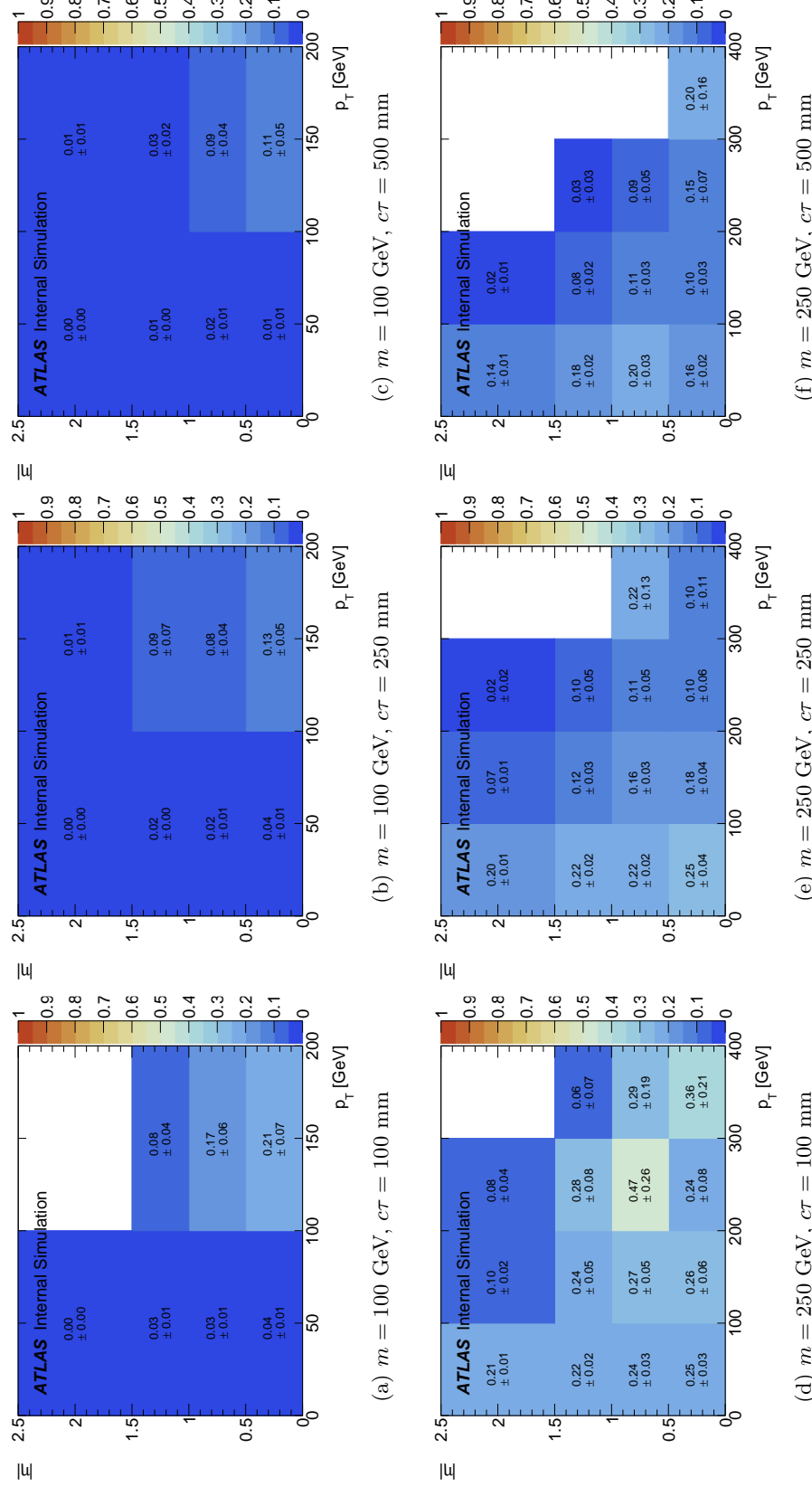


Figure B.1: Reconstruction efficiency map of  $|\eta|$  vs.  $p_T$  for  $Z' \rightarrow \mu^+ \mu^-$  MC sample with  $m_{Z'} = 100$  and  $250$  GeV.

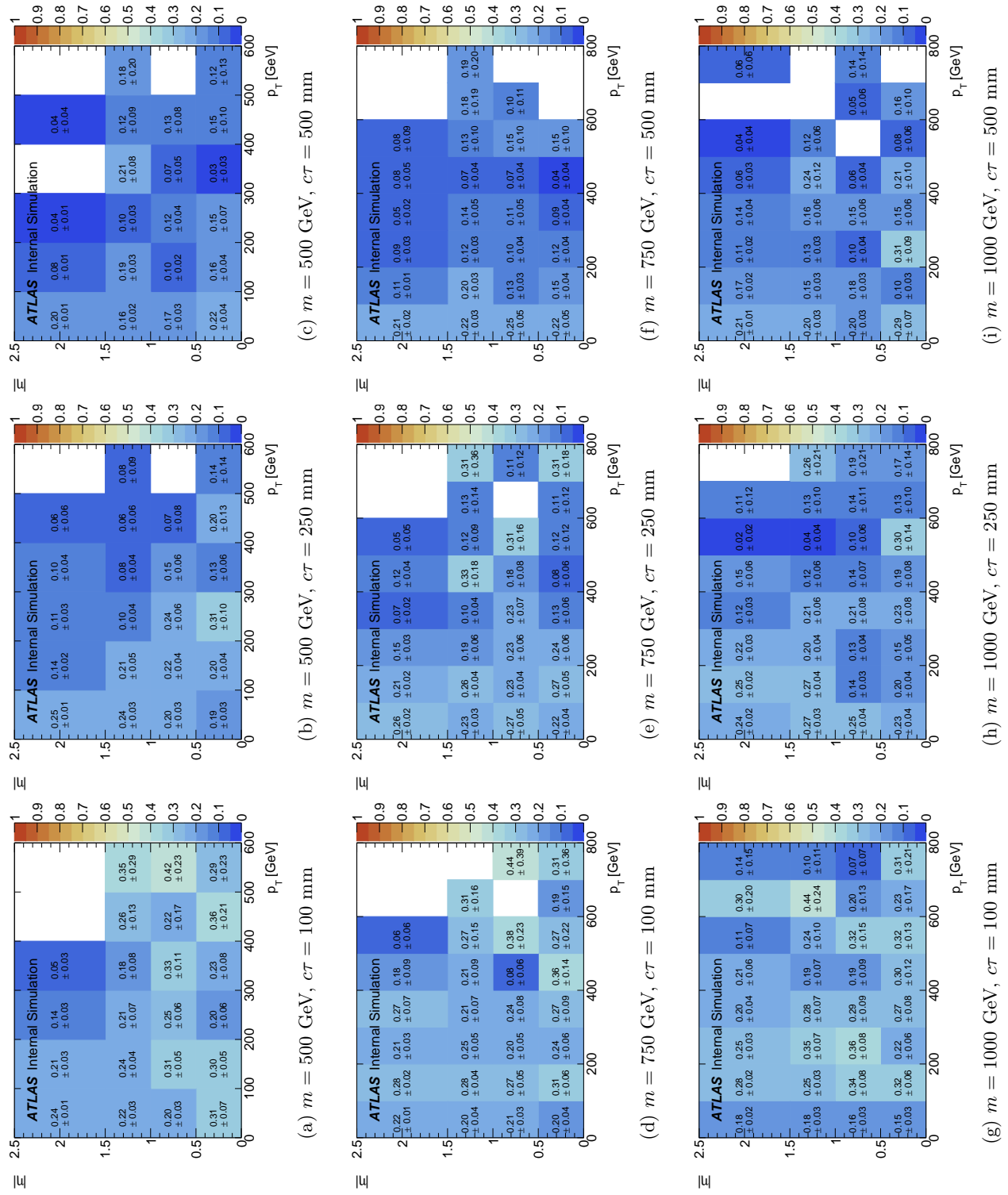


Figure B.2: Reconstruction efficiency map of  $|\eta|$  vs.  $p_T$  for  $Z' \rightarrow \mu^+ \mu^-$  MC sample with  $m_{Z'} = 500, 750$  and  $1000 \text{ GeV}$ .

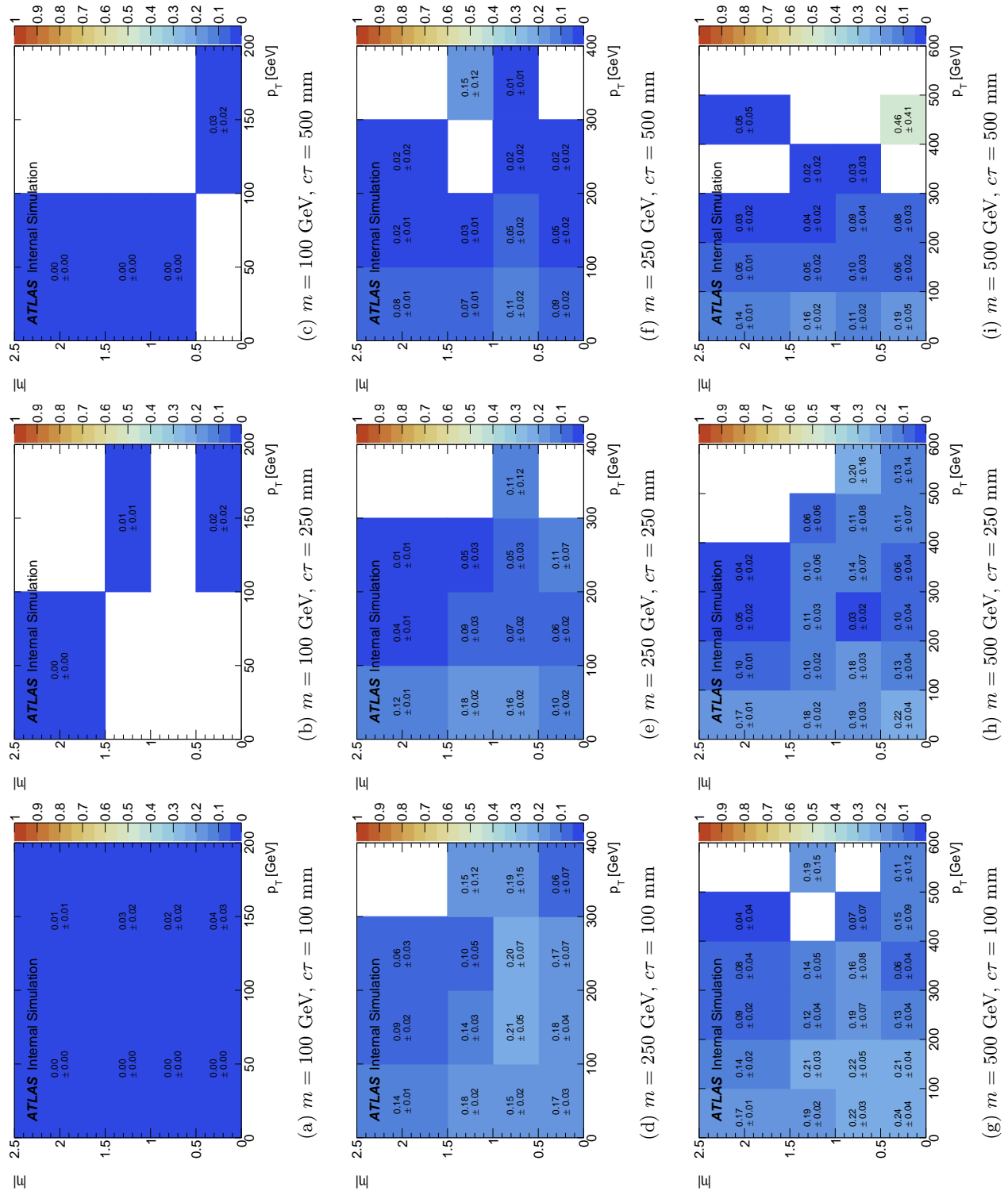


Figure B.3: Reconstruction efficiency map of  $|\eta|$  vs.  $p_T$  for  $Z' \rightarrow e^+e^-$  MC sample with  $m_{Z'} = 100, 250$  and  $500 \text{ GeV}$ .

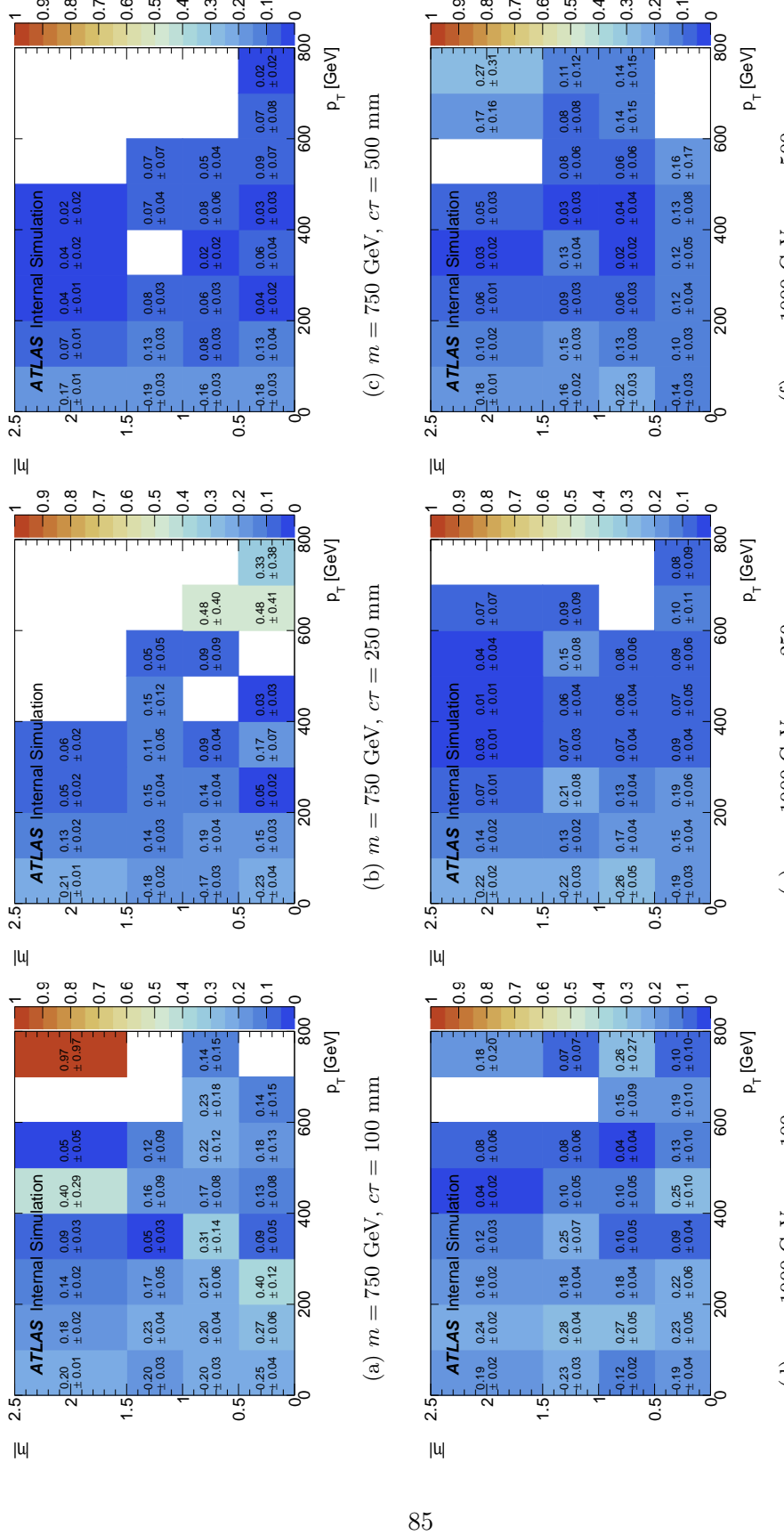


Figure B.4: Reconstruction efficiency map of  $|\eta|$  vs.  $p_T$  for  $Z' \rightarrow e^+ e^-$  MC sample with  $m_{Z'} = 750$  and  $1000 \text{ GeV}$ .

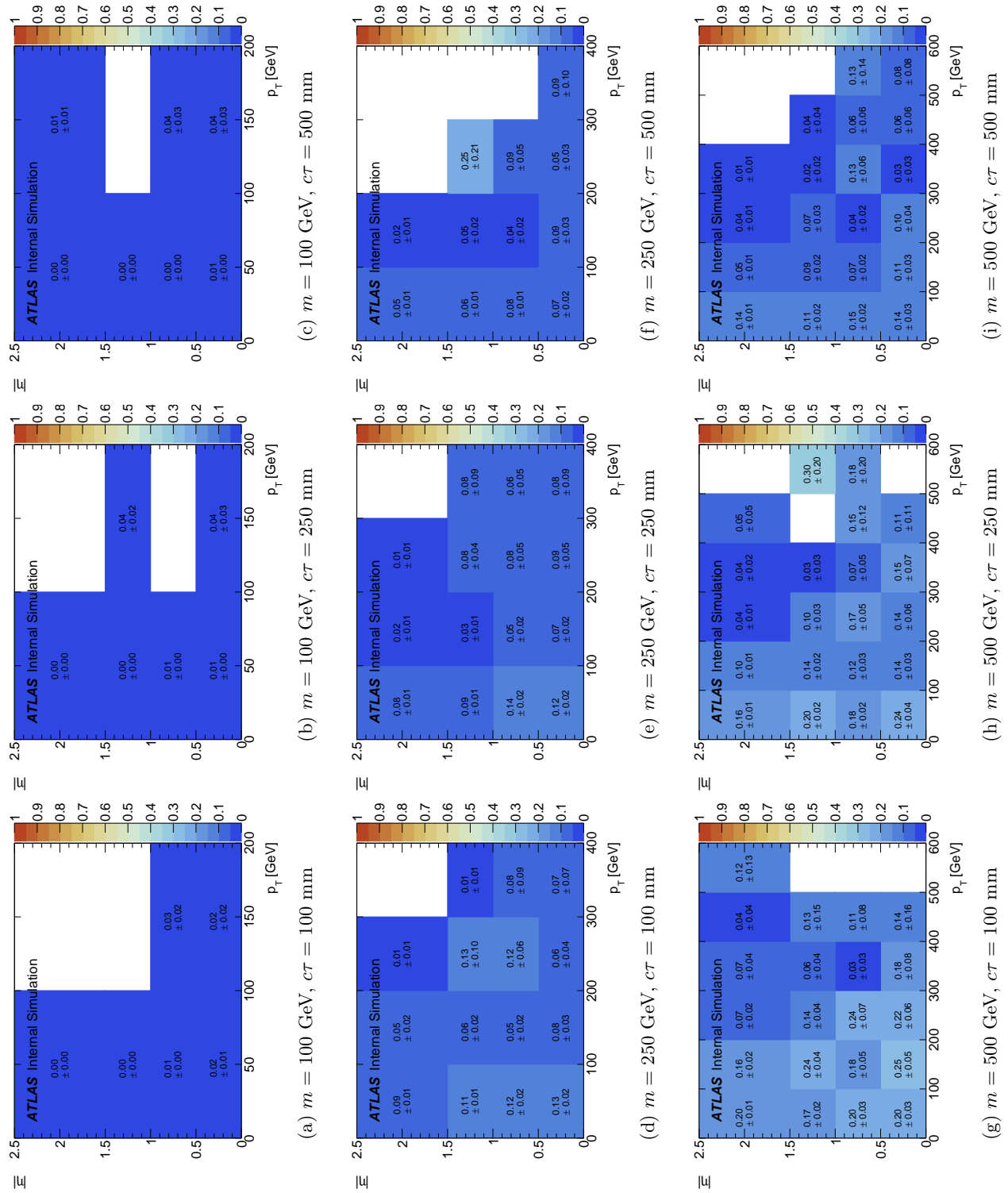


Figure B.5: Reconstruction efficiency map of  $|\eta|$  vs.  $p_T$  for  $Z' \rightarrow e^\pm \mu^\mp$  MC sample with  $m_{Z'} = 100, 250$  and  $500 \text{ GeV}$ .

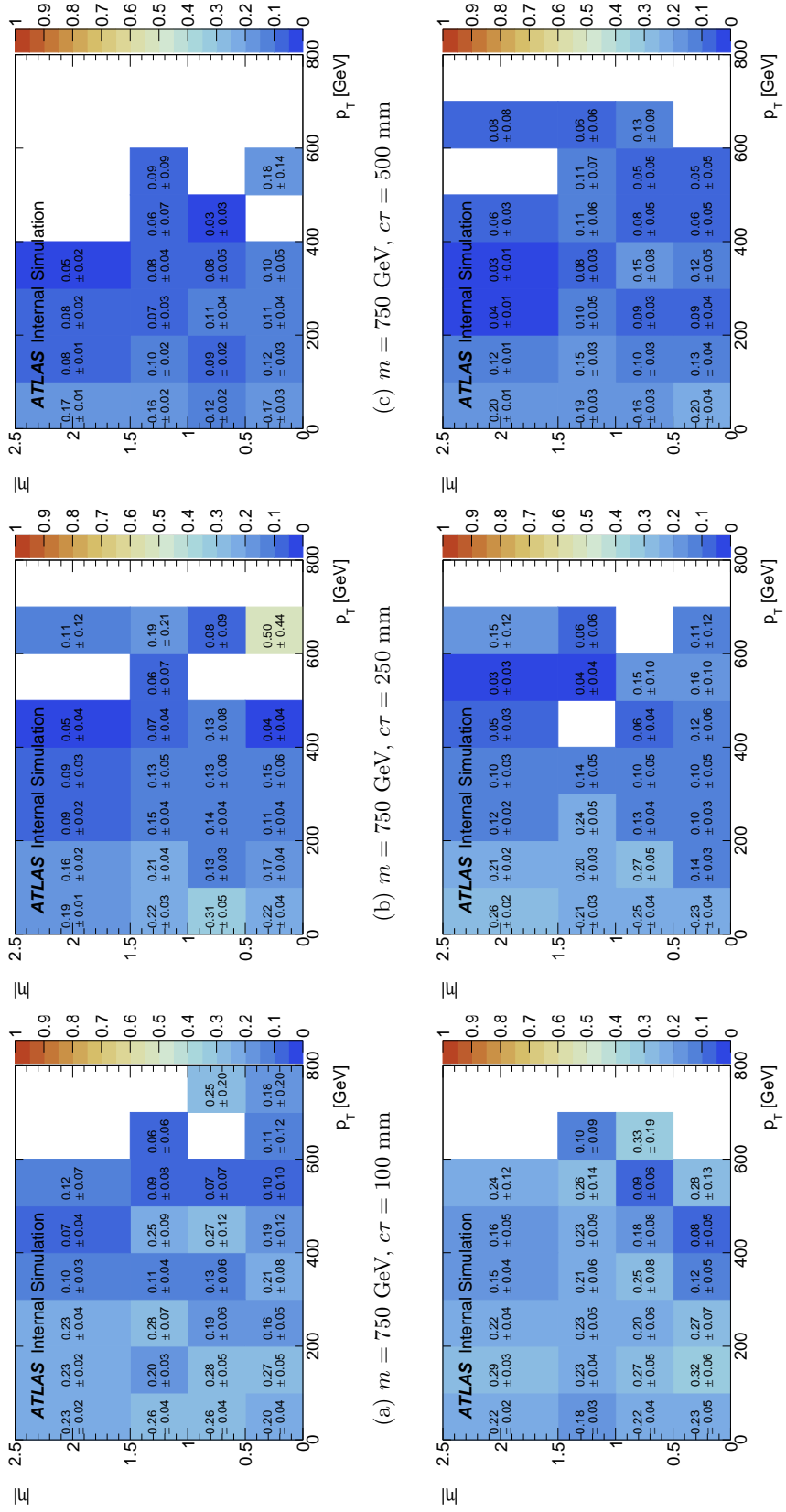


Figure B.6: Reconstruction efficiency map of  $|\eta|$  vs.  $p_T$  for  $Z' \rightarrow e^\pm \mu^\mp$  MC sample with  $m_{Z'} = 750$  and 1000 GeV.

## Appendix C: $K_S$ and $Z'$ comparison

The ideal  $K_S$  sample to estimate the systematic uncertainty in track and vertex reconstruction should have the same kinematic distributions as the  $Z'$  MC sample. Obviously, the two samples have different distributions. Figure C.7 shows comparisons of the vertex and kinematic distributions. The reconstructed  $K_S$  and  $Z'$  vertices are required to match to a  $K_S$  and  $Z'$  vertex produced at truth level with spatial displacement no larger than 0.7 mm. It is fortuitous that their distribution cover the  $r$  region of interest, and the two samples have similar  $z$  distribution. Obviously, the  $p_T$  distributions are quite different due to the different production mechanism of  $Z'$  and  $K_S$ .

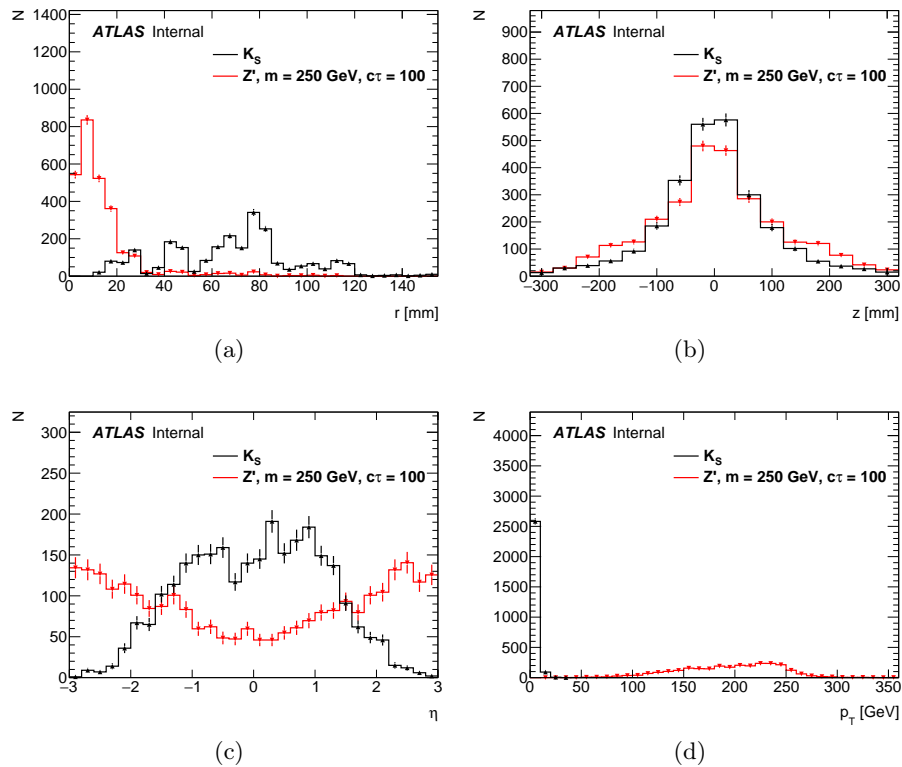


Figure C.7: Distribution of (a) transverse and (b) longitudinal position, (c)  $\eta$ , and (d)  $p_T$  of  $K_S$  and  $Z'$  vertices found in the  $Z'$  and genetic MC sample described in Section 5.2.2.  $Z'$  distribution is normalized to  $K_S$  distribution. Statistical uncertainties are shown.

## Appendix D: Extrapolation in the track flipping method

In this section, the extrapolation method used in the TF method is derived. The TF method estimates the number of vertices in the control ( $x^+x^-$ ), validation ( $\mu^\pm x^\mp$ ,  $e^\pm x^\mp$ ), and signal region ( $\mu^+\mu^-$ ,  $e^+e^-$ ,  $e^\pm\mu^\mp$ ) which represent the estimate of random-crossing background in each region. The vertex yields in the control and validation region are extrapolated into the signal region to estimate the random-crossing background.

### D.1 Definition

In this derivation, the following definition of  $\mu$ ,  $e$ , and  $x$  is used where lepton and non-leptonic tracks are mutually exclusive.

- $x$  = tracks that are not  $\mu$  or  $e$
- $e$  = electron tracks
- $\mu$  = muon tracks

Furthermore, the following conventions for the number of tracks, pairs, vertices, and lepton probability are used.

- $N_x$ ,  $N_e$ ,  $N_\mu$  represent the number of  $x$ ,  $e$ , and  $\mu$  tracks.
- $N_{xx}$ ,  $N_{\mu x}$ ,  $N_{ex}$ ,  $N_{\mu\mu}$ ,  $N_{ee}$ ,  $N_{e\mu}$  represent the number of pairs of each type.
- $N_{xx}^v$ ,  $N_{\mu x}^v$ ,  $N_{ex}^v$ ,  $N_{\mu\mu}^v$ ,  $N_{ee}^v$ ,  $N_{e\mu}^v$  represent the number of vertices of each type.
- $P_{(\mu)} = \frac{N_\mu}{N_\mu + N_e + N_x}$  represents the probability for a track being a muon.
- $P_{(e)} = \frac{N_e}{N_\mu + N_e + N_x}$  represents the probability for a track being an electron.

### D.2 Vertex estimation

A number of reconstructed vertices in the sample can be estimated by the number of track pairs in the sample and the probability of a pair to form a vertex, i.e.

$$N_{xx}^{v(\text{est})} = N_{xx} \times P_{(xx)}^v, \quad (\text{D.1})$$

where  $P_{(xx)}^v$  is the probability for a  $xx$  pair to form a vertex. Similarly, the vertexing probability for track pairs in the validation and signal region can be defined as below.

$$\begin{aligned} N_{\mu x}^v &= N_{\mu x} \times P_{(\mu x)}^v, \\ N_{ex}^v &= N_{ex} \times P_{(ex)}^v, \\ N_{\mu\mu}^v &= N_{\mu\mu} \times P_{(\mu\mu)}^v, \\ N_{ee}^v &= N_{ee} \times P_{(ee)}^v, \\ N_{e\mu}^v &= N_{e\mu} \times P_{(e\mu)}^v. \end{aligned} \quad (D.2)$$

### D.3 Counting pairs

Given a collection of  $x$  tracks in a single event, the number of all possible pairs can be expressed as,

$$N_{xx} = \binom{N_x}{2} = \frac{N_x!}{(N_x - 2)! \cdot 2!} = \frac{1}{2} \cdot (N_x \cdot (N_x - 1)). \quad (D.3)$$

Given two different sets of tracks, for example  $x$  and  $\mu$ , the number of possible pairs is

$$N_{\mu x} = N_\mu \cdot N_x. \quad (D.4)$$

Similarly, the number of pairs from other combinations of tracks are

$$\begin{aligned} N_{ee} &= \binom{N_e}{2} = \frac{N_e!}{(N_e - 2)! \cdot 2!} = \frac{1}{2} \cdot (N_e \cdot (N_e - 1)), \\ N_{\mu\mu} &= \binom{N_\mu}{2} = \frac{N_\mu!}{(N_\mu - 2)! \cdot 2!} = \frac{1}{2} \cdot (N_\mu \cdot (N_\mu - 1)), \\ N_{ex} &= N_e \cdot N_x, \\ N_{e\mu} &= N_e \cdot N_\mu. \end{aligned} \quad (D.5)$$

### D.4 Extrapolation of control region into validation and signal regions

The track-flipped vertex yield in the control region can be extrapolated into the validation and signal region as follows.

Given a number of tracks ( $\mu, e, x$ ), we can estimate the number of vertices in the validation and signal region using Eqs. D.2–D.5. However, since the vertexing probabilities in the validation and signal region ( $P_{(\mu x)}^v, P_{(ex)}^v$ , etc.) are unknown without using the information from those regions, the vertexing probability obtained from the control region,  $P_{(xx)}^v$ , is used as an estimation of the vertexing probability in the validation and the signal region.  $P_{(xx)}^v$  can be expressed as,

$$P_{(xx)}^v = \frac{N_{xx}^{v(\text{obs})}}{N_{xx}} = \frac{N_{xx}^{v(\text{obs})}}{\frac{1}{2} \cdot (N_x \cdot (N_x - 1))}. \quad (\text{D.6})$$

Using Eqs. D.2-D.6, the vertex yield in the validation and signal region can be estimated as,

$$\begin{aligned} N_{\mu x}^{v(\text{est})} &= N_{\mu x} \cdot P_{(\mu x)}^v \approx N_{\mu x} \cdot P_{(xx)}^v = 2 \cdot \frac{N_\mu}{N_x - 1} \cdot N_{xx}^{v(\text{obs})} \approx 2 \cdot P_{(\mu)} \cdot N_{xx}^{v(\text{obs})}, \\ N_{ex}^{v(\text{est})} &= N_{ex} \cdot P_{(ex)}^v \approx N_{ex} \cdot P_{(xx)}^v = 2 \cdot \frac{N_e}{N_x - 1} \cdot N_{xx}^{v(\text{obs})} \approx 2 \cdot P_{(e)} \cdot N_{xx}^{v(\text{obs})}, \\ N_{\mu\mu}^{v(\text{est})} &= N_{\mu\mu} \cdot P_{(\mu\mu)}^v \approx N_{\mu\mu} \cdot P_{(xx)}^v = \frac{N_\mu \cdot (N_\mu - 1)}{N_x \cdot (N_x - 1)} \cdot N_{xx}^{v(\text{obs})} \approx (P_{(\mu)})^2 \cdot N_{xx}^{v(\text{obs})}, \\ N_{ee}^{v(\text{est})} &= N_{ee} \cdot P_{(ee)}^v \approx N_{ee} \cdot P_{(xx)}^v = \frac{N_e \cdot (N_e - 1)}{N_x \cdot (N_x - 1)} \cdot N_{xx}^{v(\text{obs})} \approx (P_{(e)})^2 \cdot N_{xx}^{v(\text{obs})}, \\ N_{e\mu}^{v(\text{est})} &= N_{e\mu} \cdot P_{(e\mu)}^v \approx N_{e\mu} \cdot P_{(xx)}^v = N_e \cdot N_\mu \frac{2 \cdot N_{xx}^{v(\text{obs})}}{N_x \cdot (N_x - 1)} \approx 2 \cdot P_{(e)} \cdot P_{(\mu)} \cdot N_{xx}^{v(\text{obs})}, \end{aligned} \quad (\text{D.7})$$

where  $N^{v,\text{obs}}$  represents the measured track-flipped vertex yield in the data and  $N^{est}$  represents the estimated vertex yield in the validation and signal region by the extrapolation.

## D.5 Extrapolation of validation region into signal region

Similarly, the track-flipped vertex yield in the validation region can be extrapolated into the signal region by using  $P_{(\mu x)}^v$  and  $P_{(ex)}^v$  as estimates of  $P_{(\mu\mu)}^v$  and  $P_{(ee)}^v$  where,

$$\begin{aligned} P_{(\mu x)}^v &= \frac{N_{\mu x}^{v(\text{obs})}}{N_{\mu x}} = \frac{N_{\mu x}^{v(\text{obs})}}{N_\mu \cdot N_x}, \\ P_{(ex)}^v &= \frac{N_{ex}^{v(\text{obs})}}{N_{ex}} = \frac{N_{ex}^{v(\text{obs})}}{N_e \cdot N_x}. \end{aligned} \quad (\text{D.8})$$

The track-flipped vertex yield in the validation region ( $N_{\mu x}^{v(\text{obs})}$ ,  $N_{ex}^{v(\text{obs})}$ ) can be extrapolated into the signal regions by,

$$\begin{aligned} N_{\mu\mu}^{v(\text{est})} &= N_{\mu\mu} \times P_{(\mu\mu)}^v \approx N_{\mu\mu} \times P_{(\mu x)}^v = \frac{1}{2} \cdot \frac{N_\mu - 1}{N_x} \cdot N_{\mu x}^{v(\text{obs})} \approx \frac{1}{2} \cdot P_{(\mu)} \cdot N_{\mu x}^{v(\text{obs})}, \\ N_{ee}^{v(\text{est})} &= N_{ee} \times P_{(ee)}^v \approx N_{ee} \times P_{(ex)}^v = \frac{1}{2} \cdot \frac{N_e - 1}{N_x} \cdot N_{ex}^{v(\text{obs})} \approx \frac{1}{2} \cdot P_{(e)} \cdot N_{ex}^{v(\text{obs})}, \\ N_{e\mu}^{v(\text{est})} &= N_{e\mu} \times P_{(e\mu)}^v \approx N_{e\mu} \times \frac{P_{(\mu x)}^v + P_{(ex)}^v}{2} = \frac{1}{2} \cdot \left( \frac{N_e}{N_x} \cdot N_{\mu x}^{v(\text{obs})} + \frac{N_\mu}{N_x} \cdot N_{ex}^{v(\text{obs})} \right) \\ &= \frac{1}{2} \cdot \left( P_{(e)} \cdot N_{\mu x}^{v(\text{obs})} + P_{(\mu)} \cdot N_{ex}^{v(\text{obs})} \right), \end{aligned} \quad (\text{D.9})$$

where the average of  $P_{(\mu x)}^v$  and  $P_{(ex)}^v$  is used for  $e\mu$  vertex.

## D.6 Scale factors

The extrapolation of the control (validation) region into the signal region,

$$\text{i.e. } \text{xx } (\mu\text{x}, \text{ex}) \rightarrow \mu\mu, ee, e\mu,$$

uses  $P_{(\text{xx})}^v$  ( $P_{(\mu\text{x})}^v$ ,  $P_{(\text{ex})}^v$ ) as an approximation of  $P_{(\mu\text{x})}^v$ ,  $P_{(\text{ex})}^v$  ( $P_{(\mu\mu)}^v$ ,  $P_{(ee)}^v$ ,  $P_{(e\mu)}^v$ ). Therefore, these extrapolation into the signal region are corrected by the scale factors obtained from the extrapolation of  $\text{xx} \rightarrow \mu\text{x}$ ,  $\text{ex}$ , defined as,

$$S_{\text{xx} \rightarrow \mu\text{x}} = \frac{N_{\mu\text{x}}^{v(\text{obs})}}{N_{\mu\text{x}}^{v(\text{est})}},$$

$$S_{\text{xx} \rightarrow \text{ex}} = \frac{N_{\text{ex}}^{v(\text{obs})}}{N_{\text{ex}}^{v(\text{est})}} \quad (\text{D.10})$$

where  $N_{\mu\text{x}}^{v(\text{obs})}$  and  $N_{\mu\text{x}}^{v(\text{est})}$  ( $N_{\text{ex}}^{v(\text{obs})}$  and  $N_{\text{ex}}^{v(\text{est})}$ ) represent the number of observed track-flipping vertex and the estimated vertex of each type.

Using these results, the scale factors applied to the extrapolation into the signal region are defined as,

$$S_{\text{xx} \rightarrow \mu\mu} = (S_{\text{xx} \rightarrow \mu\text{x}})^2,$$

$$S_{\text{xx} \rightarrow ee} = (S_{\text{xx} \rightarrow \text{ex}})^2,$$

$$S_{\text{xx} \rightarrow e\mu} = \left( \frac{1}{2}(S_{\text{xx} \rightarrow \mu\text{x}} + S_{\text{xx} \rightarrow \text{ex}}) \right)^2,$$

$$S_{\mu\text{x} \rightarrow \mu\mu} = S_{\text{xx} \rightarrow \mu\text{x}},$$

$$S_{\text{ex} \rightarrow ee} = S_{\text{xx} \rightarrow \text{ex}},$$

$$S_{\text{ex, } \mu\text{x} \rightarrow e\mu} = \frac{1}{2}(S_{\text{xx} \rightarrow \mu\text{x}} + S_{\text{xx} \rightarrow \text{ex}}), \quad (\text{D.11})$$

where the average of  $S_{\text{xx} \rightarrow \mu\text{x}}$  and  $S_{\text{xx} \rightarrow \text{ex}}$  is used for  $e\mu$  vertex.

## D.7 Vertex yields in the TF method and data

The raw vertex yields in the TF method and data, and the scale factors calculated from the vertex yields are shown in Table D.4. The extrapolation of  $\text{xx}$  into the validation region ( $\mu\text{x}$  and  $\text{ex}$ ) estimated vertex yields of 4  $\mu\text{x}$  and 5  $\text{ex}$  vertices, which are used to calculate the scale factors.

	Tracks-flipped	Data	Type	SF
$x^+x^-$	1255	1346	$S_{xx \rightarrow \mu x}$	0.82
$\mu^\pm x^\mp$	3	4	$S_{xx \rightarrow ex}$	0.19
$e^\pm x^\mp$	1	0	(b) Scale factors	

(a) Vertex yields

Table D.4: (a) Vertex yields in the TF and data. (b) The scale factors calculated from the vertex yields